NICFD and the PIV technique: Feasibility in low speed and high speed flows

Harshil Lakkad

Technische Universiteit Delft

TU Delft Delft University of Technology

Challenge the future

NICFD AND THE PIV TECHNIQUE: FEASIBILITY IN LOW SPEED AND HIGH SPEED FLOWS

by

Harshil Lakkad

in partial fulfillment of the requirements for the degree of

Master of Science
in Aerospace Engineering

at the Delft University of Technology,
to be defended publicly on Tuesday October 30, 2017 at 2:30 PM.

Student number:	4518969	
Thesis registration number:	165# 17# MT# FPP	
Supervisor:	Asst. Prof. dr. ir. F. F. J. Schrijer,	TU Delft
	Ir. A. J. Head,	TU Delft
Thesis committee:	Prof. dr. ir. P. Colonna,	TU Delft
	Dr. ir. M. Gallo,	InHolland

This thesis is confidential and cannot be made public until January 1, 2022.

TU Delft Delft University of Technology

ABSTRACT

The growing interest in organic Rankine Cycle (ORC) based power systems has encouraged ample amount of literature on the design methodologies for unconventional turbo-machinery. These machines generally operate in the so-called Non-Ideal Compressible Fluid Dynamic (NICFD) region of the working fluid where the thermophysical properties and transport properties models, and optical properties are experimentally unexplored. Therefore, these design methods need to be validated using state-of-the-art measurement techniques like Particle Image Velocimetry (PIV). PIV has not been implemented to study the non-ideal behaviour of such fluids, and therefore a feasibility study of PIV in these unconventional media is required. This work deals with exploring the possible challenges that could occur while applying the PIV technique to measure the flow comprising of non-ideal fluids in low speed and high-speed regime.

The fluids for which the feasibility is studied are Octamethylcyclotetrasiloxane (D_4) and Hexamethyldisiloxane (MM) which are frequently used working fluids for ORC power systems. The equation of state used to calculate thermo-physical properties of these fluids is briefly discussed. The viscosity of these fluids is calculated to assess the tracer particle response characteristics and check for large variations of viscosity with the thermodynamic variables. To be able to perform optical diagnostics, one also has to explore the optical properties of the working fluid — especially the refractive index. Therefore, a theoretical study of refractive index and influence of thermodynamic properties on the refractive index is studied. Conventional seeding techniques are reviewed and its feasibility for the fluids of interest is discussed.

A test facility called the Non-Intrusive Vapour Analyser (NIVA) was designed to conduct PIV in low speed vapour flows induced by a rotating disk. A suspension of D_4 and 170 nm titania particles was evaporated to obtain a seeded volume of D_4 vapour, on which PIV can be performed. The signal-to-noise ratio (SNR) was calculated to verify sufficient light scattering property of the titania particles. The seeding technique of evaporating the suspension of D_4 + titania yields sufficiently homogeneous seeding distribution. Mean velocity fields of the vapour flow in the NIVA at different disk rotation speeds could be measured with acceptable uncertainties. Considering a vast difference in flow conditions at high-speeds, a theoretical study of high-speed MM flow in a de-Laval nozzle is done to explore challenges that could occur in application of PIV. Large gradients in density are typical of dense gas expansions. This subsequently results in large gradients in optical properties like refractive index. Challenges to particle imaging due to inhomogeneous refraction of light are investigated by preliminary estimation of position error and velocity error along the nozzle axis. A conceptual design of the seeding system is proposed that can operate at high-pressures and does not risk contamination of the working fluid.

It was concluded from the experimental results in NIVA that PIV is feasible in low-speed vapour flows and can measure velocity fields with an average uncertainty of less than 1%. Also, refractive index gradients in high-speed vapour flows could cause unacceptable errors of greater than 1% in PIV measurements. These errors depend on the complexity of the fluid and the distance between the measurement plane and nozzle wall.

ACKNOWLEDGEMENTS

This research was carried out at Delft University of Technology with the Propulsion and Power group of the Faculty of Aerospace Engineering under the supervision of Dr. Ferry Schrijer and Ir. Adam Head. I am indebted to Adam for his perpetual guidance and support throughout the project. I am grateful to Prof. Schrijer for sparing time for questions whenever needed. I also extend my sincere thanks to Dr. Matteo Novara and Dr. Fulvio Scarano for fruitful discussions regarding low speed experiments. Without the mentors and all the professors who taught me during the study program, I wouldn't have been able to gather the knowledge and insights required for this project.

I would also like to thank Pankaj, Yash, Senthil, Robin, Francesco, Nicholas, Michal, Chiara, Arum, Sam, Pengqi, Andreea, Yue, Aravind, Li, Nisarg, and Shravan for being great house-mates and friends and providing warm environment away from academics. I cannot thank enough to Manoj, Arun, Shivang, Kritika, Rahul, Sai, Arjun, and Atul for sharing the much needed, stress-free and memorable time. I am also grateful to Sumit, Pranav, Rishikesh, Piyush, and Ramya for their friendship and also their academic support. All these people had a small but essential role to play in completion of this work.

And at last but never the least, I can never fairly estimate the contributions of my beloved family and friends back in India to whatever I have done in last couple of years away from home.

Harshil Lakkad
Delft, October 2017

Contents

List of Figures ix

List of Tables xi

1 Introduction 1
- 1.1 Motivation . . . 1
- 1.2 Literature Review . . . 2
  - 1.2.1 Equations of State . . . 2
  - 1.2.2 Fluid Machines for ORC . . . 4
  - 1.2.3 Experiments in Dense Gas Flows . . . 5
- 1.3 Thesis Outline . . . 8

2 Theoretical Background 11
- 2.1 Working Fluid Properties . . . 11
  - 2.1.1 Viscosity Models . . . 11
  - 2.1.2 Optical Properties . . . 13
- 2.2 Basics of PIV . . . 16
  - 2.2.1 Equation of Motion for Tracer Particles . . . 18
  - 2.2.2 Dimensional Analysis of BBO Equation . . . 18
  - 2.2.3 Seeding Strategies for Gaseous Flows . . . 21

3 Experiments in Low Speed Vapour Flows 23
- 3.1 The NIVA Apparatus . . . 23
- 3.2 PIV Measurement Set-up . . . 24
  - 3.2.1 Seeding Material and Technique . . . 25
  - 3.2.2 Laser and Camera . . . 25
  - 3.2.3 Key parameters of imaging set-up . . . 26
  - 3.2.4 Amount of Fluid in NIVA . . . 26
- 3.3 Experimental Procedure . . . 27
- 3.4 Quality of Acquired Image . . . 28
  - 3.4.1 Image Pre-processing . . . 29
- 3.5 Quality of Measurement . . . 30
  - 3.5.1 Seeding Distribution . . . 31
  - 3.5.2 Cross-Correlation Coefficient . . . 32
  - 3.5.3 Outliers, Q-factor, and Peak Lock . . . 33
  - 3.5.4 Uncertainties . . . 34
- 3.6 Conclusion . . . 35

4 PIV Analysis of Compressible Vapour Flows 37
- 4.1 Supersonic Flow of Dense Vapours . . . 37
- 4.2 Variation of Refractive Index . . . 39
  - 4.2.1 Inhomogeneous Normal Shift . . . 39
  - 4.2.2 Inhomogeneous Lateral Shift . . . 41
- 4.3 Tracer particle fidelity . . . 42
  - 4.3.1 Step Change in Fluid Flow . . . 42
- 4.4 Seeding Strategies for Vapour Tunnels . . . 45

5 Results 47
- 5.1 PIV Results from NIVA . . . 47
  - 5.1.1 Mean Velocity Fields . . . 47
  - 5.1.2 Absolute Uncertainties . . . 49

5.2 Feasibility in Compressible Flows . . . 51
5.2.1 Optical Challenges . . . 51

6 Conclusion **55**
6.1 Future Work . . . 56

A Non-Ideal Compressible Fluid Dynamics **57**

B Image Pre-processing Techniques **59**
B.1 POD based background removal . . . 59

C NIVA Instantaneous Velocity Fields **61**
C.1 0 Hz Case . . . 61
C.2 10 Hz Case . . . 62
C.3 20 Hz Case . . . 62
C.4 30 Hz Case . . . 63
C.5 40 Hz Case . . . 63

D Miscellaneous Information on DaVis **65**
D.1 Vector processing in DAVIS . . . 65
D.1.1 In Chapter 5 . . . 65
D.2 Importing Background Removed Images . . . 65
D.3 Uncertainty Quantification . . . 66
D.4 Relative Uncertainty . . . 68
D.5 PIV Data Quality Table from NIVA . . . 69

E MATLAB Codes **71**
E.1 Euler Shock Wave Calculator . . . 71
E.1.1 Code . . . 71
E.2 Vapour Viscosity Plot . . . 75
E.3 Molecular Complexity Plot . . . 77
E.4 Particle Equation of Motion . . . 77
E.5 Particle Image Count . . . 79

Bibliography **81**

List of Figures

1.1 Compressibility contours near critical point on T-S plot of D_4. . . . 3
1.2 Nozzle shapes for M_{exit} = 2.0 for varying polytropic index (throat radius of curvature is 2.5 times the throat height) [1]. . . . 5
1.3 Comparison of turbine stage designed by Wheeler and Ong and the NASA's turbine stage used for RANS validation, taken from [2]. . . . 5
1.4 Schlieren image of supersonic expansion of MDM vapour flow shown image corruption due to condensation, taken from Ref. [3]. . . . 7
1.5 Occurence of HWA, LDV, and PIV, taken from ref.[4]. . . . 7
1.6 LDV measurements of supersonic MDM flow 15 mm downstream of the throat, taken from Ref. [5]. . . . 8

2.1 Variation of viscosity with pressure. . . . 12
2.2 Variation of viscosity with temperature. . . . 13
2.3 Molecular complexity vs Molecular mass 13
2.4 Real component vs. density 15
2.5 Change in real component of the refractive index with density in a typical nozzle flow case. . . . 16
2.6 Schematic depicting the application of the PIV technique[6]. . . . 17
2.7 Cross-correlating the image pair. . . . 17
2.8 Particle relaxation after the shock wave in air. . . . 20
2.9 Fluidization of metal oxide powder[6, 7]. . . . 21
2.10 Atomization of metal oxide suspension [7]. . . . 22

3.1 CAD model and realization of NIVA. . . . 23
3.2 Motor calibration curve 24
3.3 Heating plate temperatures curves. Time t = 0 does not correspond to switching on of the heating plate. . . . 24
3.4 The NIVA 25
3.5 Operating point of NIVA. . . . 27
3.6 Temperature of the floor and ceiling of NIVA. . . . 28
3.7 Evaporation Process. . . . 28
3.8 The raw data images. . . . 29
3.9 Result of subtracting TSM. . . . 29
3.10 Result of POD-based background removal. . . . 29
3.11 Number of particles detected vs. chosen threshold value. . . . 31
3.12 Seeding density profile in vertical direction. . . . 31
3.13 Correlation values after processing images using interrogation window of different sizes. . . . 32
3.14 Vector fields obtained using different interrogation window sizes. . . . 33

4.1 Nozzle shape with Mach no. distribution. Throat radius of curvature is 50 units. . . . 38
4.2 Nozzle shape with temperature distribution. . . . 38
4.3 Nozzle shape with density distribution. . . . 38
4.4 Nozzle shape with refractive index distribution. . . . 39
4.5 Normal shift due to refraction. . . . 39
4.6 Schematic of focal depth and laser sheet thickness along with refractive index profile at nozzle axis for MM. . . . 40
4.7 Errors due to presence of on-zero refractive index gradient. . . . 41
4.8 Refractive index derivative and refractive index second derivative profile along the nozzle axis for MM. . . . 42
4.9 Oblique shock wave and velocity jump. . . . 43

4.10 Response characteristics of 170 nm titania particles in supersonic MM flow calculated numerically. . . . 43
4.11 Response of tracer particle to sudden flow turning. . . . 44
4.12 Flow turning response of the 170 nm titania particles for in a dense MM flow. . . . 44
4.13 Radius of curvature of particle trajectory in dense MM flow for deflection angle varying from 1^o to 10^o. . . . 45
4.14 Conceptual design of seeding system for vapour tunnels. . . . 46

5.1 Comparing effects of image pre-processing on vector fields. . . . 47
5.2 Disk rotating at a frequency of 0Hz. . . . 48
5.3 Disk rotating at a frequency of 40Hz. . . . 48
5.4 Disk rotating at a frequency of 30Hz. . . . 49
5.5 Disk rotating at a frequency of 20Hz. . . . 49
5.6 Disk rotating at a frequency of 10Hz. . . . 49
5.7 Absolute uncertainty field in $[cm/s]$ for different disk rotational frequencies. . . . 50
5.8 Normal shift due to refraction. . . . 51
5.9 First and second derivative of the refractive index along the nozzle axis for MM. . . . 52
5.10 X-component of velocity and its derivative profile along the nozzle axis for MM. . . . 52
5.11 Position and velocity errors divided by W^2. . . . 53
5.12 Expansion process of MM flow over T-S plot. . . . 53

A.1 Saturation curve of D_6 and iso-Γ lines < 1. Grey regions represents $\Gamma < 0$ (extracted from Ref. [8]). 57

B.1 Result of POD based background removal. . . . 60

C.1 Instantaneous velocity fields at different time instances. . . . 61
C.2 Instantaneous velocity fields at different time instances. . . . 62
C.3 Instantaneous velocity fields at different time instances. . . . 62
C.4 Instantaneous velocity fields at different time instances. . . . 63
C.5 Instantaneous velocity fields at different time instances. . . . 63

D.1 Cross-correlation settings in DaVis 65
D.2 Cross-correlation settings in DaVis 65
D.3 Post-processing option in DaVis 66
D.4 Step 1 66
D.5 Step 2 67
D.6 Step 3 67
D.7 Step 4 68
D.8 Distribution of disparity over an interrogation window [9]. . . . 68
D.9 Image division for analysing quality of data in different regions. . . . 69

List of Tables

1.1 Properties of common working fluids [10]. . . . 2
1.2 Simulation results from molecular simulation in [11]. Temperature, vapour pressure, saturated vapour density, and enthalpy of vaporization for D_4. . . . 4

2.1 Refractivity data of constituent bonds of D_4 and MM . . . 15
2.2 Optical properties of D_4 and MM . . . 15
2.3 Commonly used tracer particles in gas flows [6] . . . 21

3.1 Optical parameters of imaging. . . . 26
3.2 Threshold value to detect particles, seeding density in ppp, source density (N_s), Average SNR. . . . 32
3.3 Interrogation window size wise % of outliers. . . . 34
3.4 Uncertainty data. . . . 34

4.1 Relaxation distance and time for 170 nm titania particles in supersonic MM flow. . . . 43

D.1 Interrogation window size wise % of outliers in two different regions. . . . 70

NOMENCLATURE

Symbol	Description	Units
T_c	Critical temperature	K
p_c	Critical pressure	bar
ρ_c	Critical density	$kg \cdot m^{-3}$
T_{boil}	Boiling point temperature	K
T_{TD}	Thermodynamic stability temperature	K
Z	Compressibility factor	-
p_v	Vapour pressure	bar or Pa
ρ_v	Vapour density	$kg \cdot m^{-3}$
R_u	Universal gas constant	$kJ \cdot kmol^{-1}K^{-1}$
R	Specific gas constant	$kJ \cdot kg^{-1}K^{-1}$
a	Parameter for attractive term in van der Waal's equation of state	$Pa \cdot m^6$
b	Parameter for molecule size term in van der Waal's equation of state	$m^3 mol^{-1}$
Φ	Specific Helmholtz energy	$kJ \cdot K^{-1}$
ϕ	Non-dimensional Helmholtz energy	-
C_p	Specific heat at constant pressure	$kJ \cdot kg^{-1}K^{-1}$
hv	Molar specific enthalpy of vapour	$kJ \cdot kg^{-1}K^{-1}$
k	Polytropic index	-
γ	Ratio of specific heats	-
μ	Dynamic viscosity	$Pa \cdot s$
m	Mass of a molecule	kg
k_B	Boltzmann constant	$J \cdot K^{-1}$
$\Omega(2,2)$	Collision integral of a molecule	m^2
υ	Distance at which the inter-molecular potential is zero	m
ε	Minimum inter-molecular potential energy	J
F_μ	Factor to transform reference fluid viscosity to viscosity of fluid of interest using corresponding states	-
f	Equivalent substance reducing ratio of critical temperatures	-
h	Equivalent substance reducing ratio of critical densities	-
σ	Molecular complexity	-
$S_{sat.vap.}$	Specific entropy of saturated vapour	$kJ \cdot kg^{-1}K^{-1}$
$\hat{n}$	Complex form of refractive index	-
n	Real part of the refractive index or simply refractive index	-
κ	Imaginary part of the refractive index or extinction coefficient	-
A	Molar refractivity	$cm^3 mol^{-1}$
N_A	Avogadro's number	mol^{-1}
α	Mean polarizability of a substance	cm^3
M	Molecular mass of a substance	$g \cdot mol^{-1}$ or $kg \cdot kmol^{-1}$
A_s	Specific refractivity	$cm^3 g^{-1}$
K	Gladstone-Dale constant	$cm^3 g^{-1}$
λ	Wavelength of electromagnetic wave	m
ω	Frequency of electromagnetic wave	s^{-1}
Δt_p	Light pulse separation used for PIV imaging	s
m_p	Mass of a tracer particle	kg
$\vec{u}_p$	Tracer particle velocity vector	ms^{-1}
d_p	Diameter of a tracer particle	m
Ω	The frequency scale of flow over particle used for non-dimensionalising the time variable	s_{-1}
$\vec{u}_f$	Fluid flow velocity vector	ms^{-3}

$\vec{u}_s$	Slip velocity vector	ms^{-1}
ρ_p	Density of a tracer particle	$kg \cdot m^{-3}$
ρ_f	Density of of the fluid flow	$kg \cdot m^{-3}$
g	Gravitational acceleration	ms^{-2}
C_D	Drag coefficient of a tracer particle	-
Re_p	Reynolds number of the flow over the tracer particle w.r.t. the particle	-
τ_p	Particle response time or relaxation time	s
ξ_p	Particle response distance or relaxation distance	m
τ_{flow}	Characteristic time of a flow feature	s
τ_κ	Kolmogorov time scale	s
St	Stoke's number	-
D	Diameter of the rotating in NIVA	cm
V_t	Tangential velocity of disk periphery in NIVA	ms^{-1}
M_f	Magnification factor of imaging set-up	-
$f_\#$	f-stop or f-number of imaging set-up	-
Δ_{pix}	Digital resolution of imaging set-up	$\text{pix} \cdot mm^{-1}$
Δz_f	Focal depth of the imaging set-up	mm
d_τ	Particle image diameter	mm or pix
V_{box}	Volume of the vapour box in NIVA	cm^3 or L
T_{max}	Maximum operating temperature of NIVA	$^\circ C$
T_{work}	Working temperature of NIVA	$^\circ C$
I	Image matrix	-
I_p	Particle image component of image matrix	-
I_b	Background noise component of image matrix	-
N_s	Image source density	-
θ_i	Incident angle of light at an interface from an object	$degrees$
θ_r	Refracted angle of light at an interface from an object	$degrees$
Δz_l	Light sheet thickness	mm
W	Distance between the measurement plane and the nozzle wall	mm
$\vec{\epsilon}$	Position error due to optical distortions	mm
∇	Gradient operator	-
∇^2	Laplacian operator	-
$\vec{\epsilon_v}$	Velocity error due to optical distortion	ms^{-1}
θ	Obstructing wedge angle in supersonic flow	$degrees$
β	Oblique shock wave angle	$degrees$

Abbreviation	**Description**
NICFD	Non-Ideal Compressible Fluid Dynamics
PIV	Particle Image Velocimetry
ORC	Organic Rankine Cycle
MOC	Method of Characteristics
ORCHID	Organic Rankine Cycle Hybrd Integrated Device
TROVA	Test-Rig for Organic Vapours
CFD	Computational Fluid Dynamics
RANS	Reynold's Averaged Navier-Stokes
LES	Large Eddy Simulation
HWA	Hot-Wire Anemometry
LDV	Laser Doppler Velocimetry
NIST	National Institute of Standards and Technology
OSW	Oblique Shock Wave
TSM	Time Series Minimum
POD	Proper Orthogonal Decomposition
PPP	Particles per Pixel
SNR	Signal-to-Noise Ratio
RMS	Root Mean Square
BOS	Background Oriented Schlieren

1

INTRODUCTION

1.1. MOTIVATION

The Organic Rankine Cycle (ORC) is the most applied technology for conversion of low temperature thermal energy sources such as geothermal energy, industrial waste heat, and biomass combustion energy etc. An estimate of around 640 to 1025 GWh of electricity per year can be extracted from industrial waste heat using ORC technology in Italy alone. The choice of the working fluids for any thermodynamic cycle is driven by reasons like simplistic design of expanders for a wide range of power levels (especially turbines), safety, and availibility. Using ordinary Rankine cycle with steam as working fluid is not practical for such low temperature heat sources because it's efficient operation mandates very low mass flow rate. Very low mass flow rate results in extremely complex design of turbo-machinery which makes a cost-effective design of a Rankine cycle set-up for energy conversion infeasible. The choice of a complex molecule for working fluids satisfies a variety of needs like feasibility of supercritical cycle even at low maximum temperaure; high mass flow rate that allows optimization of expander for any power levels; moderate peripheral speeds of turbmachinery without condensation; choice of pressure levels between components independent of temperature of heat source and cold sink etc [12, 13]. Certain families of chemical compounds mentioned in Table 1.1 are complex enough to satisfy the above requirements and are thermodynamically stable within the typical operating range of ORC power plants.

Along with selection of the working fluid, the design of the turbo-machinery is an equally crucial aspect of any power system. The process of designing turbo-machinery involves solving equations of conservation of mass-momentum-energy and equations of state. The equations of conservation of mass-momentum-energy are derived from the laws of conservation and hence will remain the same for the new working fluid, however, the equations of state will change drastically. The ideal gas equation of state is not valid for the vapours of complex fluids mentioned in the Tab. 1.1 due to the presence of inter-molecular forces and highly non-spherical geometry. Numerous equation of state for such fluids have been developed which can be classified as cubic equations of state, non-cubic equations of state, Virial equations of sate, Multi-parameter equations of state etc. The reliability of these equations or as a result the reliability of the turbo-machinery design can only be verified by experiments. Particle Image Velocimetry (PIV) is one of the most reliable experimental technique to validate flow solvers. The literature on experimental verification of flow solvers for the ORC working fluids is very deficient because the increase in popularity of ORC based power systems is a fairly recent phenomenon.

Two most important aspects of PIV upon which the accuracy of the measurement depends are flow seeding and imaging the seeded particles. The unconventional behaviour of ORC working fluids demands a thorough investigation on the feasibility of these aspects of PIV. Main purpose of this work is to evaluate these aspects of PIV technique on flows comprising of ORC working fluids and recommend modifications to conventional implementation of the measurement technique.

Siloxanes	T_c/K	p_c/bar	T_{boil}/K	T_{TD}/K
D_4	586.5	13.3	448.5	≈623
D_5	619.2	11.6	484.0	≈623
D_6	645.8	9.61	518.2	≈623
MM	527.8	19.4	373.4	≈573
MDM	564.0	14.2	425.4	≈623
MD_2M	599.4	12.3	467.6	≈623
MD_3M	628.4	9.4	503.0	≈623
MD_4M	653.2	8.8	533.8	≈623
Hydrocarbons				
Toluene	591.8	41.3	383.8	≈673
Pentane	469.6	33.7	309.2	≈543
Cyclopentane	511.65	45.1	322.4	≈573
Perfluorocarbons				
PP2	486.0	20.2	349.2	≈573
PP80	507.12	16.85	376.4	≈573
PP90	530	16.0	398.2	≈573
Hydrofluorocarbons				
R245fa	427.2	36.5	288.25	≈533.15

Table 1.1: Properties of common working fluids [10].

1.2. LITERATURE REVIEW

It was stated in the previous section that vapours of the fluids mentioned in Tab. 1.1 does not obey the ideal gas equation of state in typical operating conditions of an ORC power plant. The deviation of these vapours from the ideal gas behaviour is generally measured in terms of compressibility factor which is given by Eqn. 1.1, where, p_v is the vapour pressure, ρ_v is the vapour density, and T is the vapour temperature. The specific gas constant R is given by $\frac{R_u}{M}$ where, R_u is the universal gas constant and M is the molecular mass of the fluid.

$$Z = \frac{p_v}{\rho_v RT} \tag{1.1}$$

The vapour is said to behave like an ideal gas if $Z \approx 1$. Non-ideal fluid flows in compressible regime exhibit compressibility factor significantly lower than 1 (Fig. 5.12a) which is typical of unconventional turo-machinery for ORC power systems. In this regime the speed of sound in the fluid medium shows appreciable variation with the thermodynamic properties and study of such flows is referred to as Non-Ideal Compressible Fluid Dynamics (NICFD). However, a more technical definition of NICFD is described in App. A. Further in the coming subsections a brief review of equation of state used in this work is presented. The effect of properties of fluid on the shape of expander is discussed. A select few works on measurements in unconventional fluid media is reviewed in context of validation of turbo-machinery designs.

1.2.1. EQUATIONS OF STATE

van der Waal (1873) was the first to propose an equation of state for liquid and vapour phase considering the intermolecular forces based on the principle of corresponding states [14]. The equation of state proposed by van der Waal is shown by Equation 1.2.

$$p = \frac{R_u T}{V - b} - \frac{a}{V^2}. \tag{1.2}$$

The parameter a and b are related to the attractive forces between molecules and the size of the molecules respectively, and can be given in terms of critical parameters of the gases as follows,

$$a = \frac{27 R^2 T_c^2}{64 p_c}, \tag{1.3}$$

$$b = \frac{RT_c}{8 p_c}. \tag{1.4}$$

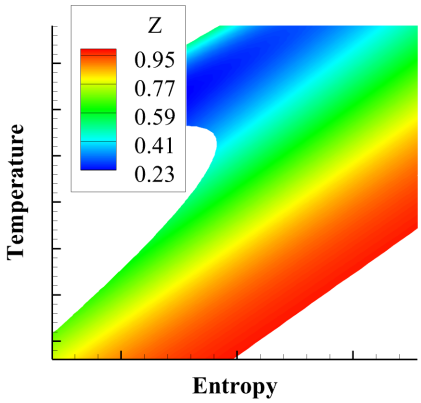

Figure 1.1: Compressibility contours near critical point on T-S plot of D_4.

Later, various equations of state were proposed with further improvements to Van der Waals equations. Improvements were made to attractive term by making it temperature dependent, by introducing fluid specific parameters like accentric factor to the attractive terms etc. Further considerations were given to improve the prediction of fluid-phase equilibria for simple molecules, chain molecules, and associating fluids [15]. These equations can be appropriately made the basis for developing a multi-parameter equation of states and can be optimized for specific fluids. One of such example is the functional form of multiparameter equation of state given by Eqn. 1.5 which was optimized for selected siloxanes by Colonna et. al. (2006). This equation is the Span-Wagner form of the equation of state.

$$\frac{\Phi(T,\rho)}{R_u T} = \frac{\Phi^{ig}(T,\rho) + \Phi^{r}(T,\rho)}{R_u T} = \phi^{ig}(\tau,\delta) + \phi^{r}(\tau,\delta) \tag{1.5}$$

where, Φ is specific Helmholtz energy and superscripts ig and r indicates ideal gas and residual terms respectively. τ and δ are dimensionless temperature ($\frac{T_{ref}}{T}$) and dimensionless density ($\frac{\rho}{\rho_{ref}}$) respectively. Reference values are generally chosen as critical values which makes τ as inverse of reduced temperature and δ as reduced density when we talk about different states in a thermodynamic cycle. Ideal gas Helmholtz energy is given by Equation 1.6.

$$\Phi^{ig} = \Phi_0 + \int_{T_0}^{T} (C_P^{ig} - R_u) dT - T\int_{T_0}^{T} \frac{C_P^{ig} - R_u}{T} dT + R_u T ln(\frac{\rho}{\rho_0}) \tag{1.6}$$

The residual Helmholtz energy is given by Equation 1.7 that depends on 12 fluid specific parameters.

$$\begin{aligned}\phi^{r}(\tau,\delta) = {} & n_1\delta\tau^{0.250} + n_2\delta\tau^{1.125} + n_3\delta\tau^{1.5} + n_4\delta^2\tau^{1.375} + n_5\delta^3\tau^{0.250} + n_6\delta^7\tau^{0.875} + n_7\delta^2\tau^{0.625}e^{-\delta} \\ & + n_8\delta^5\tau^{1.750}e^{-\delta} + n_9\delta\tau^{3.625}e^{-\delta^2} + n_{10}\delta^4\tau^{3.625}e^{-\delta^2} \\ & + n_{11}\delta^3\tau^{14.5}e^{-\delta^3} + n_{12}\delta^4\tau^{12}e^{-\delta^3}\end{aligned} \tag{1.7}$$

Values of n_i's for MM, MD_4M, and D_4 are given in Table 11, 12, and 13 respectively in Ref [16].

Further experimental investigation on speed of sound measurements as reported by Thol et. al. (2015) shows that Eqn. 1.5 yields marginally inaccurate values of speed of sound [17]. The authors measured the speed of sound in MM using a pulse-echo technique, which considerably extends the limited amount of thermodynamic data on MM available in literature. The authors used these data to optimize a form of equation similar to Eqn. 1.5 for the fluid MM. This data was also used to verify the validity of predictions using molecular simulation of MM. Similar speed of sound data and molecular simulation was used to predict thermodynamic properties of D_4 by Thol et. al. (2016) and Tab. 1.2 shows data for a few thermodynamic points [11].

For more rigorous studies the thermodynamic properties are calculated using thermodynamic library softwares that are programmed using equation of states that will be most suitable for the desired fluid. One

T/K	p_v/MPa	ρ/mol·dm^{-3}	h_v/kJ·mol^{-1}
320	0.0005	0.00017	52.22
330	0.0008	0.0003	51.02
335	0.0017	0.0006	50.4
435	0.064	0.0187	40.77
450	0.098	0.0282	39.16
500	0.301	0.086	33.06
525	0.47	0.136	29.33
550	0.759	0.241	24.46

Table 1.2: Simulation results from molecular simulation in [11]. Temperature, vapour pressure, saturated vapour density, and enthalpy of vaporization for D_4.

such software called REFPROP by NIST is used in this work to calculate thermodynamic properties and transport properties [18]. REFPROP uses the multi-parameter equation of state given by the Eqn. 1.5 developed by Colonna et.al. (2006) [16] for the siloxanes mentioned in the Tab. 1.1. The thermodynamic properties computed using REFPROP deviates from the more accurate predictions presented by Thol et. al., however, the deviations are within acceptable limits.

1.2.2. FLUID MACHINES FOR ORC

A fluid machine is a system within which one or more fluid performs energy conversion through dynamic or kinematic processes [13]. Turbines or expanders are the machines that extract the energy from the working fluid and converts into mechanical energy, and are the prime movers of any power system. The design of an efficient expander depends on the properties of the fluid, and thus their size and shape for ORC power systems are anticipated to be drastically different than that for steam power systems.

The simplest represention of a stator is a de-Laval nozzle (or Convergent-Divergent nozzle), which is designed using the Method-of-Characteristics (MOC). MOC uses the Prandtl-Meyer function[1] to determine the shape of the nozzle walls for given entry and exit Mach nos. [1]. MOC is generally used to design the nozzles for gases with a constant polytropic index[1] greater than unity (i.e. ideal gases), however MOC was used by Aldo and Argrow (1993) for the first time to design a supersonic nozzle for non-ideal gases as well [1, 19]. Another modified and simpler approach to design supersonic nozzles for non-ideal gases using MOC is presented by Wheeler and Ong (2013) in Ref [1]. Wheeler and Ong designed a supersonic nozzle for the fluids Pentane and R245fa which are common choices in ORC turbines. The authors assumes that pressure and density of these fluids follows the relationship given by the Eqn. 1.8. In reality, the value of k varies between 0.9-1.1 (which decreases even further near critical region) for these gases which can be verified by plotting pressure versus density using refprop. Wheeler and Ong uses a linear regression on the logarithm of pressure versus logarithm of density plot to determine the k [1].

$$\frac{p}{\rho^k} = constant \tag{1.8}$$

For ideal gases the k is equal to the γ which is always greater than unity, however for dense gases the k can be greater than or less than unity depending upon the thermodynamic state of the gas and is significantly lesser than unity near the critical point. Owing to a large difference in k the nozzle shapes for dense gases are significantly different from that for ideal gases. Dependence of the nozzle shape can be seen in the Fig. 1.2. These nozzle designs can be extended to design turbine vanes to achieve a desired entry mach. no for the rotating component. A radial turbine is preffered for ORC applications due to its simplicity, robustness, and effficieny.

After the preliminary design of the turbo-machinery components, it is crucial to assess their performance. This is generally done by studying 2-D and 3-D flow structures inside the turbine using CFD simulations. Flows through turbines are also simulated to investigate efficiency inhibitors like turbulence, boundary layer growth, heat losses, trailing-edge losses, friction etc. and the design is changed so as to minimize their effects. However, all these numerical calculations cannot be used to design a manufacturable model without validation using experimental data, which is scanty. For example, Wheeler and Ong (2014) presents designs of radial inflow turbines which are designed using the modified MOC approach, and the study of the 3-D un-

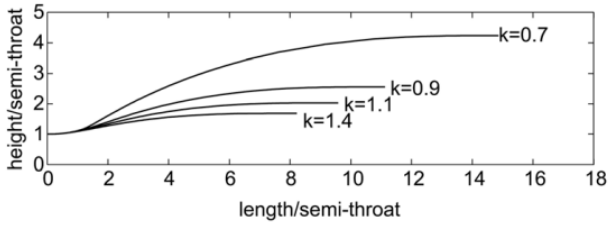

Figure 1.2: Nozzle shapes for M_{exit} = 2.0 for varying polytropic index (throat radius of curvature is 2.5 times the throat height) [1].

steady flows within the turbines using RANS simulation [2]. The study shows significant reduction in trailing edge losses in the turbo-machinery for unconventional fluids. Due to unavailability of experimental rig data, authors used data from conventional radial inflow turbine stage obtained by NASA to validate the RANS simulation [20]. The Fig. 1.3 shows significant difference between geometries of the designed turbine and turbine used for validation. Various experimental techniques that are routinely used for verification of numerical designs are discussed in the Sec. 1.2.3 using a select few references.

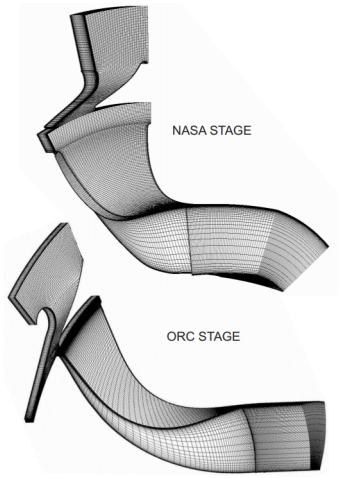

Figure 1.3: Comparison of turbine stage designed by Wheeler and Ong and the NASA's turbine stage used for RANS validation, taken from [2].

1.2.3. EXPERIMENTS IN DENSE GAS FLOWS

Any proposed theory, or a theoretical prediction based on a theory, or a computer simulation in fluid mechanics is subject to experimental validation before it is accepted for application by the community. For validation of numerical models of turbo-machinery, the experiments could be aimed at measuring a gross quantity like the attainable power (for e.g. study by Kang (2012)[2]), or more fundamental quantities like velocity, pressure, temperature, and density. The latter quantities which are more frequently measured are functions of space and time, and are generally called field variables. Depending on the quantity to be measured, the measurement technique should be chosen carefully and the results should be interpreted with caution. The choice of measurement technique is generally driven by the complexity of instruments range of validty, accuracy, cost, spatial & temporal resolution, and interference with the flow field [22]. The following subsections will summarize few popular measurement techniques used to measure field variables in dense gas medium in

[1] If a gas undergoes a process such that $p\rho^{-k}$ is a constant then the process is called a polytropic process and k is called the polytropic index. For adiabatic processes of ideal gases, the polutropic index is equal to the ratio of the specific heats (γ) and the terms are used interchangeably, however the equality does not hold for dense gases. Prandtl-Meyer function (ν) is the angle of deflection through which supersonic flow can turn isentropically for a given initial and final Mach no. [21]. It is a function of the Mach no. and the polytropic index (k).

[2] Kang (2012) conducted experiments to study the operational characteristics of a newly developed ORC with R245fa as working fluid. A radial turbine designed for the ORC was also tested. The efficiecy of the turbine and cycle, amount of electric power produced were analysed with varying operating conditions.

past work.

MEASUREMENT BY PRESSURE PROBES

Absolute or gauge pressure can be measured using different kind of transducers and the choice of transducer is dependent on the magnitude of the pressure, desired sensitivity, interference with the flow, and robustness [22]. In most of experimental fluid mechanics campaign an orifice connects the flow to the sensing element which can be a manometer, piezo-electric sensor, piezo-capacitive sensor, piezo-resistive strain-gauge etc. A pressure measurement instrument called Pitot-static tube is also used to deduce velocity by measuring total and static pressures at a location. The difference in total and static pressure and density of the fluid is used to calculate the velocity using Bernoulli's equation.

The interest in dense gases increase immensely when the works Bethe (1942) and Zel'Dovich (1946) suggested that expansion shock waves can be possible in certain fluids for which $\Gamma < 0$ is possible is certain thermodynamic conditions (Γ is fundamental derivative of gas dynamics described in A). In an attempt to show such phenomena experimentally, several shock-tube experiments have been conducted without any success. Pressure measurement is used to monitor the moving shock in a shock-tube experiments. Since the shocks move at very high speed, pressure transducers with high-frequency response are needed. Borisov et. al. in 1980 for the first time used a Ludwieg shock tube to detect the occurrence of a rarefaction shock, however the results are now considered as erroneous. Similar investigation to study the variation of the speed of sound in Siloxanes was undertaken separately by Nannan (2009) and Mathijssen (2016) in the Flexible Axisymmetric Shock Tube facility at TU Delft [23–25]. Another study by Galiana et. al. (2015) was conducted at Ludwieg shock tube facility at Whittle laboratory in Cambridge university to investgate trailing-edge losses in ORC turbines [26]. Galiana et. al. conducted the study for Air, CO_2, and SF_6 flows and found that the base flow separation downstream of trailing-edge is significantly reduced for dense gases compared to Air. This study was used to validate the RANS and LES simulation of the trailing edge models which were used to predct trailing edge losses. The authors found that RANS failed to correctly predict flow structure downstream of the trailing-edge, however, the LES simulations were closer to the experimental results [26]. All these studies rely on pressure measurements on detection of shocks using high-frequency response pressure transducers and the accuracy of pressure measurements were not influenced by the non-ideal nature of the fluids.

TEMPERATURE MEASUREMENTS

Temperature is an important parameter to indicate the energy of the fluid. Temperature measurements can be used to calculate the energy lost or gained by the fluid. Temperature is also an important parameter to be monitor to keep check on thermal loads. Temperature is measured using a thermocouple, which is a junction of two different metals. Different types of thermocouples are chosen in different temperature ranges.

Temperature measurements of MM vapours were carried in an electric tube by Preissinger and Brueggmann (2016) to study to degradation of MM. They kept MM under varying temperature conditions for long periods and studied the compositions using chromatography and mass spectroscopy. The temperature was measures using thermocouple. The results showed that MM vapours degrades at a rate of 5 % per year at a temperature of $300°C$. The authors report that the design of direct contact evaporator for MM requires special care concerning film temperature and should not promote concentrated hot spots in the evaporator. Free water molecules and contaminants can significantly increase the degradation rate and requires a special start-up procedure. A suggestion is also made to include thermal stability as a design parameter for ORC systems and the maximum temperature as a boundary conditions for the ORC simulations [27].

SCHLIEREN PHOTOGRAPHY

Schlieren photography is used to visualize density variations in a flow field. The captured quantity in the schlieren technique is the density gradient. Detailed description of a method of density and density gradients quantification is described by Elsinga (2003) which is also using in this work [28]. There has been two schlieren campaign on the dense gases used for ORC. The first is by Spinelli et. al. (2015), who presented the results of schlieren experiments on a nozzle flow of MDM vapours [3]. The experiments were conducted in a facility called TROVA (Test Rig for ORganic Vapours) designed by Spinelli as part of his doctoral studies [29]. Authors report that the preliminary results for nozzle flow of MDM vapours were consistent with that of air, however the images were quite polluted by the condensation of the vapour during expansion (Fig. 1.4). Other measurements like pressure and temperature were in good agreement with the numerical predictions

which suggests negligible influence of fluid behaviour on temperature and pressure measurements [3]. The second is by Gori et. al. (2017) who presents the first ever experimental assessment of the NICFD solvers for ORC applications using Schlieren experiments. The authors report the validity of the thermodynamic models and the CFD implementation using both the RANS equations for non-ideal compressible turbulent flows and Euler equations for inviscid flows [30].

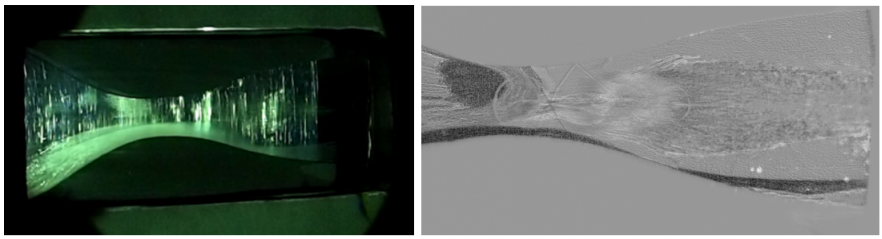

Figure 1.4: Schlieren image of supersonic expansion of MDM vapour flow shown image corruption due to condensation, taken from Ref. [3].

Another vapour tunnel is being developed at Delft University of Technology called ORCHID (Organic Rankine Cycle Hybrid Integrated Device) by Head et. al. (2016) [31]. ORCHID will be used to test ORC expanders (both stationary and rotating components) and validate the numerical designs for applications in Industrial ORC based power systems. TROVA will only be used to validate stationary components like stator vanes. TROVA does not facilitate tests for moving components.

ADVANCED VELOCIMETRY TECHNIQUES

The aim of turbo-machinery design process is to achieve the desired velocity distribution across the component. The velocity fields predicted by the numerical designs need to be reproduced in the experiments to validate the design. Researchers have been using advanced velocity measurement techniques to validate designs like Hot Wire Anemometry (HWA), Particle Image Velocimetry (PIV), Laser Dopler Velocimetry (LDV) etc. In recent times, the most preferred velocimetry technique is PIV as can be seen from the Fig. 1.5.

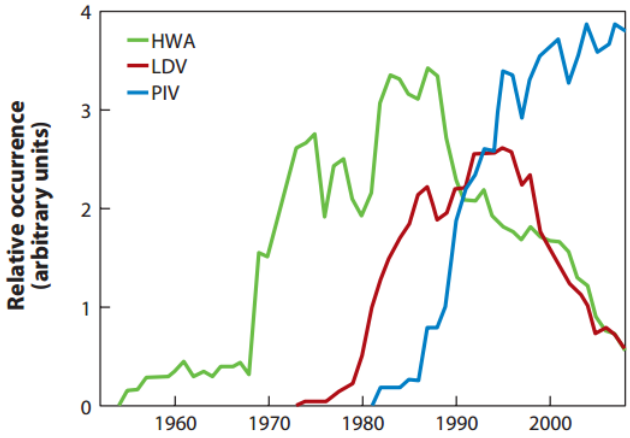

Figure 1.5: Occurence of HWA, LDV, and PIV, taken from ref.[4].

PIV has never been used to measure flows of dense gases. The closest relevant example is the use of PIV in gas-liquid two-phase nozzle flow of CO_2 by Ueno et.al. (2015). Close to critical point CO_2 shows some non-ideal behaviour, however, its complexity and deviation from ideal behaviour is not nearly as drastic as the fluids shown in the Tab. 1.1. The study was not aimed at verification of a nozzle design, instead it was to study the acceleration and flow characteristics in an open and closed nozzle configuration with reservoir pressures slightly above (9 MPa) and slightly below (7 MPa) critical pressure of CO_2 [32]. The acceleration characteristics are then used to further optimize the nozzle for the application as ejector in refrigeration cycle. No comments were given by authors on any effect on accuracy of PIV conducted in unconventional

medium.

LDV has been used to measure velocity of dense supersonic flow of MDM by Gallarini (2016), where the measurement was done as a part of commissioning of a LDV system implemented in the TROVA facility at Politecnico di Milano. LDV is a non-intrusive laser based velocimetry technique that uses tracer particles to measure the flow velocity. The velocity is determined by sensing the Doppler shift in frequency of incident laser after reflection from tracer particles. The work of Gallarini was aimed at designing an effective seeding system which is claimed to be satisfactory, however, some issues were encountered regarding the failure of the mixing pump due to metallic powder and insuffiecient scattering power of the seeded particles to be detected by the LDV system. The velocity measurements were done at a location 15 mm downstream of the nozzle throat using three kinds of tracer particles namely, Aerosil 200 (silica) of diamter 100-150 nm, titania of diameter 150-250 nm, and powder made from impurities that caused mixing pump failure. The velocity obtained were considerably lower than that were expected from the inviscid CFD simulations. In the case of Aerosil 200 and titania seeding the inaccuracy and low measurement rate is attributed to the insufficient scattering due to small size by the author. A much better measurement rate was observed using the pump impurities as tracer due to its large size, however, that also resulted in pretty inaccurate results [5].

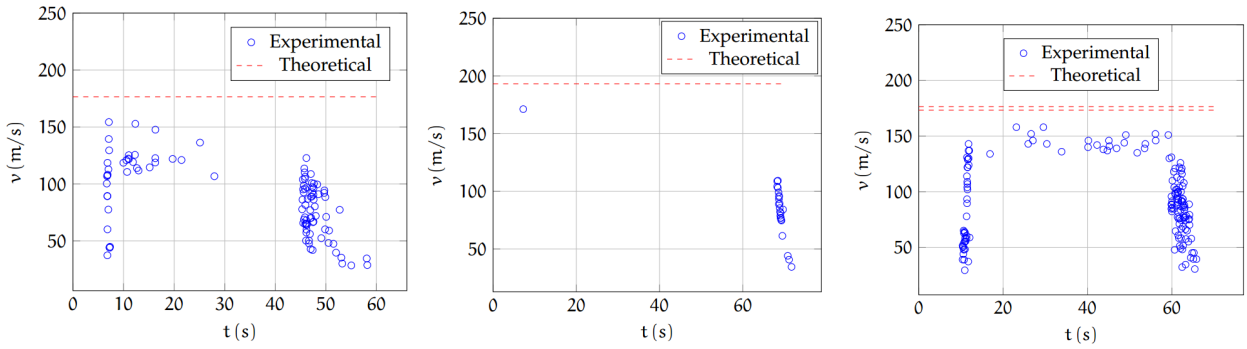

(a) Aerosil 200 (b) Titania (c) Pump impurities

Figure 1.6: LDV measurements of supersonic MDM flow 15 mm downstream of the throat, taken from Ref. [5].

1.3. THESIS OUTLINE

It is clear that the deficiency in experimental validation for solvers of non-ideal fluid flows is stark, and prolific campaigns involving pressure, temperature, and velocity measurements are needed. Previous works suggests that the non-ideal behaviour does not influence the ex-situ techniques like temperature and pressure measurement. There has been only one in-situ experimental campaign on supersonic MDM flows by Gallarini (2016) utilizing LDV and it resulted in appreciable inaccuracies [5]. This encourages a thorough investigation of feasibility of a similar in-situ technique, PIV. Similar to LDV, seeding is required in PIV to track the flow and optical signals from the particles are captured to evaluate velocity. Therefore, the feasibility of PIV relies on the accuracy of the tracer particles to follow the flow and optical properties of the medium to transmit uncorrupted signals. An efficient seeding system is also required to introduce the tracer particles, however, this requires a separate study, hence, only a conceptual design will be discussed. With this purpose in mind, the structure of the thesis from here onwards is as follows,

- Theoretical background: Two of the properties of the fluid of interest namely, viscosity and refractive index are theoretically calculated. These properties will be utilized to reflect on tracer particle motion in the fluid and imaging of the tracer particles. Popular seeding strategies for solid tracer particles in gaseous flows will be presented to test for its feasibility in vapour tunnels.
- Experiments in low speed vapour flows: PIV experiments are conducted in low speed flow of D_4 vapours induced by a rotating disk. The seeding technique of evaporating the suspension of D_4 and 170 nm titania tracer particles will be tested. Scattering property of these tracer particles will also be verified by calculating average SNR of signals from particles. A short discussion on the quality of PIV measurements will be presented.

- PIV analysis of compressible vapour flows: Supersonic nozzle flow of MM is compared with that of air. Large density gradients that results in large refractive index gradients are reported. Aero-optical distortions due to refractive index gradients will be formulated. Tracer particle response characteristics in high-speed MM flow will be discussed. A conceptual seeding technique will be proposed that can operate in high pressure vapour tunnels.
- Results: A short discussion on the mean velocity fields measured in chapter-3 will be presented. Preliminary estimations of errors due to aero-optical distortions in a nozzle designed for MM will be presented. Probable methods for correcting those errors will be presented.
- Conclusion: Conclusions are drawn from the results and possible modifications to the conventional set-up is recommended. Future projects essential for a successful PIV campaign in non-ideal compressible fluid flow are recommended.

2

THEORETICAL BACKGROUND

2.1. WORKING FLUID PROPERTIES

As discussed in Chapter 1 the ideal gas equation of state cannot be used to obtain the thermodynamic properties of the fluids of interest. The thermodynamic properties namely, temperature (T), pressure (p), and density (ρ) of the fluids are obtained from the thermodynamic library REFPROP that uses the modified Span-Wagner form of multi-parameter equation of state [16, 18]. Another set of properties relevant to these fluids are the transport properties namely, viscosity and thermal conductivity. Out of the two transport properties only the viscosity of the fluids of interest are discussed in detail due to its relevance to the study of motion of tracer particles in fluid medium. It is desirable that the variation in viscosity is well within one order of magnitude to avoid any large variation in flow Reynold's number over tracer particles. Optical properties are also of interest to speculate any potential corruption of signals from the tracer particle resulting in inaccurate measurements.

2.1.1. VISCOSITY MODELS

Numerous viscosity models exist in the literature which are derived by modifying or enhancing the viscosity expression given by Chapman-Enskog theory. Chapman-Enskog gives the viscosity of gases at low density with no internal degree of freedom and is a termed as dilute gas viscosity (μ^*) which is given by the Eqn. 2.1, where, m is the mass of a molecule, k_B is the Boltzmann constant, T is the absolute temperature, the reduced temperature is defined as $T^* = \frac{k_B T}{\varepsilon}$, υ and ε are the potential distance and energy parameter, and $\Omega^*(2,2)$ is the reduced collision integral which is related to the potential model of the molecule [33, 34].

$$\mu^*(T) = \frac{5}{16}\frac{(\pi m k_B T)^{1/2}}{\pi \upsilon^2 \Omega^*(2,2) T^*} \tag{2.1}$$

The dilute gas viscosity is only function of temperature and does not take into account intra-molecular and inter-molecular complexity of fluids of interest here [34]. Therefore, various modifications have been applied to predict viscosity of different fluids as a function of its thermodynamic properties. One such model is Extended Corresponding State Model that uses a fairly accurate model of viscosity for one fluid (reference fluid) to predict the viscosity of another fluid at a synonymous thermodynamic state. This model is discussed in detail below.

EXTENDED CORRESPONDING STATES MODEL

Fluid viscosity at different thermodynamic points is computed using REFPROP which uses an extended corresponding states method developed by Huber et. al. 2003. [35] for dense gases and refrigerants. The viscosity of a pure fluid is represented as a sum of dilute gas viscosity (function of T only) and a residual viscosity term (function of T and ρ or P) as shown by Equation 2.2. The corresponding states principle is then applied to the residual viscosity term as shown in Equation 2.3.

$$\mu(T,\rho) = \mu^*(T) + \Delta\mu(T,\rho) \tag{2.2}$$

$$\Delta\mu(T,\rho) = \Delta\mu_0(T_0,\rho_0) F_\mu(T,\rho) \tag{2.3}$$

The viscosity of the reference fluid is calculated at thermodynamic point (T_0, ρ_0) which conform to the thermodynamic point of the fluid of interest by following Equations,

$$T_0 = T/f \tag{2.4}$$

$$\rho_0 = \rho h \tag{2.5}$$

Where, f and h are called equivalent substance reducing ratios and are given as below,

$$f = \frac{T_c}{T_{c0}}\theta_s \tag{2.6}$$

$$h = \frac{\rho_{c0}}{\rho_c}\phi_s \tag{2.7}$$

Here, θ_s and ϕ_s are called the shape factors and are functions of temperature and density. Huber et. al. used the "exact" shape factor method, where the thermodynamic surfaces of one fluid is mapped onto another to directly find the conformed thermodynamic points [35]. The factor F_μ in Eqn. 2.3 is given by Eqn. 2.8. Residual viscosity of the reference fluid is calculated using a correlation established by Huber et. al. (2003) [35]. It is important to choose a reference fluid that resembles the fluid of interest chemically and structurally. Considering that the ECS method relies on mapping the thermodynamic surface, it is reasonable to assume that the thermodynamic surface of a good reference fluid should resemble the thermodynamic surface of the fluid of interest. If T-S is chosen as the thermodynamic surface then the retrograde of the saturation curve is a good measure of such resemblance. Therefore in this work, the fluid with molecular complexity (given by the Eqn. 2.9) close to that of the fluid of interest (Figure 2.3) is chosen as the reference fluid. In REFPROP the reference fluid for D4 ($\sigma = 51.94$) is dodecane ($\sigma = 48.47$), which is a good choice. However, in REFPROP the reference fluid for MM is chose to be N_2. Therefore, the reference fluid for MM ($\sigma = 28.15$) was changed to a more appropriate fluid nonane ($\sigma = 29.66$), and this modification was verified in a communication with Dr. Huber of NIST via e-mail. The viscosities of MM and D_4 in vapour phase with varying temperature and pressure are calculated and shown below.

$$F_\mu = f^{1/2} h^{-2/3} \left(\frac{M}{M_0}\right)^{1/2} \tag{2.8}$$

$$\sigma = \frac{T_c}{R}\left[\frac{dS_{sat.vap.}}{dT}\right]_{T=0.7T_c} \tag{2.9}$$

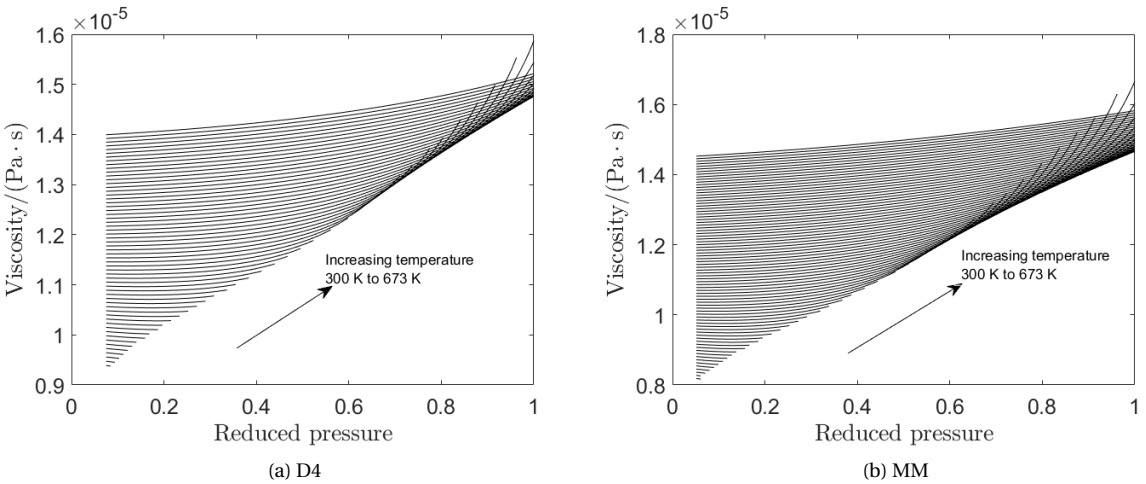

(a) D4 (b) MM

Figure 2.1: Variation of viscosity with pressure.

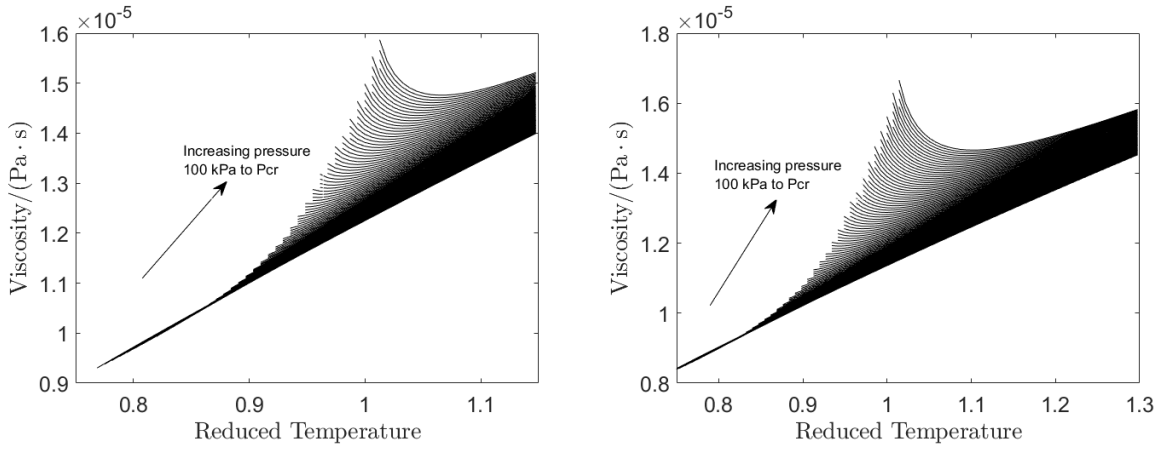

(a) D4 (b) MM

Figure 2.2: Variation of viscosity with temperature.

The isobars in the Figs. 2.2 range from 100 kPa pressure to their respective critical pressures. The isotherms in the Figs. 2.1 ranges from near respective boiling point temperature to 673 K. It can be noticed from Figure 2.1 that for both the fluids the effect of pressure on viscosity becomes more prominent with increasing pressure. Viscosity is almost independent of pressure at lower pressure values (dilute gas region). The trend of viscosity variation with temperature changes completely with significant increase in pressure. Viscosity varies linearly with temperature at lower pressures while at higher pressures the viscosity decreases first and then increases with temperature.

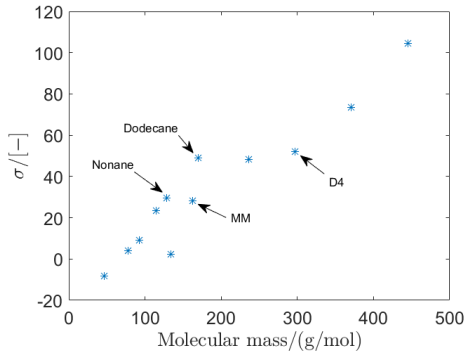

Figure 2.3: Molecular complexity vs Molecular mass

The viscosity varies well within one order of magnitude with the thermodynamic properties in vapour phase. Due to the absence of experimental data for vapour phase viscosity of D4 and MM one cannot judge the accuracy of the viscosity models. A very rough estimate of the uncertainty in viscosity of the reference fluids (dodecane and nonane) is given to be 10% (or higher near critical point) by NIST. Considering that the viscosity models of these reference fluids are also fitted to some experimental data, the uncertainty margin of D_4 and MM is also taken to be 10% in this work.

2.1.2. OPTICAL PROPERTIES

For PIV it is important that laser does not suffer any optical attenuation[1] by the fluid medium drastically or vice versa. Ideally, light must pass through the fluid medium with minimum attenuation and uniform refraction as in the case with homogeneous medium. Both these effects depends on the frequency of the

[1]The electromagnetic radiation can be affected by fluid by absorption and refraction. Loss in the energy of light due to such light matter interaction is called attenuation.

light and molecular structure of the fluid. The most important property of a fluid medium to identify these two effects is the complex refractive index. The complex refractive index consists of a real and an imaginary component as shown in Eqn. 2.10. The real component (n) is the ratio of speed of light in vacuum to the speed of light in the fluid medium. The imaginary component (κ) is called the extinction coefficient and it represents the decay of light intensity passing through the medium. Both the n and κ are not measurable quantities but can be determined from other related properties of the medium which can be measured.

$$\hat{n} = n + i\kappa \tag{2.10}$$

REAL COMPONENT

The real component of Eqn. 2.10 can be determined from molar refractivity (A) measurements that exist in literature (in case of monoatomic species it is called atomic refractivity). Molar refractivity is essentially total polarizablity of one mole of a substance and is given by Eqn. 2.11 [36]. When an electromagnetic field interacts with a molecule the electric field causes the molecule to form a dipole. Molar refractivity is dependent on the real component (n), pressure (p), and temperature (T) of the substance.

$$A = \frac{4\pi}{3} N_A \alpha(n, p, T) \tag{2.11}$$

In the above equation, N_A is Avogadro's number, and α is the mean polarizability of the substance. The mean polarizability of N molecules a substance in a unit volume is given by Eqn. 2.12 which is called Lorentz-Lorenz formula [36].

$$\alpha = \frac{3}{4\pi N} \frac{n^2 - 1}{n^2 + 2} \tag{2.12}$$

If M is the molecular mass of the substance and ρ is density, then Eqns. 2.11 and 2.12 can be used to establish a relation between real component of the refractive index, molar refractivity, and thermodynamic state of the substance, Eqn. 2.13 is the relation established for ideal gases. Only the first equality holds in case of non-ideal gases.

$$A = \frac{M}{\rho} \frac{(n^2 - 1)}{(n^2 + 2)} = \frac{RT}{p} \frac{(n^2 - 1)}{(n^2 + 2)} \tag{2.13}$$

Further, $A_s = \frac{A}{M}$ can be termed as specific refractivity and it remains almost constant under changes in density to a high degree of approximation [37]. Hence, for a given density (ρ) one can determine the real component (n) from Eqn. 2.13. In the field of aerodynamics where the fluid of interest is generally air or ideal gases, an approximation of $n \approx 1$ is made. The definition of specific refractivity along with the approximation when applied to Eqn. 2.13 yields the following equation.

$$n - 1 = \frac{3}{2} A_s \rho \tag{2.14}$$

Equation 2.14 is same as the Gladstone-Dale relation ($n - 1 = K\rho$, where K is Gladstone-Dale constant) given in reference [38]. The compressible effects in organic vapours like $D4$ and MM is higher than that of air and as a result the approximation of $n \approx 1$ may not hold for large densities in comparison to ideal gases. It is suggested to not use Eqn. 2.14 to calculate the real component for high speed flows where density gradients are large. Therefore the specific refractivity (A_s) will be used in this work instead of conventional Gladstone-Dale constant (K). After some algebraic manipulation the real component can be expressed in terms of specific refractivity and density given by Eqn. 2.15

$$n = \sqrt{\frac{2A_s\rho + 1}{1 - A_s\rho}} \tag{2.15}$$

Molar refractivity is generally measured experimentally but one cannot measure for all molecules in engineering applications. There are several theoretical methods to calculate molar refractivity with acceptable error. If the atomic refractivities of the constituent atoms of a molecule is known one can calculate the molar refractivity using Eqn. 2.16 [36], where N_i is the number of atoms of i^{th} species in the molecule and A_i is the atomic refractivity.

$$A = \sum_i A_i N_i \tag{2.16}$$

Atomic refractivity of an atom in different compounds can be different [36]. A detailed description of such deviation in atomic refractivity in different organic compounds is given by Swientoslawski [39]. He mentions that Eqn. 2.16 can be used with an acceptable accuracy as long as the constituent atoms are part of the same group (i.e. if two atoms of same element are bonded with atoms of different elements, the atomic refractivity of the atoms will be different). Due to this issue an alternative method to calculate molar refractivity is through bond refractivities of the bonds present in the molecule. Every bond between two atoms in a molecule is associated a refractivity and is called bond refractivity and sum of all bond refractivities of the molecule gives the molar refractivity. Warrick (1946) mentions a simplified method of using bond refractions which is a modified form of model given by R. O. Sauer [40]. Also, refractivity can be associated to a bond between an atom and a group as well, for example, methyl group is quite frequently occurring group in organosilicon compounds and one can assign bond refractivity to $Si-CH_3$ bond. The D_4 and MM molecules does not contain any atom that is a part of two different groups and one can use atomic refractivities or bond refractivities to calculate molar refractivity with reasonable accuracy. Although, the method of bond refractivity is used in this work to be on the safer side. The bond refractivity data required to calculate the molar refractivity of D_4 and MM is tabulated in the Table 2.1.

Bond	Bond Refractivity/($cm^3 mol^{-1}$)	Reference
$Si-O$	1.75	[40]
$Si-CH_3$	7.573	[40]

Table 2.1: Refractivity data of constituent bonds of D_4 and MM

D_4 consists of eight $Si-O$ bonds and eight $Si-CH_3$ bonds and MM consists of two $Si-O$ bonds and six $Si-CH_3$ bonds. With the information above and known molecular masses of our fluid of interest, their optical properties were calculated and can be seen in the Table 2.2, the values reported here are for light of wavelength close to that of 527 nm and they will remain approximately constant for almost all wavelengths in the in visible spectrum [38].

Fluid	$A/(cm^3 mol^{-1})$	Calculated $A/(cm^3 mol^{-1})$	Error	$A_s/(cm^3 g^{-1})$	Reference
D_4	74.47	74.584	+0.15%	0.251	[40, 41]
MM	-	48.938	-	0.301	[40]
Air	6.66	-	-	0.23	[38]

Table 2.2: Optical properties of D_4 and MM

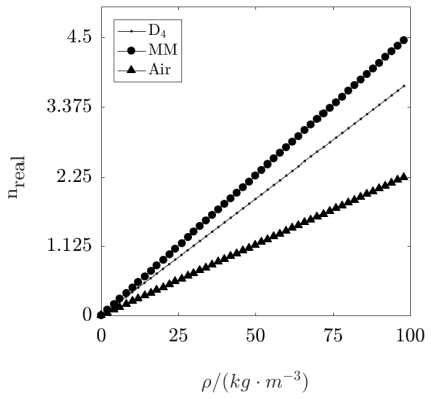

Figure 2.4: Real component vs. density

In a high speed flow the density of organic vapours has larger variation than that in air. The Fig. 2.4 shows the variation of real component of refractive index with the variation of density. It should be noted

that effect of temperature is not taken into account during the calculation of molar refractivity due to the weak dependence [42].

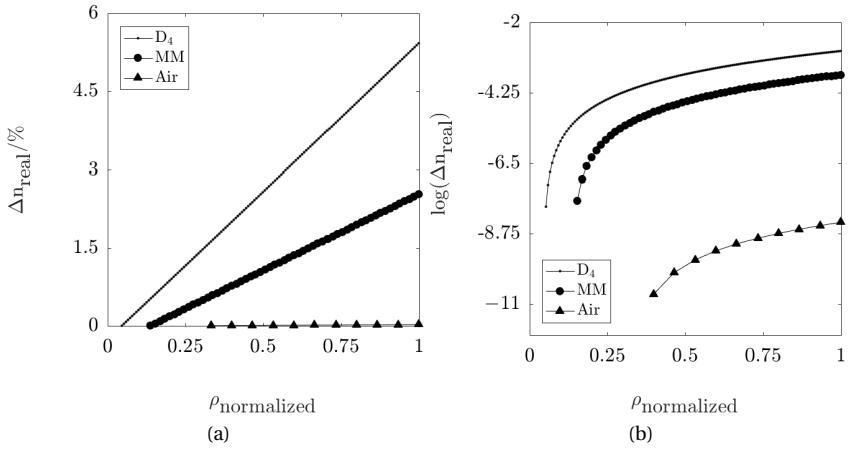

Figure 2.5: Change in real component of the refractive index with density in a typical nozzle flow case.

According to Fainberg and Miller (1965) the effect of temperature on molar refractivity can be of the order of $0.005 - 0.02\%/°C$ for flourine containing perhalo compounds [42]. Hence, it is reasonable to assume that by not accounting the change in molar refractivity due to temperature does not bring in large errors in calculation of the real component [43]. Comparison of the magnitude of change in real component in a typical compressible nozzle flow case is shown in Fig. 2.5a, where the percentage change of real component due to density variation is shown. Density on horizontal axis is normalized with the maximum value of the density observed in the compressible flow (i.e. at the throat). To appreciate the comparison of dense vapour and air, Fig. 2.5b shows the logarithm of the percentage change of real component vs. the normalized density.

IMAGINARY COMPONENT

There is always some amount of attenuation of light intensity primarily due to absorption and scattering when it passes through a medium. High amount of light attenuation is not desired for laser based diagnostic techniques. The imaginary part (or the extinction coefficient κ) gives an estimate of the decrease in light intensity due to the attenuation. When the complex refractive index is substituted in the electric field ($E = \mathrm{Re}[E_0 e^{i(\hat{k}z-\omega t)}]$) of a plane electromagnetic wave using the relation between complex refractive index ($\hat{n}$) and complex wave number ($\hat{k}$), i.e. $\hat{k} = 2\pi\hat{n}/\lambda$, we get the Eqn. 2.17.

$$E = \mathrm{Re}[E_0 e^{i(2\pi(n+i\kappa)z/\lambda-\omega t)}] = e^{-2\pi\kappa z/\lambda}\mathrm{Re}[E_0 e^{i(kz-\omega t)}] \tag{2.17}$$

The Eqn. 2.17 shows an exponential decay term which involves κ. This exponential decay of light is better described by the Beer-Lambert law. Intensity of electromagnetic radiation is directly proportional to the square of the electric field and hence the decay term becomes $e^{-4\pi\kappa z/\lambda}$. The term $4\pi\kappa/\lambda$ is defined as the attenuation coefficient. The inverse of the attenuation coefficient is called the penetration depth, which is the length when light intensity is reduced to $1/e$ of the incident intensity. Therefore, by measuring the decrease in light intensity due to a known volume of substance through a known depth, one can estimate the complex component of the refractive index. But such measurements for the fluids of interest has not been done yet, therefore, we rely on the observed transparency of the fluids in liquid phase and assume the transmittance to be sufficient in the vapour phase as well. Moreover, due to the extinction coefficient's strong dependence on density, the measurement in liquid phase cannot be used for vapour phase. From this point the real complex of the refractive index simply will be referred to as the refractive index.

2.2. BASICS OF PIV

The principle of PIV is based on determining the displacement of small tracer particles introduced in the flow in a small time interval. Consider the Fig. 2.6 that shows the basic implementation of the PIV technique [6]. The initial and final position of the tracer particles in the given time interval is determined by capturing the

images of the tracer particles at two time instances separated by the given time interval. The tracer particles are illuminated by a thin sheet of light that is generated from a pulsed light source. Generally, a double-head pulsed laser is used as the light source which is synchronised with a high-speed imaging system such that the illumination and camera exposure is done simultaneously. The time interval between two consecutive pulses of light is called the pulse separation ($\Delta t_p = t' - t$) and the time for which each pulse lasts is called the pulse duration.

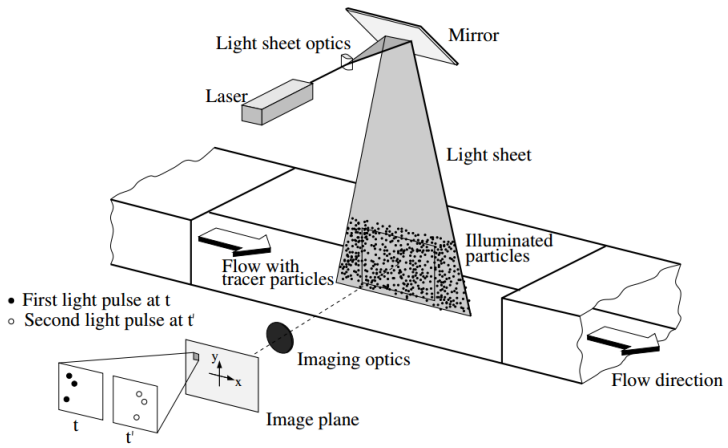

Figure 2.6: Schematic depicting the application of the PIV technique[6].

The captured images are then divided into smaller interrogation windows and the average displacement of the particles within the window is calculated by cross-correlating the corresponding interrogation windows of the image pair as shown in the Fig. 2.7. The peak of the cross-correlation map indicates the final position of the average particle displacement. The size of the interrogation window is chosen such that adequate amount of particles are captured to obtain a satisfactory correlation signal.

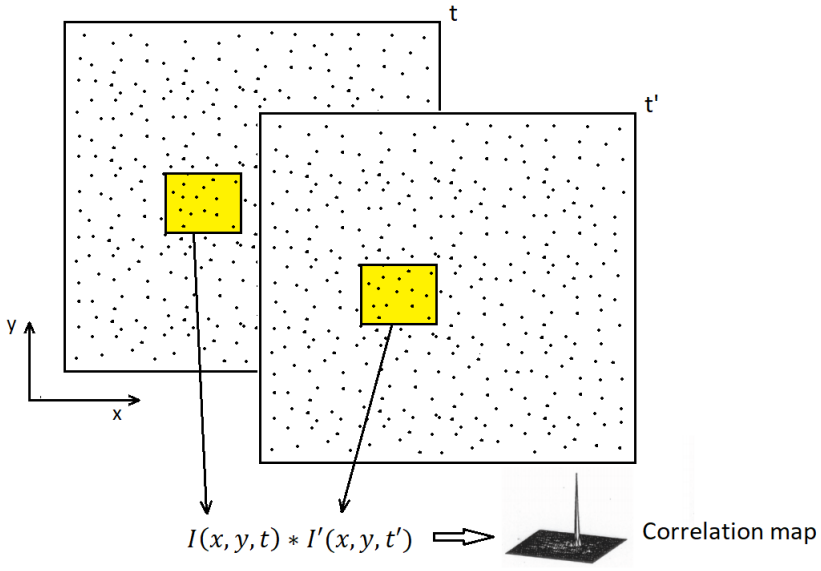

Figure 2.7: Cross-correlating the image pair.

Important design aspects that should be considered for PIV application are the choice of tracer particles, seeding system (to introduce tracer particles into the flow), and the imaging optics. Following subsection discusses the accuracy of tracer particles to follow the flow and commonly used seeding systems for gas flows.

2.2.1. EQUATION OF MOTION FOR TRACER PARTICLES

The tracer particles seeded in the flow should follow the flow accurately, i.e. ideally there should not be any slip between the fluid and the particle. To better understand the motion of tracer particle inside a flow field, it is important to formulate the equation of motion of tracer particle in the flow that takes into account all the forces experienced by the tracer particle. One such formulation is the Basset-Boussinesq-Oseen's (BBO) equation of motion of a sphere settling in a fluid flow and later extendend by Corrsin and Lumley. An extended form of BBO equation (Eqn. 2.18) was treated extensively by Maxey and Riley (1982) to study the motion of spherical particle in a non-uniform flow [44].

$$m_p \frac{d\vec{u}_p}{dt} = \underbrace{3\pi d_p \mu(\vec{u}_f - \vec{u}_p)}_{\text{Drag of Sphere}} + \underbrace{\frac{1}{6}\pi d_p^3 \rho_f \frac{D\vec{u}_f}{Dt}}_{\text{Pressure Gradient}} + \underbrace{\frac{1}{6}\pi d_p^3(\rho_p - \rho_f)g}_{\text{The Gravity}} + \underbrace{\frac{1}{12}\pi d_p^3 \rho_f \frac{d}{dt}(\vec{u}_f - \vec{u}_p)}_{\text{Virtual Mass}} - \underbrace{\frac{3}{2}\pi d_p^2 \mu \int_0^t \left(\frac{d/d\tau(\vec{u}_p - \vec{u}_f)}{\sqrt{\pi\mu(t-\tau)/\rho_f}} \right) d\tau}_{\text{Basset history term}} \tag{2.18}$$

Here, u_p, u_f, ρ_p, ρ_f, and μ denotes the velocity, density of fluid and particles, and viscosity of the fluid respectively. The operator d/dt and D/Dt are the total derivatives (or material derivative) of the particle and the fluid element that is replaced by the particle respectively. The slip/relative velocity of a particle is defined as follows:

$$\vec{u}_s = \vec{u}_p - \vec{u}_f$$

where $\vec{u}_p$ is the instantaneous particle center-of-mass velocity, and $\vec{u}_f$ is a velocity which is representative of the local instantaneous fluid velocity field. According to Newton's second law of motion the left hand side of Equation 2.18 is the product of particle mass and corresponding acceleration, which is equal to the impressed forces acting on the particle. These are the drag of a sphere in the flow, the gravity, the pressure gradient force due to the displaced fluid, the virtual mass term and the Basset history term. It is extremely difficult to solve the complete equation of motion, therefore, certain approximations are necessary. In the following subsection we compare the order of magnitude of the terms in equation of motion and neglect less significant terms.

2.2.2. DIMENSIONAL ANALYSIS OF BBO EQUATION

An estimate of the order of magnitudes of the terms of Eqn. 2.18 is obtained by dimensional analysis, i.e., the three differential variables position, time, and velocity are non-dimensionalised and substituted to Eqn. 2.18. Lang (1999) uses Eqn. 2.18 to investigate the relative significance of each term in high speed flows by non-dimensionalizing it, which results in Eqn. 2.19 [45]. The variables were non-dimensionalised in the following manner,

$$\bar{x} = \frac{x}{L} \qquad \bar{t} = \frac{t}{1/\Omega} = t\Omega \qquad \bar{u}_p = \frac{u_p}{u_{p,0}} \qquad \bar{u}_f = \frac{u_f}{u_{f,0}}$$

The parameters used to non-dimensionalize are length scale of interest of the flow around the particle (L), frequency scale of interest of the flow around the particle (Ω), velocities of fluid and particle at the starting location ($u_{f,0}$ and $u_{p,0}$ respectively). After expanding the total derivatives and substituting the above variables in terms of their non-dimensional form, the following form of the BBO equation is obtained,

$$\frac{\partial \bar{u}_{p,x}}{\partial \bar{t}} + \frac{u_{p,x_0}}{\Omega L}\bar{u}_{p,x}\frac{\partial \bar{u}_{p,x}}{\partial \bar{x}} + \frac{u_{p,y_0}}{\Omega H}\bar{u}_{p,y}\frac{\partial \bar{u}_{p,x}}{\partial \bar{y}} = \frac{18\mu}{\rho_p d_p^2 \Omega}\frac{(u_f-u_p)_{x_0}}{u_{p,x_0}}\overline{(u_f-u_p)}_x + \frac{(\rho_p-\rho_f)}{\rho_p}\frac{g}{\Omega u_{p,x_0}} + \frac{\rho_f}{\rho_p}\left(\frac{u_{f,x_0}}{u_{p,x_0}}\frac{\partial \bar{u}_{f,x}}{\partial \bar{t}} + \frac{u_{f,x_0}}{\Omega L}\bar{u}_{p,x}\frac{\partial \bar{u}_{f,x}}{\partial \bar{x}} \frac{u_{f,x_0}u_{p,y_0}}{\Omega L u_{p,x_0}\bar{u}_{p,y}}\frac{\partial \bar{u}_{f,x}}{\partial \bar{y}}\right) + \frac{1}{2}\frac{\rho_f}{\rho_p}\left(\frac{(u_f-u_p)_{x_0}}{u_{p,x_0}}\frac{\partial \overline{(u_f-u_p)}_x}{\partial \bar{t}} + \frac{(u_f-u_p)_{x_0}}{\Omega L}\bar{u}_{p,x}\frac{\partial \overline{(u_f-u_p)}_x}{\partial \bar{x}} + \frac{u_{p,y_0}}{u_{p,x_0}}\frac{(u_f-u_p)_{x_0}}{\Omega L}\bar{u}_{p,y}\frac{\overline{(u_f-u_p)}_x}{\partial \bar{y}}\right) - \frac{18\mu}{\rho_p d_p^2\Omega}\sqrt{\frac{\rho_f d_p^2\Omega}{4\pi\mu}}\frac{(u_p-u_f)_{x_0}}{u_{p,x_0}}\int \frac{\frac{\partial}{\partial \bar{\tau}}\overline{(u_p(\tau)-u_f(x,t))}_x}{\sqrt{t-\tau}} \tag{2.19}$$

The above form yields five non-dimensional parameter which governs the relative significance of the force terms, and they are $\pi_1 = \frac{\rho_p d_p^2 \Omega}{18\mu}$, $\pi_2 = \frac{\rho_f}{\rho_p}$, $\pi_3 = \frac{(u_f-u_p)_{x_0}}{u_{p,x_0}}$, $\pi_4 = \frac{(u_f-u_p)_{x_0}}{\Omega L}$, and $\pi_5 = \sqrt{\frac{\rho_f d_p^2\Omega}{4\pi\mu}}$. According to Lang (1999), for solid tracer particles of density much higher than fluid, all the non-dimensional parameters can be neglected in comparison to π_1 [45]. Using this manipulation, the equation of motion can be reduced to much simplified form shown in Eqn. 2.20. Where Re_p is the relative particle Reynold's number and is defined as $Re_p = \frac{\rho_f u_s d_p}{\mu} = \frac{u_s d_p}{\nu}$ and C_D is the drag coefficient of the particle.

$$\frac{d\vec{u}_p}{dt} = \frac{3}{4}C_D Re_p \frac{\mu}{\rho_p d_p^2}(\vec{u}_f - \vec{u}_p) \tag{2.20}$$

LOW RELATIVE REYNOLD'S NUMBER

For high density ratio ($\frac{\rho_p}{\rho_f} >> 1$), and low relative Reynold's number ($Re_p < 1$) which is a good assumption for low speed flows, the C_D can be expressed as shown by the Eqn. 2.21 which prescribed by Melling (1997)[7].

$$C_D = \frac{24}{Re_p} \tag{2.21}$$

On substituting the drag coefficient as given by the expression above into the Eqn. 2.20, it simplifies to a separable first order linear differential equation of the form $(\dot{x}+c_1(x-c_2)=0)$ which can be solved analytically and the solution is given by the Eqn. 2.22 where $C = \frac{18\mu}{\rho_p d_p^2}$.

$$\frac{u_f - u_p}{u_f - u_{p,t=0}} = e^{-Ct} \tag{2.22}$$

The constant C determines how quickly the particle catches up to the velocity of the fluid surround it and therefore the inverse of it is referred to as particle response time or particle relaxation time ($\tau_p = \frac{1}{C}$). More accurately the particle response time is defined as the time after which the particle achieves $1-e$ (63%) of the change occurred in the fluid velocity. And the distance travelled by the particle during this interval is called the particle relaxation distance (ξ_p). The τ_p and ξ_p represents the capability of the particle to adapt to the flow conditions and hence gives an estimation of minimum spatial and temporal resolution that the particle can achieve. For low speed flow the particle response time is equal to the time constant of the first order linear differential equation. However, for the high speed flow the formulation of the drag coefficient is significantly different and is a function of Re_p and therefore the solution has to be determined numerically.

$$St = \frac{\tau_\mathrm{p}}{\tau_\mathrm{flow}} \tag{2.23}$$

Another important parameter defined to show the resolving power of a tracer particle is the Stokes' number (St), defined by Eqn. 2.23. It is the ratio of the time response of the particle to the time scale of the flow feature to be resolved. This ratio was encountered in the non-dimensional BBO equation as the non-dimensional parameter π_1, where the frequency scale of Ω is chosen of the flow feature to be resolved. For a particle to resolve the flow feature accurately the Stokes' number with respect to the flow time scale has to be very small ($St << 1$). Higher Stokes' number results in higher uncertainty in the measurement. For application in turbulent flows the particle is chosen such that the time response is much less than the Kolmogorov

time scale (Eqn. 2.24, where τ_L is the largest time scale and Re is the Reynold's number w.r.t. largest length scale L) if the smallest flow feature is to be resolved.

$$\tau_\kappa = \tau_L Re_L^{-\frac{1}{2}} \tag{2.24}$$

HIGH RELATIVE REYNOLD'S NUMBER

As mentioned in the preceding subsection the drag coefficient formulation given by Melling is no longer valid due to high relative particle Reynold's number. For high speed flow several formulation for C_D is proposed in literature and the difference in particle response times calculated using some of these C_D are compared here. Some of these C_D formulations are shown in the Eqns. 2.25 and 2.26 which were proposed by Oseen and Goldstein respectively[46].

$$C_{\text{D,Oseen}} = \frac{24}{Re_p(1+\frac{3}{16}Re_p)} \tag{2.25}$$

$$C_{\text{D,Gold.}} = \frac{24}{Re_p}(1+\frac{3}{16}Re_p - \frac{19}{1280}Re_p^2) \tag{2.26}$$

The Re_p is function of the relative velocity (slip velocity) and it is clear that when one of these formulations are substituted in Eqn. 2.20 the solution for u_p can no longer be given by the Eqn. 2.22. Scarano and Oudheusden uses titania particles of diameter 270 nm to measure velocity field across an obliue shock wave [47]. The velocity normal to the oblique shock undergoes drastic reduction and the tracer particles require finite amount of time to adapt to that change in velocity. The distance travelled by the particle during the time particle velocity achieves $1-\frac{1}{e}$ of the fluid velocity change is termed as relaxation distance. The normalized particle velocity versus the distance travelled normal to the oblique shock wave obtained by solving the Eqn. 2.20 using the drag formulations given by the Eqns. 2.21, 2.25, and 2.26 is compared with the experimental results given by Scarano and Oudheusden and is shown in the Fig. 2.8.

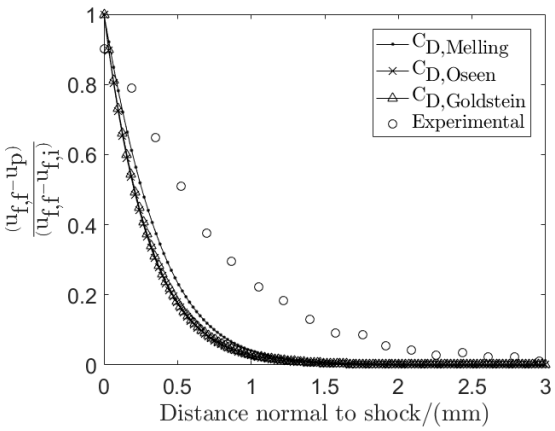

Figure 2.8: Particle relaxation after the shock wave in air.

The relaxation distance obtained by numerical solution of particle equation of motion does not account for real life effects like coagulation of particles and the neglected terms (Sec. 2.2.1), therefore, it is anticipated that the calculated relaxation parameters will be less than the observed. This anticipation can be verified by the comparison shown in the Fig. 2.8 and the resembling trend also proves the validity of the particle motion solver. The Fig. 2.8 shows that the shock wave thickness if deduced from the PIV measurements gives a value of around 1.5-2 mm while that predicted by theoretical calculation is 0.5-1 mm, however the real shock wave thickness is approximately four times the mean free path of the fluid molecule which for air amounts to around 0.2 μm [48], which clearly shows extremely poor capability of PIV in resolving shock waves.

2.2.3. SEEDING STRATEGIES FOR GASEOUS FLOWS

It clear from the previous section that the main factors that affects the accuracy of tracer particles to follow the flow is the density and size of the tracer particle. Other factors that are considered before choosing a tracer particles is the health concerns, availability, and ease of dispersion. Due to these reasons commonly used tracer particles are metal oxides, oils droplets, glass spheres, gas bubbles etc., properties of some of these is presented in the Tab. 2.3.

Type	Material	d_p/μm	$\rho_p/\text{kg}\cdot\text{m}^{-3}$	Boiling point/°C
‘ Solid	Polystyrene	0.5-10	1000	-
	Alumina	0.2-5	3950	2977
	Titania	0.1-5	4000	2972
	Glass micro-spheres	0.2-3	2200-4500	> 1500
	Glass micro-balloons	30-100	< 1000	> 1500
	Granules for synthetic coatings	10-50	-	-
	Dioctylphathalate	1-10	990	385
	Smoke	< 1	-	-
Liquid	Different oils	0.5-10	800-1000	100-300
	Di-ethyl-hexyl-sebacate	0.5-1.5	912	< 250
	Helium-filled soap bubbles	1000-3000	< 1	< 100

Table 2.3: Commonly used tracer particles in gas flows [6]

Due to high temperatures conditions the liquid seeding materials cannot be used. Among the solid seeding materials, polystyrene melts at around 250 °C and hence cannot be chosen. Among the remaining choices, metal oxides alumina and titania are easily and cheaply available therefore are chosen as the seeding materials. Other characteristic of metal oxides like inertness and high melting point works in favour of application in high temperature unconventional medium. Some common strategies used to seed metal oxide tracer particles in the gas flows are discussed in following subsections.

SEEDING BY FLUIDIZATION

Very commonly used technique for seeding solid tracer particles in gas flows is by using fluidized bed. The Fig. 2.9 shows typical designs used to generate solid seeding particles from their powdered form. A powder of metal oxide is suspended on a porous plate (bed) and the fluidized aerosol is drawn from the top [7].

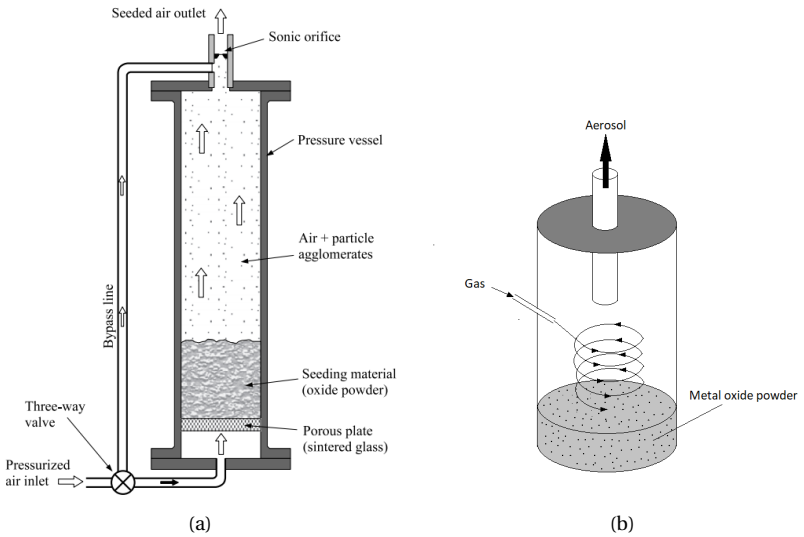

Figure 2.9: Fluidization of metal oxide powder[6, 7].

The dispersed particles generated by the design shown in the Fig. 2.9a are generally several times larger than their nominal size due to coagulation that depends on the humidity of the gas used to fluidize the powder. Therefore, the gas is generally dried before it is sent for fluidization. Due to coagulation the number

density (N) of the tracer particles tend to reduce. In addition, the rate of coagulation increases as N^2, making this effect a matter of concern within the generator [7]. An additional Cyclone of gas can be introduced to improve the quality of aerosol as shown in the Fig. 2.9b, which was used by Glass and Kennedy (1997) to obtain 0.1-1 μm alumina particles [49].

SEEDING BY ATOMIZATION

Atomization of a solution or suspension of metal oxide with suitable volatile solvent is also a promising strategy of generating tracer particle aerosols. A set-up shown in the Fig. 2.10a that utilizes Laskin nozzle to atomize the metal oxide + solvent suspension can be used to generate seeding. A thoroughly dispersed low concentration suspension generates a steady concentration of solvent droplets that has metal oxide particles trapped within, which upon evaporation generates almost mono-dispersed particle seeding. The Fig. 2.10b shows an alternative design to Laskin nozzle where a side-ways flow of compressed air through horizontal orifice is used for suction of the metal oxide suspension from the vertical orifice.

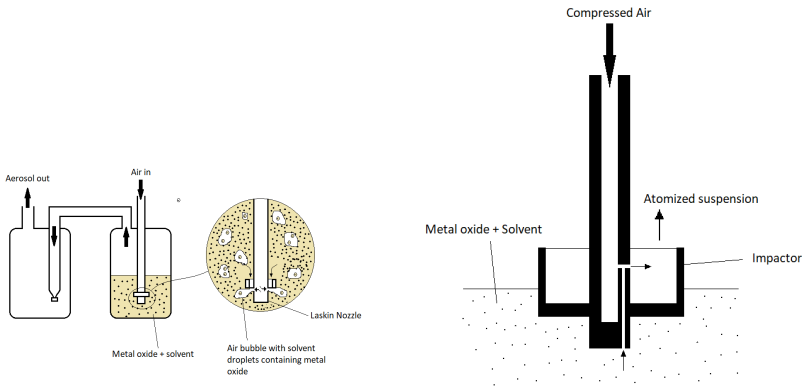

(a) Laskin nozzle (b) Alternate nozzle design

Figure 2.10: Atomization of metal oxide suspension [7].

For application in vapour tunnels, these techniques cannot be used to seed solid particles in dense vapour flows because the contamination of the working fluid cannot be risked and the operating pressures are very high. Considering only the working fluid and the tracer particles are allowed inside the vapour tunnels, only viable option of seeding appears to be evaporation of suspension of D_4 and tracer particles. As already discussed, the tracer particle of choice is smallest available (170 nm) titania particles due to its inert nature, and high temperature tolerance. The purpose of the next chapter is to evaluate the seeding distribution quality obtained by evaporating the suspension of D_4 + 170 nm titania particles and to verify a satisfactory scattering property of the 170 nm titania particles.

3

EXPERIMENTS IN LOW SPEED VAPOUR FLOWS

3.1. THE NIVA APPARATUS

The experimental investigation is performed in an apparatus which is named Non-Intrusive Vapour Analyser (NIVA). Figure 3.1a shows an isometric view of the apparatus together with the instruments. The NIVA was designed to assess the feasibility of laser diagnostic related techniques on vaporised organic media. The fundamental idea of operation is to insert a certain amount of liquid siloxanes (here D4) into the NIVA, vapourize the siloxane, induce a flow and perform measurements. Design parameters of the apparatus, measurement instruments used in the apparatus, and the experiments conducted using the apparatus will be explained in this section.

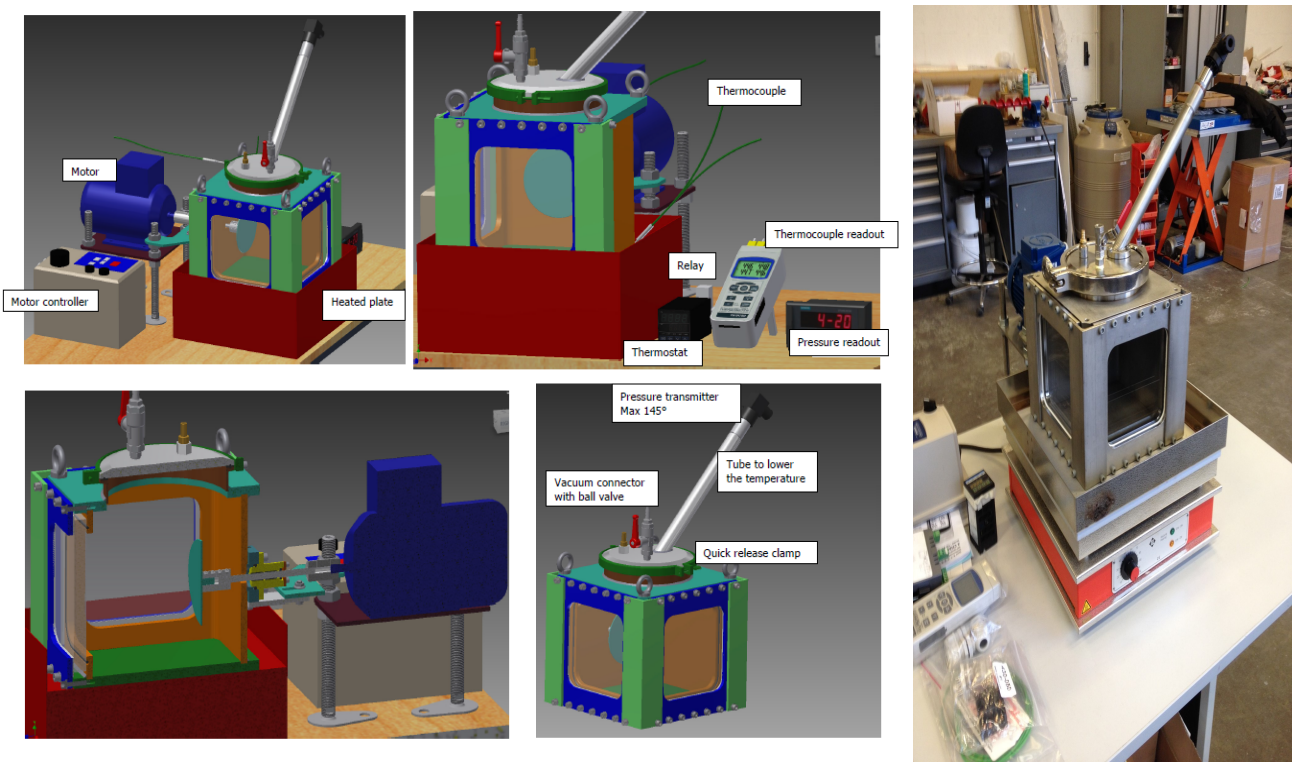

(a) (b)

Figure 3.1: CAD model and realization of NIVA.

The NIVA is a steel box (Figure 3.1b) with two glass windows on adjacent sides for optical access. A metallic shaft that goes through one of the steel wall holds a disk of diameter (D) 10 cm, which will be used to induce a rotating flow. The disk actuator is connected to the motor via flexible junction. The motor is first calibrated (Fig. 3.2) to relate it to the tangential velocity at the disk periphery with the controller display (in Hz).

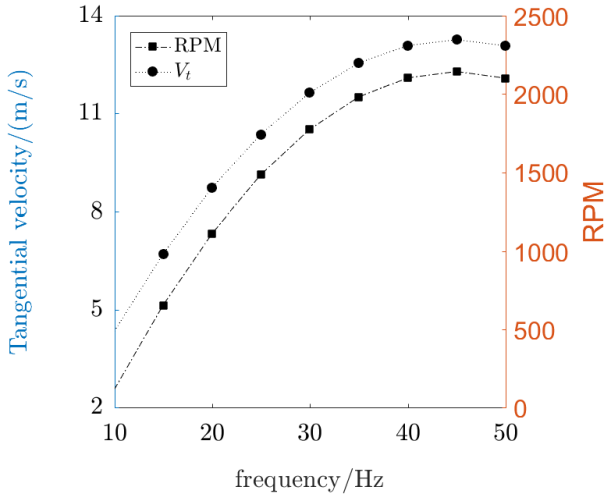

Figure 3.2: Motor calibration curve

The steel box sits on a heating plate (max. power 2.2 kW) which is used to control the temperature inside the box. Two thermocouples, one at the bottom (floor) and one at the top of the box (ceiling) are placed to measure the temperature inside the box. The temperature can be changed by changing the power of the heating plate. Steady heating plate temperature attained by setting it to a certain percentage of maximum power can be seen in Fig. 3.3. The apparatus also accommodates a relay connected to the thermocouple at the floor via a thermostat to automatically switch off the heating plate if the temperatures exceeds a certain threshold (180-190 $^{\circ}C$) set by the user.

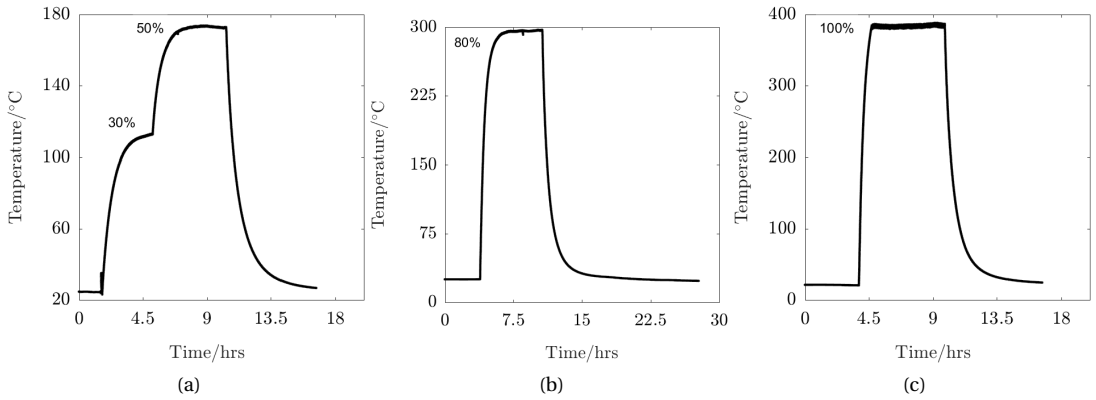

Figure 3.3: Heating plate temperatures curves. Time t = 0 does not correspond to switching on of the heating plate.

An oblique pipe connected through the ceiling also carries a Siemens Sitran P200 pressure transmitter to monitor the pressure inside the box. The maximum working temperature of the sensor is 140$^{\circ}C$, therefore it is placed as far as possible from the heating plate and it also sets the constraint to maximum temperature inside NIVA. The maximum attainable pressure inside NIVA is 2 bar beyond which the safety valve mounted on the lid opens to release pressure.

3.2. PIV MEASUREMENT SET-UP

The vapour flow induced by the rotating disk inside the NIVA was visualized and quantified by PIV. Figure 3.4 shows the schematic of experimental set-up which comprises the NIVA, laser for particle illumination,

and the camera for image acquisition. A LITRON LDY laser was used for the experiments synchronized with Imager Pro HS 4M high speed camera.

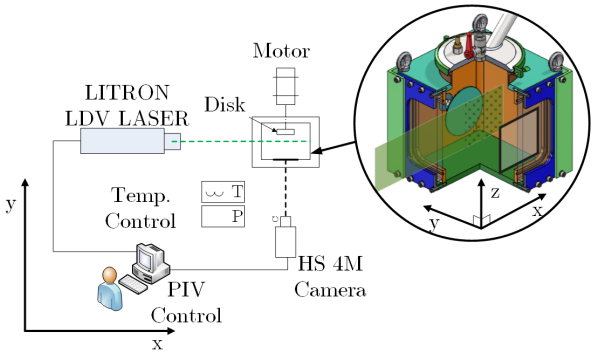

Figure 3.4: The NIVA

3.2.1. SEEDING MATERIAL AND TECHNIQUE

The NIVA is a closed box with no exchange of matter across the boundaries during the its operation and because of that the seeding techniques discussed in Sec. 2.2.3 cannot be implemented. Therefore, the tracer particles were mixed with D_4 prior to its entry and vapourization inside NIVA. The assumption made is that the tracer particles will be carried along with the D_4 vapours during vaporization. The dispersion of tracer particles is further enhanced by switching on the disk rotation.

The liquid seeding materials cannot be used due to the fact that they would not comply with the seeding technique. Therefore, solid seeding material is preferred. Among the solid seeding materials polystyrene and dioctylphthalate cannot be used due its melting point's proximity to the operating temperatures inside the NIVA. Therefore, among the remaining options titania (TiO_2) and alumina (Al_2O_3) are the best options due to its cheap cost and inert nature. Titania particles of mean diameter(d_p) of 170 nm is chosen for the application in NIVA.

To resolve the flow feature of the dimensions of the order of the disk diameter accurately, the particle stokes number (St) w.r.t. time scale of these features should be less than 0.1. The time scale of these flow feature can be estimated as $\tau_{\text{flow}} = \frac{D}{V_t}$, which results in minimum τ_{flow} of 7.7 ms from the rotational speeds shown in the Fig. 3.2. The order of magnitude of the viscosity of D_4 as estimated from the Fig. 2.1a or 2.2a is 10^{-5} Pa·s. The order of magnitude of density of D_4 under constraints mentioned in the Sec. 3.1 is 1. Now, taking the disk rotation of the maximum magnitude from the Fig. 3.2 the estimated relative Reynold's number ($\text{Re}_p = \frac{\rho_f \cdot V_t \cdot d_p}{\mu_f}$) of the flow around the tracer particles at the disk periphery is less than 0.5. Hence, the particle response time can be estimated using the expression $\tau_p = \frac{\rho_p d_p^2}{18\mu_f}$ which results in τ_p equal to 0.64 μs. These estimation of the time scale of the flow feature and particle response time gives a St of the order of 10^{-4}. The St for the lower rotational speed will be even smaller. Therefore, it can be said that the 170 nm Titania particle are suitable for measurements in the NIVA.

3.2.2. LASER AND CAMERA

A LITRON LDY is a double cavity Nd:YLF laser with wavelength of 527 nm. The energy of the laser beam with pulse duration of 5 ns is 400 mJ. The beam output diameter is 7 mm and in the current experiment is shaped into a sheet of thickness 1 mm. The laser is used in synchronization with Imager Pro HS 4M high speed camera. The camera consists of a CCD sensor of resolution of 2016 × 2016 pixels with pixel size of 11 μm. The sensor's dynamic range (bit-depth) is 12 bits (4095 counts). The focal length of the lens used and the $f_\#$ at the time of acquisition was 60 mm and 4 respectively. The data is acquired via a software by LaVision named DaVis version 8.3.0. The mode of data acquisition can be set using DaVis. For the experiments in this work the data was acquired in a single frame time-series mode. In single frame time-series mode the data is acquired at a specific frequency given by user. The inverse of the acquisition frequency is the time difference

between two adjacent images in the data set. From Sec. 3.2.1 the greatest frequency scale of the large flow features is estimated to be 130 Hz and therefore the acquisitions frequency should be atleast 260 Hz. The experiments are conducted using the lowest acquisition frequency setting available in the Laser i.e. 300 Hz. Therefore, the pulse separation (Δt_p) is 3.33 ms.

3.2.3. KEY PARAMETERS OF IMAGING SET-UP

Some parameters that affects the quality of image will be calculated before performing the PIV experiments. These parameters include: magnification factor, digital resolution in pixels per mm; depth of focus of the camera lens; expected particle image size in pixels.

Magnification Factor

$$M_f = \frac{\text{(pixel size)} \cdot \text{(number of pixels in the sensor)}}{\text{field of view}} \tag{3.1}$$

Digital resolution

$$\Delta_{pix} = \frac{\text{number of pixels}}{\text{field of view}} \tag{3.2}$$

Depth of Focus

$$\Delta z_f = 4.88 * f_\#^2 * (\frac{M_f + 1}{M_f})^2 * \lambda \tag{3.3}$$

Particle Image Diameter

$$d_\tau = \sqrt{(M_f d_p)^2 + (2.44\lambda(1 + M_f) f_\#)^2} \tag{3.4}$$

M_f	$\Delta_{pix}/(pixels/mm)$	$\Delta z_f/mm$	$d_\tau/pixels$
0.19	17.08	1.614	0.56

Table 3.1: Optical parameters of imaging.

The depth of focus is larger than laser sheet thickness which is ideal for capturing all particles within laser sheet with sufficient sharpness. Particle image diameter appears smaller than optimum value but the particle image size can be increased, insitu, by slightly defocussing the camera, which is a commonly adopted measure in PIV.

3.2.4. AMOUNT OF FLUID IN NIVA

The amount of liquid D4 to be introduced in the vapour box is calculated using the following procedure,

1. The process in the NIVA is a constant volume process at V_{box} = (20cm)^3 = 8 litres. The controlled parameter is the temperature of the heating plate which is allowed to go to a maximum of $T_{max} = 190°C$ and at that temperature the saturated vapour pressure of D_4 is 1.42 bars and vapour density of 12.1048 kg/m^3 (i.e. approximately 97 ml of D_4 at room temperature). But, at this thermodynamic conditions the vapour is very sensitive to the thermodynamic parameters and condensation can occur at their slightest of fluctuations. Therefore, the aim is to reach a thermodynamic point which is considerably away from the saturation curve as shown by the dome in the Fig. 3.5.

2. Assuming a working temperature (T_{work}) of 130 $°C$ the saturated vapour density obtained is $\rho_{\text{D4,vap}}$ = 2.41 kg/m^3 (obtained using $\rho = f(T, q)$, from REFPROP). The total mass of D_4 of the given density in a volume of 8 litre is approximately 19.3 mg.

3. At room temperature of 25 $°C$ the $\rho_{D_4,liq}$ = 933kg/m^3 and $\rho_{D_4,vap}$ = 0.0164kg/m^3. The mass of D_4 vapour in the at room temperature occupied within the vapour box is therefore 13.12 μg. Hence, the total mass of D_4 required in mg is,

$$m_{D_4,required} = 19.3 - 0.001312 \approx 19.3mg \approx 20.69ml$$

4. The volume of D_4 introduced in the NIVA is therefore 20 ml.

3.3. EXPERIMENTAL PROCEDURE

All the steps taken leading up to the processing of PIV images are presented in this section.

1. The set-up is arranged as shown in Figure 3.4 and the distance between the disk and the laser sheet is kept 1 cm.

2. Titania (TiO_2) powder is mixed with 20 ml of liquid D4 (see Sec. 3.2.4) and poured into the box[1]. The box is closed and vacuumized. The heating plate is switch on to evaporate the D4 + titania suspension, and the tracer particles are carried by the D4 vapour. In the meantime, the motor is switch on and set to a constant rotational frequency to aid the dispersion of tracer particles.

3. Successive images of the measurement plane are acquired by the camera system immediately after the heating plate is switched on to monitor the evaporation process and the tracer particles dispersion. The figure 3.7 shows the states of test section from the beginning to the end of the evaporation process. Stage 1 of the process is when the D_4 starts to boil and a few particles can be seen. Slowly D_4 passes through stage 2-4 where it can be seen that the image gets brighter due to more scatter from more tracer particles. Maximum brightness is observed in stage 5 i.e. on complete evaporation, which is when maximum tracer particles are suspended in the vapour. Time taken to complete the evaporation can be seen in Fig. 3.6 and the stages shown in Fig. 3.7 are captured at regular intervals before the ceiling temperature becomes constant.

4. Thermodynamic parameters of the vapour inside the box were noted. The pressure inside the box at the end of evaporation and at the time of acquisition was 0.238 bars. The temperature of the floor and the ceiling of the box were 190 $^\circ C$ and 130 $^\circ C$ respectively. The Density of D4 at STP is 933 kg/m^3 and that at the time of experiments is 2.3576 kg/m^3. The operating point on the T-s plot of D4 can be seen in Fig. 3.5.

5. The disk rotational frequency is set to 10 Hz and 1000 images are acquired at an acquisition frequency of 300 Hz. The acquisition is repeated for disk rotational frequencies of 20 Hz, 30 Hz and 40 Hz.

6. The rotating disk was switch off and the flow was allowed to settle for 5 mins, and 100 images were taken as a rotational frequency case of 0 Hz.

7. The acquired images are later processed to determine the flow fields. The details about the processing is presented in sections to come.

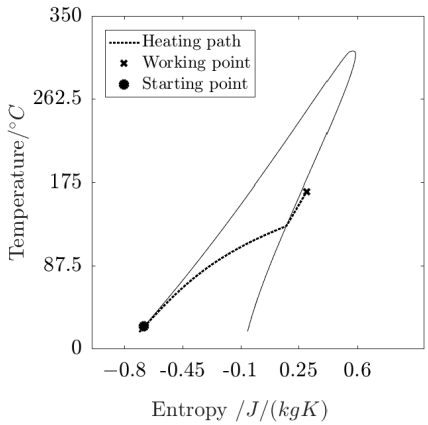

Figure 3.5: Operating point of NIVA.

[1]The amount of titania added to D_4 should be large enough to get sufficient seeding density and small enough to alter the flow features. However, deposition of titania on optical windows was another constraint that limited the amount of particles. Therefore, the amount of titania was decided to be maximum possible before any deposition is observed.

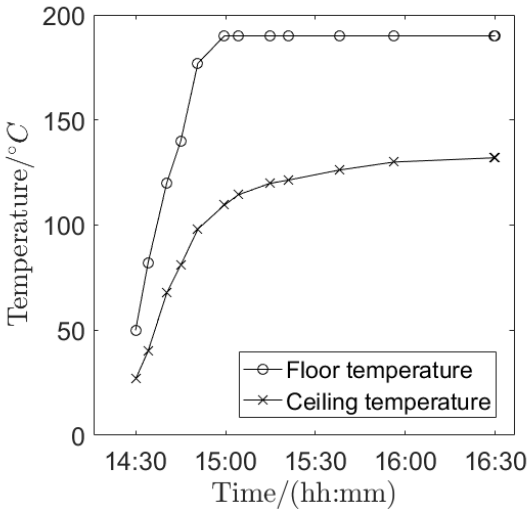

Figure 3.6: Temperature of the floor and ceiling of NIVA.

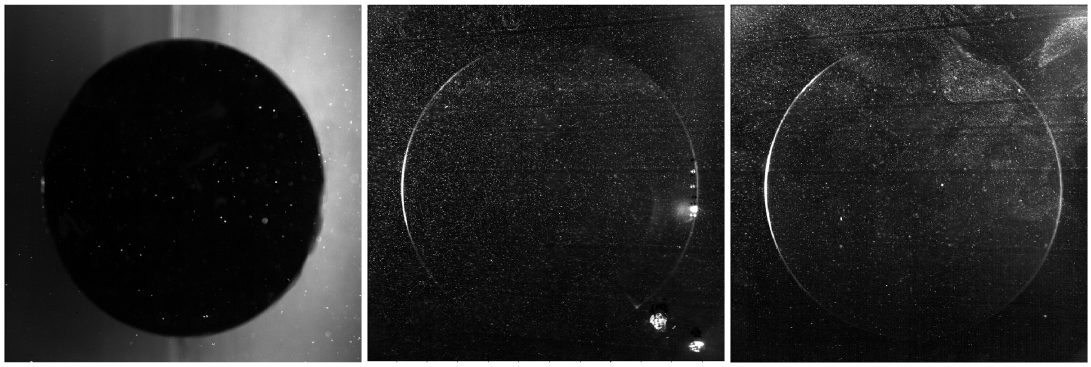

(a) Stage 1 (b) Stage 2 (c) Stage 3

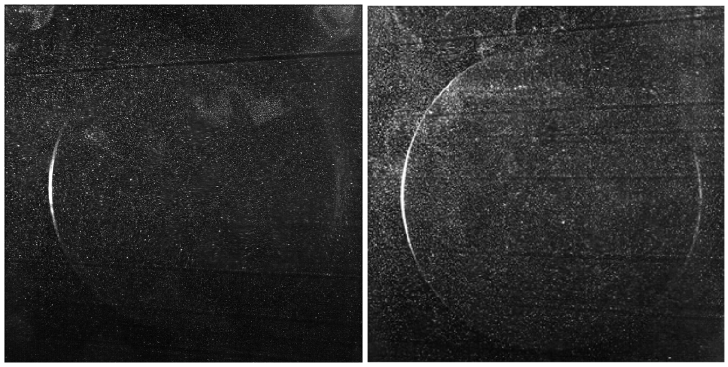

(d) Stage 4 (e) Stage 5

Figure 3.7: Evaporation Process.

3.4. QUALITY OF ACQUIRED IMAGE

Quality of acquired image can be seen from the Figure 3.8 which is an exemplary raw image from the dataset acquired for disk rotational frequency 30 Hz. The histogram of pixel values (Fig. 3.8b) can be used to assess the level of noise and quaility of illumination. According to Raffel et. al. [6] an image of dynamic range of 6-bits (i.e. pixel values 0-127) is sufficient for a good quality measurement.

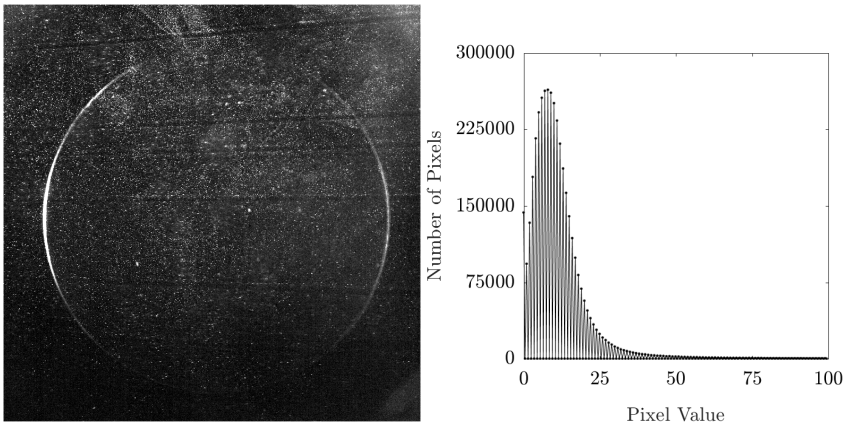

(a) Raw image (b) Histogram

Figure 3.8: The raw data images.

3.4.1. IMAGE PRE-PROCESSING

Initially, time series minimum (TSM) subtraction was used as the image pre-processing tehcnique which is available in DaVis. Along with it, background removal technique by Proper Orthogonal Decomposition (POD) of raw images was also done using algorithm developed by Mendez et. al.[50].

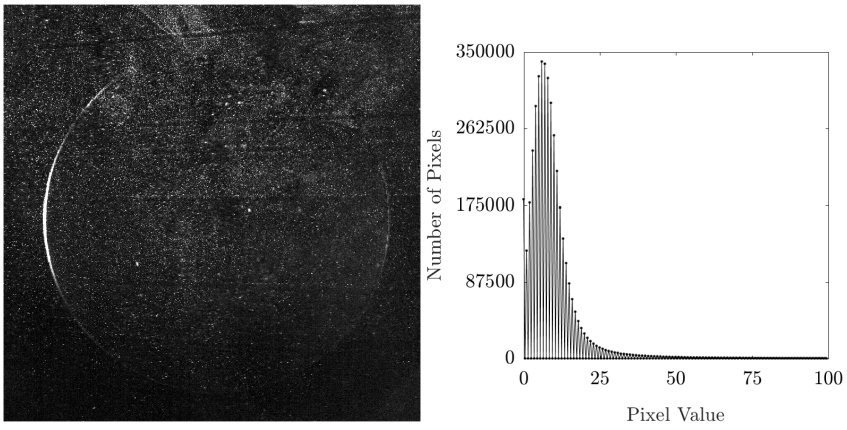

(a) Processed image (b) Histogram

Figure 3.9: Result of subtracting TSM.

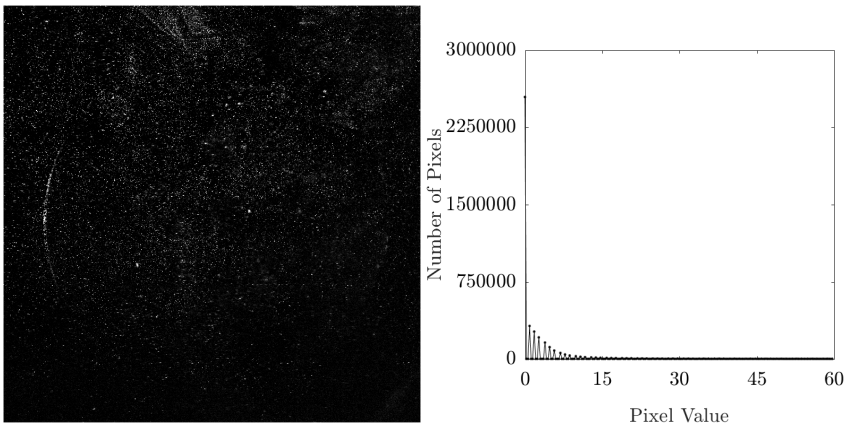

(a) Processed image (b) Histogram

Figure 3.10: Result of POD-based background removal.

Compared to TSM subtraction a better contrast of particle images can be observed after the POD based background removal, which is evident from Fig. 3.10a and 3.9a. The pixel intensity histograms of the images after both de-noising techniques (Figure 3.9b and 3.10b) shows the leftward movement of peak which shows reduction in the noise. The noise reduction in case of POD based background removal is significantly better than that in case of TSM subtraction. A significant removal of the reflections at the periphery of the disk can be observed when POD based background removal is implemented, and therefore this is the chosen technique for image-preprocessing in this work. It is important to note that the noise in raw image is modelled as an additive component to an ideal particle images with black background [50] and can be presented as in Eqn. 3.5.

$$I = I_p + I_b \tag{3.5}$$

The detailed mathematical description of the POD based background removal can be found in App. B. Once the background is removed the images are imported to DaVis using a stepwise procedure described in App. D. After pre-processing of the images, cross-correlation is performed to determine the velocity vectors. Following section deals with assessing the quality of flows measured using PIV.

3.5. QUALITY OF MEASUREMENT

This section will delve into assessing the quality of PIV data acquired for all the disk rotation speeds. Aspects to consider when assessing the quality of PIV data:

1. Sufficient seeding density is required for a reliable detection of the cross-correlation peak. Raffel et. al. suggests to seed the flow such that at least 10 particles are captured within an interrogation window [6]. A typical seeding density for PIV in particles per pixel ranges from 0.02-0.2.

2. The cross-correlation coefficient of the interrogation window should be between 0.6-0.8 for a reliable velocity measure. Lower value of the coefficient suggests lack of seeding or large flow gradients within the interrogation window.

3. After performing cross-correlation on acquired images, number of spurious vectors should be less than 10% of the total number of vectors in the measured vector field. Advanced post-processing techniques are used to further reduce the number of outliers.

4. A quality factor which is referred as Q-factor is defined as $\frac{P_1 - P_{min}}{P_2 - P_{min}}$ for the resulting correlation map from the cross-correlation, where P_1 and P_2 are the peak value and second highest peak value of the correlation map and P_{min} is the minimum value on correlation map. Q-factor value greater than 2 is considered a good correlation signal.

5. The peak lock parameter that reflects the bias of a measurement towards a decimal value should be determined [6, 51]. DaVis calculates the histogram of the occurrence of all decimal values between (0 to 1) in the vector field and provides a parameter "V mod. 0.5" (which is simply referred as peak lock in this work). A measurement with acceptable peak locking bias should have peak lock < 0.1.

6. Spatial resolution of the flow field is also dependent on seeding and gradients present in the flow. Insufficient seeding cannot resolve smaller flow structure. Low seeding density does not allow smaller interrogation windows because enough particles are not captured to get a reliable correlation value. And this results in reduced spatial resolution for a fixed magnification.

7. Relative uncertainty in velocity after cross-correlation should be well within 1%. Another parameter that is associated with a PIV set-up is the dynamic range, which is the ratio of maximum measured velocity to the minimum resolvable velocity. A high dynamic range shows that the measurement technique is capable of measuring a wide range of velocity magnitudes. A dynamic range of 60 or above is considered good. Dynamic range is affected by the spatial resolution which again depends on seeding.

All the aspects discussed above demonstrates the quality of measured data using PIV. Therefore, these aspects will be investigated with regards to the measurements done in NIVA, starting with evaluation of seeding distribution in the following subsection.

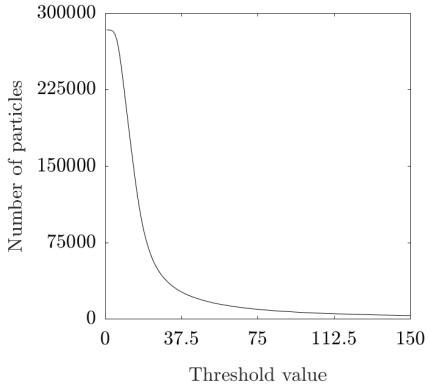

Figure 3.11: Number of particles detected vs. chosen threshold value.

3.5.1. SEEDING DISTRIBUTION

The Particle Seeding Density in a PIV image is expressed as the number of particles per pixel (ppp). A MATLAB script is used to detect the particles by taking a threshold intensity value as input. Each particle image is generally a group of 2 or more pixels and the highest (peak) pixel value of the group is used to represent the particle. The script allows one to calculate all the particles with peak pixel values above a certain threshold and values below threshold is considered as noise. Therefore, it is important to choose a threshold value below which a particle is practically impossible indistinguishable from the image noise. Considering that seeding is sparse enough (to not affect the flow) it can be said that most of the pixels in the image will have the zero value or a small non-zero value due to noise. From Figure 3.8b it can be said that most of the low intenisty noise pixel values are accommodated below 25. Hence, a threshold of 25 is chosen to estimate the number of particles. Figure 3.11 above shows the number of particles detected vs. the threshold value, from which it can be observed a steep decrease in number of particles detected for threshold between 6 and 25 separated the particles from noise.

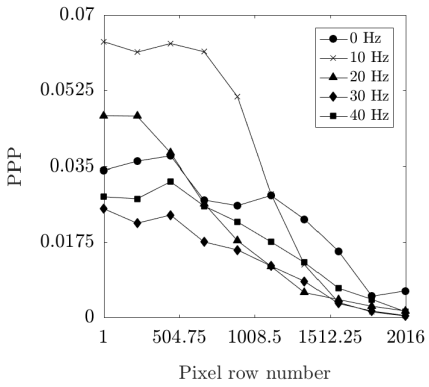

Figure 3.12: Seeding density profile in vertical direction.

The number of particles detected in the image shown by Figure 3.8a is 52144. The total number of pixels in the sensor are 2016X2016, therefore the average seeding density is 0.0128 ppp (typical seeding density lie between 0.02-0.2 ppp [6]). With this seeding density value, approximately 13 particles are accommodated in a 32X32 interrogation window, and 52 for 64X64 interrogation window.

Although the seeding in the Figure 3.8a is more or less uniform it can be noted that there is significant lack of seeding at the bottom. One can also observe in Figure 3.12 that the seeding density decreases as one goes towards the bottom of the box. There is not enough evidences that direct to a specific cause of this homogeneity, but one could suspect the vertical temperature gradient (Fig. 3.6) to be a probable cause.

Using similar calculations shown above, the seeding density of different cases were calculated and tabulated in Tab. 3.2 along with average signal-to-noise ratio (SNR), and source density (N_s) of the PIV images. The threshold value is taken as the noise level and the average peak intensity of particle images is divided by the threshold to estimate the average SNR of the PIV images. The N_s signifies the compactness of the particles in the PIV images. $N_s < 1$ suggests that particles does not overlap each other.

Disk speed/(Hz)	0	10	20	30	40
threshold	20	20	10	25	25
Seeding Density/ppp	0.0234	0.0343	0.0198	0.0128	0.0176
N_s	0.37	0.58	0.17	0.22	0.22
SNR	2.56	6.27	2.70	2.50	2.82

Table 3.2: Threshold value to detect particles, seeding density in ppp, source density (N_s), Average SNR.

Once the seeding quality is evaluated the images need to be processed to obtain the velocity vector field. The image processing involves cross-correlation of consecutive PIV images to obtain instantaneous fields from which the mean velocity field can be calculated. The following section discusses the cross-correlation of the PIV images.

3.5.2. CROSS-CORRELATION COEFFICIENT

After using the pre-processing technique mentioned in Sect. 3.4.1 the images were processed using multi-grid iterative cross-correlation algorithm available in LaVision DaVis. Four iterations of a larger window size and a refined window size (final window size) each were used to calculate velocity. The overlap used during the iterations is 50 and 75 percent respectivey. The Fig. D.1 shows the settings in LaVision DaVis used to perform the above mentioned cross-correlation.

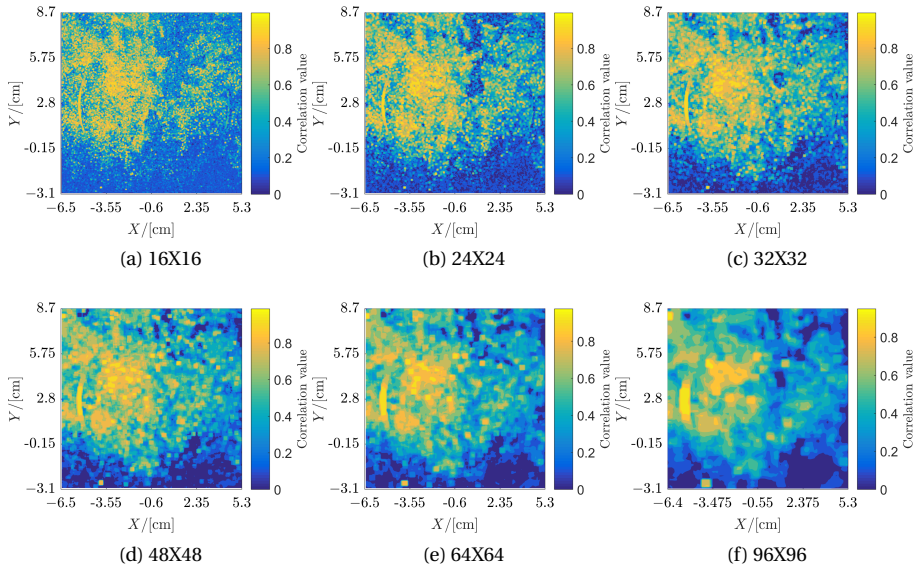

(a) 16X16 (b) 24X24 (c) 32X32

(d) 48X48 (e) 64X64 (f) 96X96

Figure 3.13: Correlation values after processing images using interrogation window of different sizes.

As discussed, the quality of vectors can be assessed by the peak value of the correlation map or simply referred to as correlation value. But one has to be careful about associating the quality of vector just by the means of correlation value. Ideally, a correlation value of 0.6-0.8 is considered a good value. But, the correlation value can be low in presence of strong gradients within the interrogation window and in such a situation the smaller flow features are not resolved. Therefore, the interrogation window size should be small enough to resolve smaller flow features and large enough to capture sufficient particles to get a reliable correlation. Also, in case of significant out of plane motion, the correlation value can be lower than expected. In case of

flow due to rotating disk, there exists a strong velocity component along the disk axis i.e. out of PIV measurement plane [52].

The Fig. 3.13 shows the field of cross-correlation coefficient field obtain by performing cross-correlation using different interrogation window sizes on PIV images from 30 Hz case. The values are ideal in most of the region except at the bottom (i.e. Y < -0.15 cm) where seeding is very low. The corresponding vector field is shown in Fig. 3.14 which is the instantaneous velocity field at time t = 0s. Apart the cross-correlation coefficient, the amount of outliers, Q-factor, and peak lock also signifies quality of the measurement and are discussed in the following subsection.

3.5.3. OUTLIERS, Q-FACTOR, AND PEAK LOCK

Normalized Median Test (NMT) is a statistical test used to verify whether or not a particular vector is an outlier. DaVis provides the information about the parameters like the amount of outliers, average Q-factor, and peak lock of a vector field. These information for the instantaneous vector field at t = 0s obtained for the varying disk rotational speed and varying interrogation window sizes is presented in Tab. 3.3. The mathematical description of the NMT is described in the next paragraph.

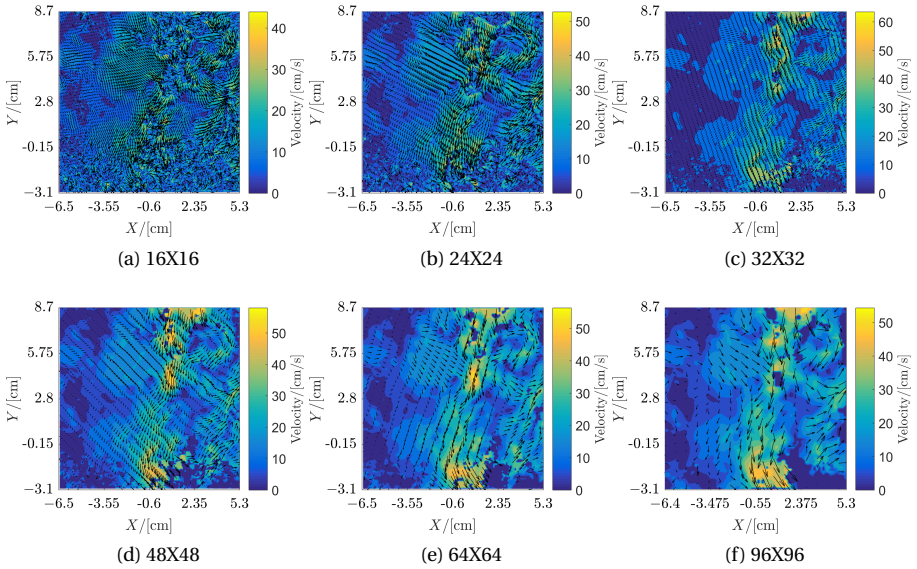

(a) 16X16 (b) 24X24 (c) 32X32

(d) 48X48 (e) 64X64 (f) 96X96

Figure 3.14: Vector fields obtained using different interrogation window sizes.

A slight modification to the median test given by Westerweel in reference [53] was proposed by Westerweel and Scarano [54] to detect spurious vectors with a universal threshold value. Residual (r_0) of the the vector (displacement or velocity) under inspection (u_0) is calculated by taking the difference of the vector and median (u_m) of the 8 vectors surrounding it, $r_0 = |u_0 - u_m|$. r_0 is normalized by median (r_m) of the residual set $\{r_i | i = 1, 2, ..., 8\}$. The threshold of normalised residual ($\hat{r} = \frac{r_0}{r_m}$) which represents the largest 10 or less percentage of the residuals is 2. Threshold value of 2 is chosen here, and thresholds less than 2 gives more stringent detection. Percentage of outliers in flow field with disk rotational speed of 40 Hz is given in Table 3.3.

From the Tab. 3.3 it can be said that the finest spatial resolution that yields vector field of acceptable quality is 24X24. With the digital magnification mentioned in Tab. 3.1 this interrogation size amounts to a spatial resolution of 1.4 mm. Smaller resoltion resulted in Q-factor < 2. For this resoluton the amount of outliers is well within 10% and peak lock values are less than 0.1 with an exception of 0 Hz case. Higher peak locking in the 0 Hz case is due to extremely low pixel displacement values [6, 51]. Very high-amount of outliers in the case of 20 Hz is due to extremely bad seeding at the bottom, and therefore, a more detailed assessment by separating the region of insufficient seeding was carried which showed that the amount of outliers, and Q-factors are much better in the regions of sufficient seeding (App. D). Interrogation window size 24X24 is chosen for the calculation of the velocity fields and the associated uncertainties. The associated uncertainties

Speed	size	16 × 16	24 × 24	32 × 32	48 × 48	64 × 64	96 × 96
0 Hz	% outliers	1.33	2.91	3.21	2.43	1.95	0.84
	Avg. Q-factor	2.41	2.72	2.82	2.89	2.92	2.94
	Peak lock	0.4778	0.5830	0.6381	0.6959	0.7265	0.7566
10 Hz	% outliers	1.44	3.94	4.47	3.70	2.69	1.95
	Avg. Q-factor	2.30	2.64	2.74	2.81	2.83	2.87
	Peak lock	0.0321	0.0399	0.0476	0.0574	0.0695	0.0727
20 Hz	% outliers	1.90	8.56	12.99	16.30	17.99	17.79
	Avg. Q-factor	1.92	2.45	2.65	2.78	2.81	2.79
	Peak lock	0.0212	0.0242	0.0268	0.0509	0.1062	0.1251
30 Hz	% outliers	1.83	5.76	7.88	9.13	10.50	9.80
	Avg. Q-factor	1.95	2.46	2.66	2.78	2.81	2.79
	Peak lock	0.0143	0.0120	0.0130	0.0081	0.0141	0.0144
40 Hz	% outliers	1.89	6.22	10.99	11.06	12.14	15.81
	Avg. Q-factor	1.97	2.44	2.64	2.76	2.80	2.79
	Peak lock	0.0096	0.0096	0.0095	0.0060	0.0081	0.0111

Table 3.3: Interrogation window size wise % of outliers.

and the dynamic range of the PIV set-up is discussed in the following subsection.

3.5.4. UNCERTAINTIES

The uncertainty in PIV is dependent on factors like seeding density, particle image size, displacement, displacement gradient, out-of-plane motion, and background noise [9]. The uncertainty field of the measurement is calculated by the correlation statistics (CS) method proposed by Wieneke and Prevost (2014). A brief description of the method is provided in App. D. The instantaneous uncertainty fields were calculated averaged over time using interrogation window size of 24X24. The field of maximum uncertainty and RMS uncertainy over time were also calculated. The field averages of the mean, RMS, and max field over time is presented in Tab. 3.4.

Speed	Uncertainty	Absolute/(pixels)	Relative/(%)
0 Hz	Mean	0.282	0.558
	RMS	0.336	0.880
	Max	0.830	3.830
10 Hz	Mean	0.284	0.308
	RMS	0.359	0.563
	Max	1.397	8.366
20 Hz	Mean	0.422	0.275
	RMS	0.547	0.578
	Max	2.040	9.538
30 Hz	Mean	0.414	0.215
	RMS	0.543	0.453
	Max	2.516	7.521
40 Hz	Mean	0.471	0.198
	RMS	0.632	0.428
	Max	2.764	7.211

Table 3.4: Uncertainty data.

Tab. 3.4 shows that the mean and RMS absolute uncertainty increases, while mean and RMS relative uncertainty decreases with the increasing disk rotational speed which is due to the increasing magnitude of the detected flow speed [2]. It that the minimum displacement detected by the set-up used in this work is 0.338 pixels (minimum average RMS uncertainty) and the maximum displacement was 22.03 (field average

[2] Relative uncertainty of a measurement is the ratio of absolute uncertainty to measured value. If the rate of increase of absolute uncertainty is lower than the rate of increase of the measurement value, then the relative uncertainty decreases.

of maximum displacement field over time). Using these values a rough estimate of the dynamic range of the set-up amounts to 65. This estimate of dynamic range is done with average values and is an underestimated value. With these parameters a brief discussion on the quality of PIV data is presented the following section.

3.6. CONCLUSION

The previous sections assessed the quality of the PIV data by evaluating the seeding density, signal quality from the particles, signal quality of the cross-correlation (cross-correlation coefficient and Q-factor), amount of spurious vectors (outliers), peak locking, spatial resolution, and uncertainty. It was concluded that the seeding density is satisfactory. Sufficient scattering from the tracer particles yield a signal of SNR > 2.5. Amount of spurious vectors are les than 10 %. The cross-correlation coefficient, Q-factor, peak lock, uncertainty, and dynamic range of the set-up are satisfactory. These results suggest that the seeding technique of evaporating the suspension of siloxane and tracer particles is effective and the 170 nm titania particles scatters sufficient light to perform PIV.

4

PIV Analysis of Compressible Vapour Flows

In Chapter 3 we showed that a low speed flow can be accurately measured using a conventional PIV set-up. The aspects of tracer fidelity and the optical properties of the unconventional fluid did not pose any problem in the measurements of flow field in the NIVA due to the low speed, no jumps in velocity, and almost homogeneous density distribution throughout the flow field. However, in supersonic flows in nozzles these favourable conditions are absent. The compressible phenomena i.e. shock will cause jumps in flow quantities such as velocity and density. The variation of density along the flow direction is substantial even in the absence of shocks due to high molecular complexity of the constituent fluid. These phenomena may pose challenge to PIV measurements in high speed flow which will be investigated in detail in this chapter.

4.1. Supersonic Flow of Dense Vapours

Supersonic flow of any fluid can be generated by a convergent-divergent nozzle (also called de Laval nozzle) by applying appropriate pressure difference. Depending upon the boundary conditions, the variation of flow properties along the nozzle axis depends on the shape of the nozzle (i.e. cross-section area distribution) and the properties of the fluid itself (already discussed briefly in the Sec. 1.2.2). The supersonic nozzle flow of the dense gases is drastically different from that of the air, especially in terms of the gradients of the thermodynamic properties. Another differentiating factor of the dense gases is the low speed of sound, which results in lower flow speeds of dense gases at same Mach no. as that of ideal gases. The Fig. 4.1 shows the nozzles designed to achieve a supersonic flow upto Mach no. 2 of air and MM (X and Y of arbitrary length units). The nozzle for air is designed for an inlet pressure of 2.04 bars, inlet temperature of 300 K based on the design of Scarano and Oudheusden (2003) [47]. The nozzle for MM is designed for inlet pressure of 18.4 bars, and inlet temperature of 525.15 K based on the design of Head et. al. (2016) [31]. Both the designs differs drastically in shape and size. It can be seen that air flow achieves Mach 2 in marginally shorter distance compared to the MM flow. Fig. 4.2 and 4.3 show that the temperature gradients for MM are milder than that of air which is due to larger heat capacity of MM, however the density gradients of MM are far stronger than that of air.

The dense gas flow in nozzle the shown in Fig. 4.1b below is representative of the conditions in ORC turbine stators [55, 56]. To investigate such flows using PIV, it is essential to predict the challenges that can occur while using PIV on dense gas nozzle flows using the conventional set-up used for ideal gas flows. One of such problems could occur due to the dependence of refractive index on the density (see Sec. 2.1.2) . The strong density gradients will cause strong gradients of refractive index which can pose challenge in capturing good quality images. Due to the supersonic nature of the flow, it is most likely that shocks will be encountered in ORC turbines. Shocks as already discussed in Sec. 2.2.1 cannot be resolved, however the tracer particles should still be chosen such that they recover from the sharp velocity jump as soon as possible for accurate field measurements. Another factor that differentiate the dense gas nozzles from the ideal gas nozzles is curvature. The concave curvature after the throat as seen in the Fig. 4.1b is larger than that in the Fig. 4.1a. The heavier tracer particles cannot follow strong curvatures in streamlines and should be investigated. The effect of density gradients, shock waves, and curvatures in the flow on the application of PIV is studied here.

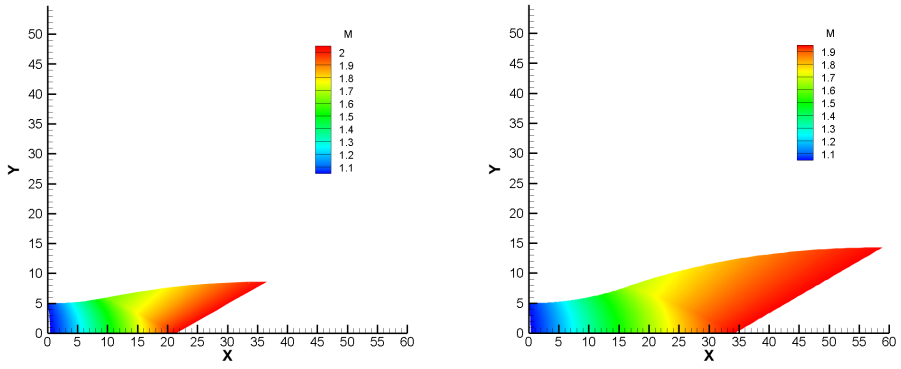

(a) Air (b) MM

Figure 4.1: Nozzle shape with Mach no. distribution. Throat radius of curvature is 50 units.

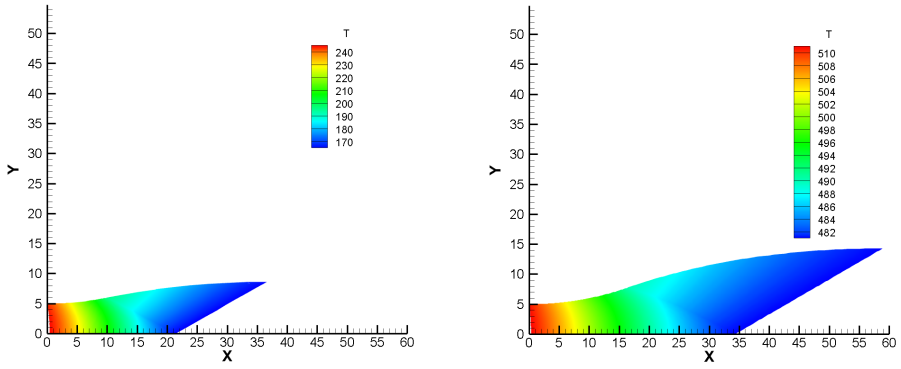

(a) Air (b) MM

Figure 4.2: Nozzle shape with temperature distribution.

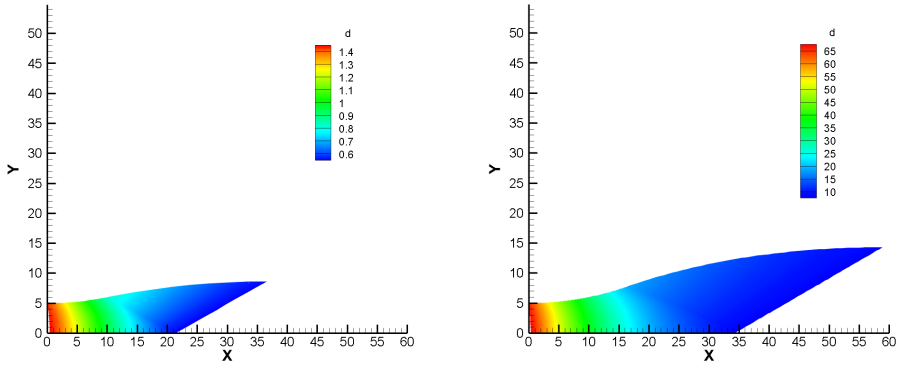

(a) Air (b) MM

Figure 4.3: Nozzle shape with density distribution.

4.2. VARIATION OF REFRACTIVE INDEX

It can be seen in Fig. 4.3 that the density magnitude and its variation along the nozzle path is significantly larger in case of MM than in air. This can pose challenges to the imaging set-up of the conventional PIV used for investigating the flow as a result of inhomogeneous refraction. The refractive index distribution across the nozzle for air and MM can be seen in the Fig. 4.4.

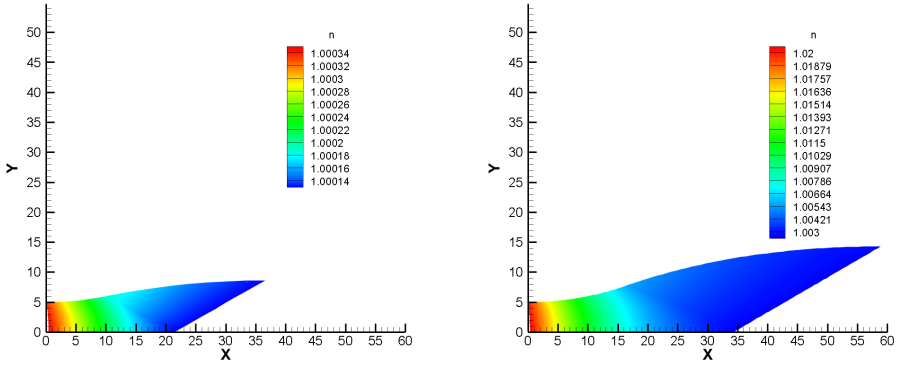

(a) Air (b) MM

Figure 4.4: Nozzle shape with refractive index distribution.

Due to the large difference between refractive index at the throat and at the exit location where flow speed is Mach 2, there could exist a large difference in the apparent depth (due to inhomogeneous normal shift) of the particles image at these locations, which can result in poorly focused images. Possibility of severe particle image blur (due to inhomogeneous lateral shift) due to inhomogeneous refractive index field can cause problems in PIV processing [57]. The challenges in capturing good quality images due to the inhomogeneous refractions is further elaborated in the following subsections. Since the deflections due to refraction from glass window is uniform along the nozzle length, it is neglected from the error estimation.

4.2.1. INHOMOGENEOUS NORMAL SHIFT

The phenomenon of refraction causes the light to change its direction of propagation at the interface between two media of different refractive index, due to which the apparent position of the object is different from the original position. If an object is in a medium of higher refractive index (denser medium) and is observed from a medium of lower refractive index then the object appears closer along the normal direction. This normal shift is represented in the ray diagram shown in the Fig. 4.5, where the n_1 is the refractive index of the media from which the object is observed and n_2 is the refractive index of the media in which the object is located.

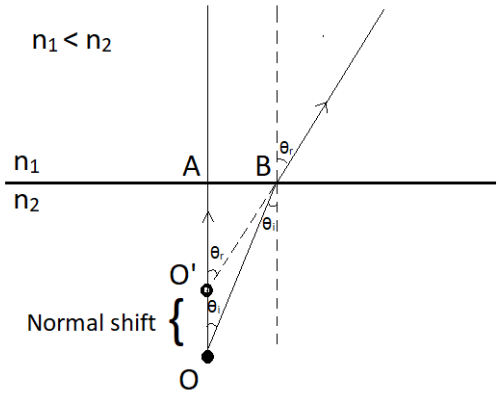

Figure 4.5: Normal shift due to refraction.

The normal shift OO' can be estimated using the Snell's law for refraction which is given by the Eqn. 4.1

and routine trigonometric relations. From the right angled triangles ABO and ABO', the length AO and AO' is given by the Eqns. 4.2 and 4.3 respectively.

$$n_1 \sin\theta_r = n_2 \sin\theta_i \tag{4.1}$$

$$\mathrm{AO} = \frac{\mathrm{AB}}{\tan\theta_i} \tag{4.2}$$

$$\therefore \mathrm{AO'} = \frac{\mathrm{AB}}{\tan\theta_r} = \mathrm{AO}\frac{\tan\theta_i}{\tan\theta_r} \tag{4.3}$$

Now using Eqns. 4.2 and 4.3, OO' can be expressed by the following equations,

$$\therefore \mathrm{OO'} = \mathrm{AO} - \mathrm{AO'} = \mathrm{AO}\left(1 - \frac{\tan\theta_i}{\tan\theta_r}\right) \tag{4.4}$$

Now for small θ_i and θ_r the results $\tan\theta_i \approx \sin\theta_i$ and $\tan\theta_r \approx \sin\theta_r$ holds, and now the OO' can be expressed as given by the following equation,

$$\mathrm{OO'} = \mathrm{AO}\left(1 - \frac{n_1}{n_2}\right) \tag{4.5}$$

In a PIV campaign the n_1 is the refractive index of the air at STP (the medium in which camera is located) and the n_2 is the refractive index of the fluid (Air or MM) inside the nozzle between the measurement plane (laser sheet) and nozzle boundary. The refractive index of air at the throat ($n_{2,X=0}$ = 1.000345) is only 0.022% larger than that at the location of desired expansion ($n_{2,X=21}$ = 1.000123). The refractive index of MM at the throat ($n_{2,X=0}$ = 1.0203) is almost 1.75% larger than that at the location of desired expansion ($n_{2,X=33}$ = 1.00275). Consider a small section of nozzle shown in the Fig. 4.6a, which shows laser sheet and camera's focal depth from top of the nozzle. The normal shift depends on the distance between measurement plane and the nozzle wall which is indicated by length W in the Fig. 4.6a. The Fig. 4.6b shows the profile of refractive index along the nozzle axis for the MM flow. Since the refractive index of MM flow is larger than the ambient air, it can be said that the normal shift occurs in n the direction towards the camera. Also, from the Eqn. 4.5 and the refractive index profile it can be judge that the normal shift will be non-uniform along the x-direction. If the profile of the normal shift is such that apparent location is out of the focal depth then the particle image can be highly defocussed.

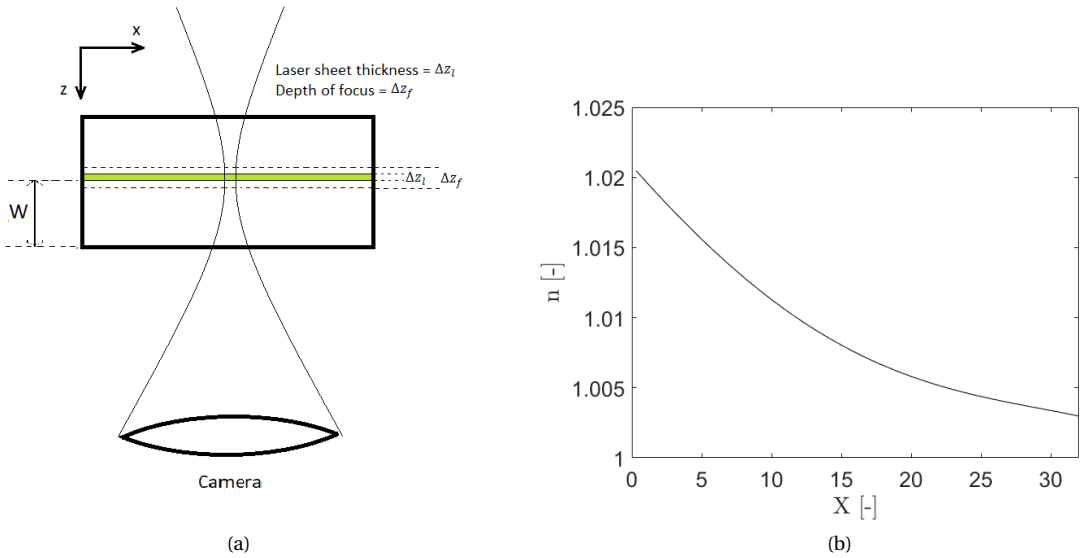

(a) (b)

Figure 4.6: Schematic of focal depth and laser sheet thickness along with refractive index profile at nozzle axis for MM.

4.2.2. INHOMOGENEOUS LATERAL SHIFT

Apart from the optical issue in normal direction discussed in the Sec. 4.2.1, even more complicated optical effects can occur in the lateral direction due to large density gradients. Such issues in air is discussed by Elsinga et. al. (2005) where the authors study the position error (Fig. 4.7a) and velocity error (Fig. 4.7b) that could occur in PIV measruements due to aero-optical distortions that occurs as a consiquence of inhomogeneous denisty field [57].

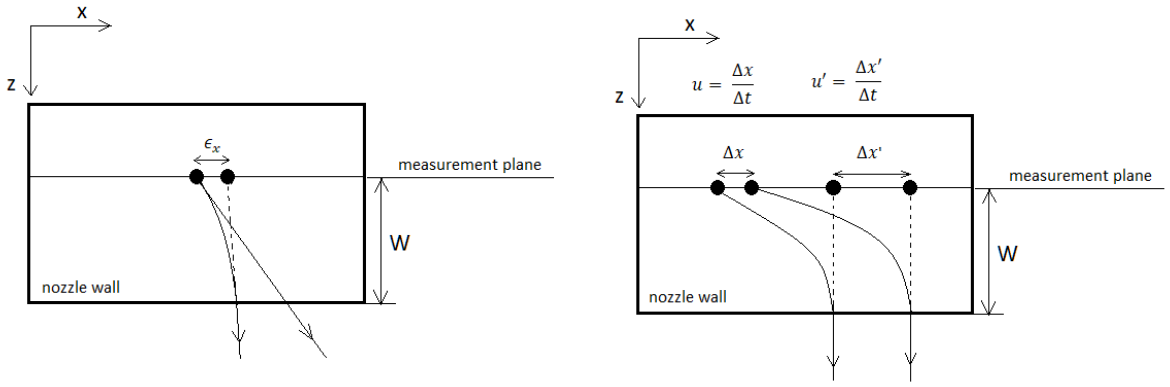

(a) Position error

(b) Velocity error

Figure 4.7: Errors due to presence of on-zero refractive index gradient.

With an assumption that the refractive index is constant along the z-direction the Eqn. 4.6 gives the position error ($\vec{\epsilon}$) which is the difference between the actual position of the particle and perceived position of the particle due to presence of a non-zero gradient of refractive index [57]. The Fig. 4.7a depicts the position error only in x-direction, while the Eqn. 4.6 gives the 2D error. The refractive index gradient shown in the Fig. 4.4b is significantly more pronounced in the x-direction than in y-direction, therefore a preliminary estimation of refractive index gradients only in the x-direction is presented to judge the magnitude of optical challenges that could be encountered in supersonic MM flow.

$$\vec{\epsilon} = -\frac{1}{2} W^2 \nabla n \tag{4.6}$$

Fig. 4.6b shows the refractive index curve along X at the nozzle axis. A fourth order polynomial curve was fitted to the refractive index distribution and was differentiated to determine the refractive index derivative at the nozzle axis which is shown in the Fig. 4.8a. The relation of the velocity error ($\vec{\epsilon}_v$) to the particle velocity ($\vec{u}_p$) and the position error is given by Eqn. 4.7. On substituting Eqn. 4.6 in Eqn. 4.7 one obtains Eqn. 4.8 which gives the relation between the velocity error, particle velocity, and the refractive index derivatives [57].

$$\vec{\epsilon}_v = (\nabla \vec{\epsilon}) \cdot \vec{u}_p - (\nabla \vec{u}_p) \cdot \vec{\epsilon} \tag{4.7}$$

$$\vec{\epsilon}_v = -\frac{1}{2} W^2 (\nabla^2 n \cdot \vec{u}_p - \nabla \vec{u}_p \cdot \nabla n) \tag{4.8}$$

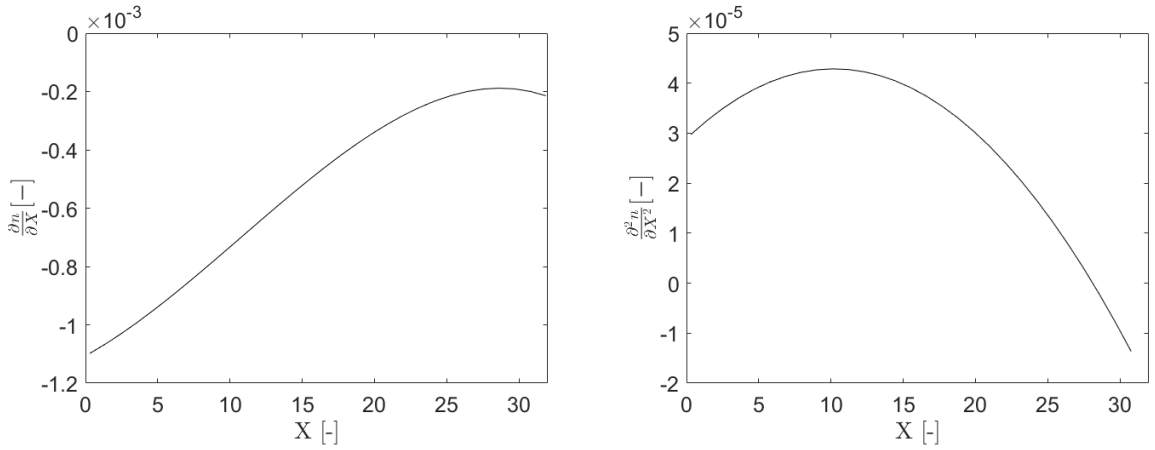

(a) Refractive index derivative

(b) Refractive index second derivative

Figure 4.8: Refractive index derivative and refractive index second derivative profile along the nozzle axis for MM.

4.3. TRACER PARTICLE FIDELITY

Both the sudden change in flow speed and sudden change in flow direction can cause momentary discrepancies between actual flow velocity and flow velocity as measured by the tracer particle. As already briefly discussed in the Sec. 2.2.1, the faithfulness of the tracer particles is assessed by the particle response time τ_p or the particle Stoke's number St_p w.r.t. a flow feature. Another quantity called relaxation length (ξ_p) can also be used as an alternative to τ_p, which is the distance travelled by the tracer particle in time τ_p. The time scales of the flow features under investigation should be known beforehand and the choice of the tracer particle should be made accordingly. If the investigation aims to analyse all the flow features, then the tracer particle should be chosen such that the St_p is less than 0.1 w.r.t. the smallest time scale, for example the Kolmogorov time scale in turbulent flows. The following sections will study the effect of sudden change due to shock wave and continuous change due to curvature in flow conditions on the velocity of the tracer particle.

4.3.1. STEP CHANGE IN FLUID FLOW

The shock wave thickness is approximated to be four times the mean free path length of molecule that constitutes the medium, and it turns out to be of the order of 10^{-7} m for air [48]. The estimation of shock wave thickness involves an assumption that the molecule is a rigid sphere and no intermolecular forces prevail in the gas phase. Since, these assumptions cannot be considered valid for MM one cannot accurately estimate the thickness of the shock wave. However, an assumption is made that the thickness of the shock wave is small enough to consider the jump in properties across the shock wave as instantaneous. And due to such small thickness of shock waves they are unresolvable by techniques that requires flow tracking through tracer particles such as PIV.

The shock waves have been used to experimentally determine the time response of the tracer particles. One such example is the study by Ragni et. al. (2011) where the author verifies the numerical assessments of particle response time of DEHS droplets, titania, and silica were verified by using PIV on a shock wave at Mach 2.0 air flow [58]. A non-dimensional interrogation window size (WS) and a non-dimensional pulse separation time (Δt_p) are introduced by authors as defined by the Eqn. 4.9 and 4.10, respectively. SR and TR are referred as spatial ratio and temporal ratio which are nothing but the window size and pulse separation time normalized by the relaxation length and response time of tracer particles. Numerical estimation of the relaxation time and response time of tracer particles used in the NIVA is used to recommend achievable spatial and temporal resolution using the same tracers in PIV application on high speed MM flow.

$$SR = \frac{WS}{\xi_p} \tag{4.9}$$

$$TR = \frac{\Delta t_p}{\tau_p} \tag{4.10}$$

When a supersonic flow shown in the Fig. 4.1 encounters an object in the way, an Oblique Shock Wave (OSW) is generated that causes a sudden change in the flow properties. A simplest case is shown in the Fig. 4.9 where a wedge with the inclination angle θ causes an OSW with an inclination angle of β.

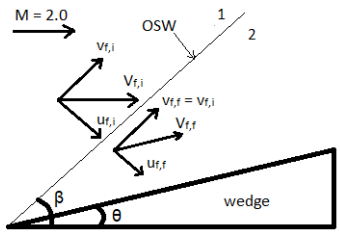

Figure 4.9: Oblique shock wave and velocity jump.

The jump conditions of the OSW is simulated for $\theta = 11°$ using an Euler shock wave generator E.1. These jump conditions are then used to plot the tracer particle velocity w.r.t. time and distance to study it's relaxation distance and the response time. It was concluded by Ragni et. al. that a pulse separation of less than τ_p ($TR < 1$) and interrogation window size of less than ξ_p ($SR < 1$) is required for a reliable measurement the particle response using PIV. However, for an accurate measurement of the flow properties the pulse separation and interrogation window size should be such that $TR > 1$ and $SR > 1$. The Fig. 4.10 shows the tracer velocity vs distance and tracer velocity vs relaxation time of titania particles in supersonic MM flow of density shown in the Fig. 4.3b.

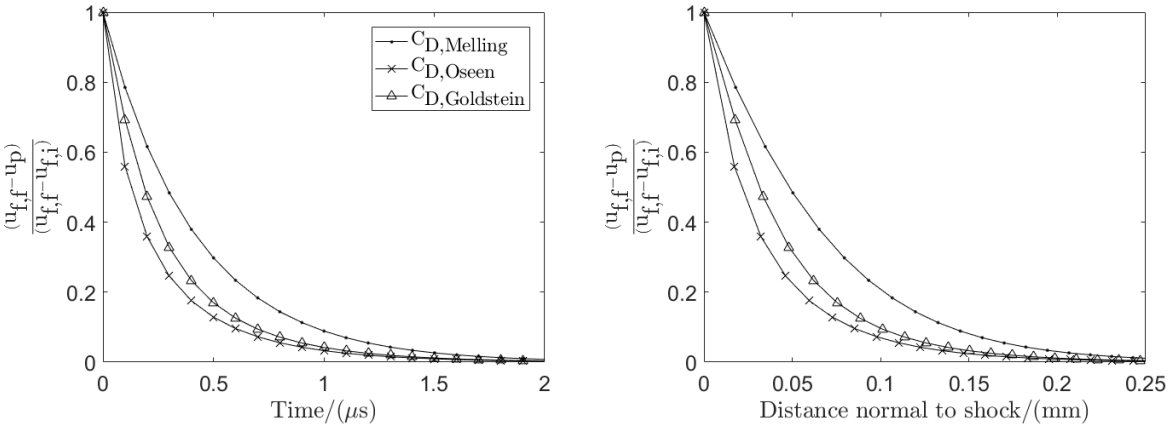

(a) Temporal response

(b) Spatial response

Figure 4.10: Response characteristics of 170 nm titania particles in supersonic MM flow calculated numerically.

The response characteristics were calculated by solving the Eqn. 2.20 using the three different drag formulation. The relaxation distance and relaxation time calculated for the three different drag formulations are shown in the Tab. 4.1.

C_D	ξ_p/μm	τ_p/μs
Melling	66.1	0.41
Oseen	30.3	0.27
Goldstein	43.5	0.19

Table 4.1: Relaxation distance and time for 170 nm titania particles in supersonic MM flow.

The relaxation parameters determined using Melling's drag formulation are greater than the same determined using Oseen's and Goldstein's formulation. In reality, the particle relaxation distance and time are

always greater or equal to the numerically determined values [58]. Therefore, the estimation of relaxation distance and time using Melling's formulation can be deemed reliable and will be used from here onwards. It can be concluded that with 170 nm titania particles the minimum achievable spatial resolution is 66.1 μm and minimum achievable temporal resolution is 0.41 μs.

RESPONSE TO SUDDEN FLOW TURNING

A good tracer particle is also expected to respond to sudden turning the flow. In real life situations the sudden deflection can be modelled as a finite angle deflection over a small distance. The exaggerated representation of the streamline of fluid passing over the corner at which the deflection takes place can be seen in the Fig. 4.11. The small length Δs is synonymous to the shock thicknes, which a jump in direction of the velocity vector. The change in velocity of fluid undergoing a turn can be construed as changes in its velocity components decomposed parallel to and normal to its initial velocity vector as shown in the Fig. 4.11. The curved element can be approximated as a circular arc that subtends and angle $\Delta\psi$. The radius of curvature of the corner $R_c = \frac{\Delta s}{\Delta\psi} \rightarrow 0$. The assumption in the Fig. 4.11 is that the particle velocity is equal to the fluid velocity before it encounters the curvature. Also over the small Δs the the magnitude of the fluid velocity is assumed constant i.e. $\vec{V}_{f,1} = \vec{V}_{f,2}$.

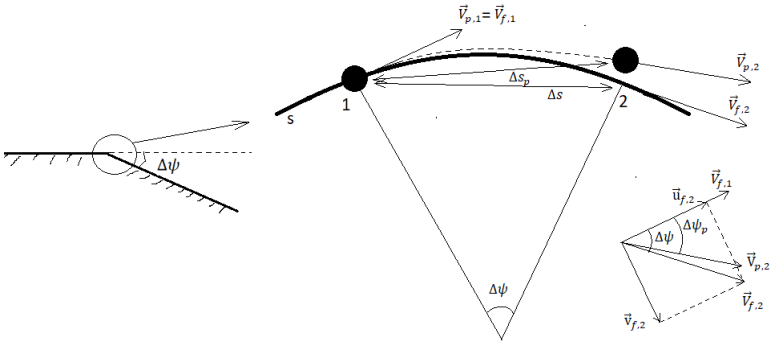

Figure 4.11: Response of tracer particle to sudden flow turning.

Using the same framework as discussed in the Sec. 2.2.1 and using the Melling's drag formulation, one can calculate the variation of the two components of the particle velocity with time. The MM flow conditions that prevails at the section where M = 2.0 is taken for this calculation. Using the two component of the velocity one can determine the direction of the velocity vector at any instant. Similar to particle response time in case of velocity jump, the response time in case of direction jump can be defines as the time taken by particle to achieve 63 % of the deflection.

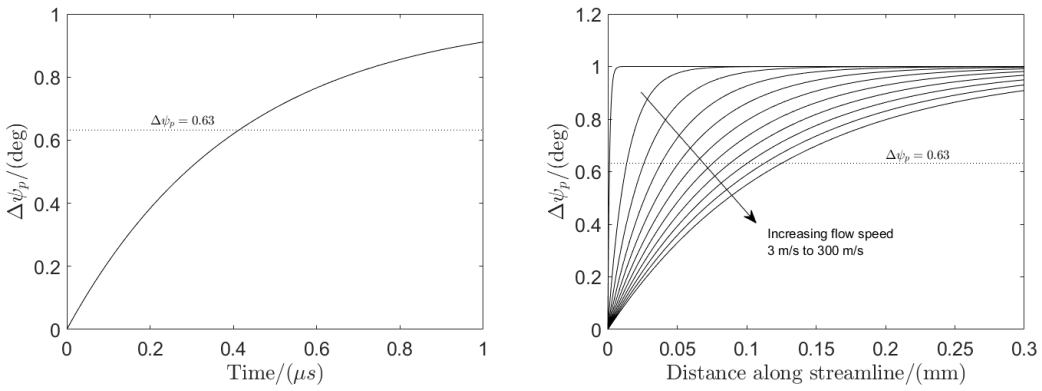

(a) Particle velocity angle vs time for $\Delta\psi = 1°$

(b) Particle velocity angle vs distance for $\Delta\psi = 1°$

Figure 4.12: Flow turning response of the 170 nm titania particles for in a dense MM flow.

Taking an arbitrary value of $\Delta\psi = 1°$ the angle of particle velocity ($\Delta\psi_p$) was plotted against time as shown in the Fig. 4.12a for flow velocities varying from 3 m/s to 300 m/s. It can be seen that the particle response time ($\tau_p = 0.41\mu$s) to the deflection is constant regardless of the velocity of the flow and is same as observed across the oblique shock in previous section. However, the distance travelled by the particle to in the response time is naturally dependent on the flow velocity as seen in the Fig. 4.12b. The particle relaxation distance for varying flow velocity and varying deflection angle (1° to 10°) was plotted and is shown in the Fig. 4.13. It is reasonable to say that the tracer particles can follow smoother curvature (finite radius of curvature) with acceptable accuracy.

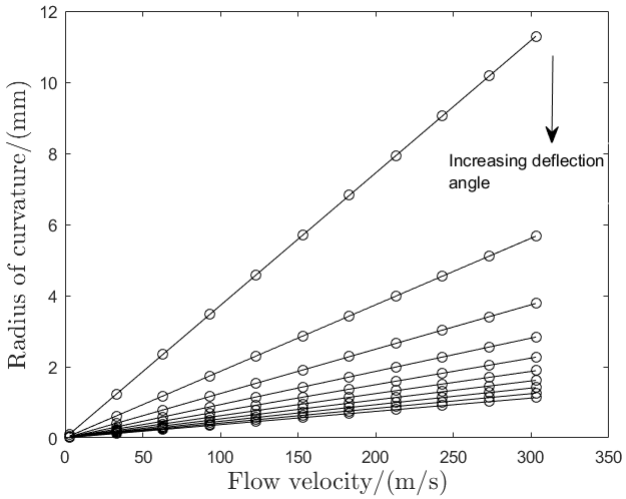

Figure 4.13: Radius of curvature of particle trajectory in dense MM flow for deflection angle varying from 1^o to 10^o.

4.4. SEEDING STRATEGIES FOR VAPOUR TUNNELS

Vapour tunnels are counterparts of wind tunnels that generates vapour flows. Vapour tunnels used to simulate flow conditions of ORC expanders operate at pressures that are very high when compared to the wind tunnels. Therefore, the conventional seeding techniques (see Sec. 2.2.3) to seed solid tracer particles in gaseous flows cannot be used, as it may risk contamination of the vapour and may cause catastrophic failure at high temperatures.

Only viable option of seeding vapour tunnels is to atomize the suspension of the liquid working fluid and tracer particles. Gallarini (2015) designed a seeding system where a hydraulic nozzle atomizes the suspension and sprays it into the main flow. The suspension droplets vapourizes and releases the tracer particles [5]. However, long term use of liquid suspension may lead to coagulation of the tracer particles and may lead to blockages of resulting in failure of the seeding system. Lower surface tension of vapour phase could reduced the risk of coagulation and consequently blockages, and hence, here an alternative seeding strategy is proposed where the suspension is first evaporated and then introduced in the main flow. The conceptual schematic of the seeding system is shown in Fig. 4.14 and its working principle is described below. Operating principle of the proposed design of the seeding system for the vapour tunnels is as follows,

1. Keeping valves 1, 2, 3, and 4 closed vacuumize the collector using the vacuum pump. Switch-off valve V after vacuumizing.

2. Reservoir stores the suspension of siloxane and tracer particles. The suspension is stirred by mixer and evaporated by heating. Open valve 1 to fill the corrector with siloxane vapours with tracer particles. A series of impactor plates can be used to filter out large tracer particles.

3. Once sufficient amount of vapour is collected switch off the valve 1 and switch on the valve 2 to pressurize the collector using nitrogen.

4. Once sufficient pressure is built to push out the vapour + tracer switch on the valve 3 to seed the main flow.

5. After all the tracer particles in collector are sent out, switch off valve 3 and release the nitrogen pressure by switching on the valve 4.

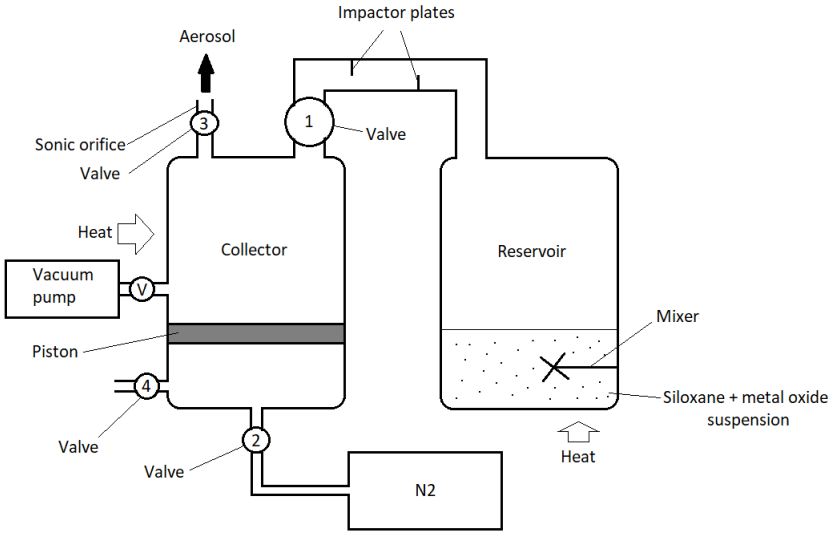

Figure 4.14: Conceptual design of seeding system for vapour tunnels.

5

RESULTS

5.1. PIV RESULTS FROM NIVA

Results of the PIV measurements done on the flow in NIVA will be briefly discussed in this section. An argument in favour of using POD based background removal as image preprocessing technique is presented. The mean velocity fields of flow induced by rotating disk at different rotational frequency and the corresponding uncertainty field is presented. The mean velocity fields were calculated from the instantaneous velocity fields that were obtained by same image processing algorithm used in chapter-3 except this time the final iteration was done using circular interrogation windows (DaVis settings shown in Fig. D.2). Before taking the time average, the instantaneous fields were post-processed to remove outliers using universal outlier detection and interpolation (post-processing settings can be seen in Fig. D.3).

5.1.1. MEAN VELOCITY FIELDS

Subtraction of TSM or POD based background removal were used to correct for influence of reflections from the disk on the mean velocity fields. The results after using the above mentioned techniques separately can be seen in the Fig. 5.1. The velocity field obtained after POD based background removal shows significantly less influence of reflections compared to the subtraction of TSM. Therefore, in conjunction with the evidence shown in the Sec. 3.4.1, the POD based background removal is significantly better image pre-processing technique compared to the TSM subtraction. It is also suggested that the POD based background removal should be used as pre-processing technique for a correcting bad reflections.

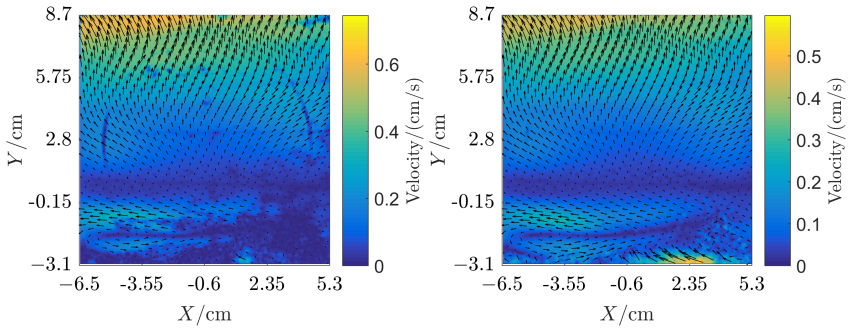

(a) TSM subtraction

(b) POD based background removal

Figure 5.1: Comparing effects of image pre-processing on vector fields.

STATIONARY DISK

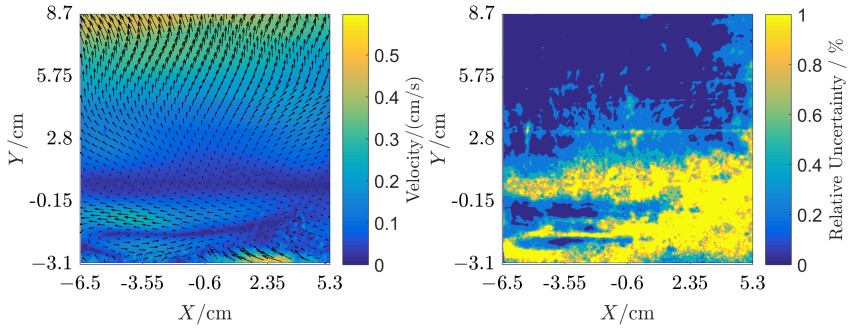

(a) Average velocity (b) Relative Uncertainty

Figure 5.2: Disk rotating at a frequency of 0Hz.

Unacceptable peak locking was observed in instantaneous fields in case of stationary disk due to very small pixel displacement. To obtain a better pixel displacement, a series of images was created from the sample of 1000 images by skipping 20 images. This effectively changes the pulse separation time from 3.33 ms to 66.7 ms and consequently higher pixel displacement. The peak lock was significantly less than 0.1 after this modification. The new sample was used to calculate the instantaneous velocity fields and associated uncertainty fields. The time averaged mean velocity fields and mean relative uncertainty field are shown in Fig. 5.2 which suggest presence of non-zero velocity despite of no disk rotation. In absence of disk rotation the only causes of motion of the fluid is the temperature difference between the floor and the ceiling of the NIVA which results in a small convective flow.

ROTATING DISK

For the disk rotational frequency of 40 Hz the mean velocity field (Fig. 5.3a) shows significant correlation with the motion of the disk. The relative uncertainty of the shown velocity field is well within 1% and can be seen in the Fig. 5.3b. The mean velocity field for disk rotational frequency of 30 Hz shows rotation but it is weaker and less prominent when compared to that of the 40 Hz case. The relative uncertainty is well within 1% except at few locations around (-5.5 cm, 2.8 cm) where the disk reflections were dominant. The mean velocity field for disk rotational frequency of 20 Hz can be seen in the Fig. 5.5a and it can be observed that the rotating motion of fluid is absent unlike the 30 Hz and 40 Hz case. One can observe the presence of a region of zero velocity along the line $Y \approx 2.8$ cm in the measurement plane. The relative uncertainty as can be seen in the Fig. 5.5b is well within 1% except at few locations. The mean velocity field for disk rotational frequency of 10 Hz (Fig. 5.6a) is very similar to that of 20 Hz case except for the magnitude which is expected to be less due to slower disk rotation. One can notice the zero velocity region along The relative uncertainty along $Y \approx 1.5$ cm is larger than 1 % which was also observed in previous case at around same location.

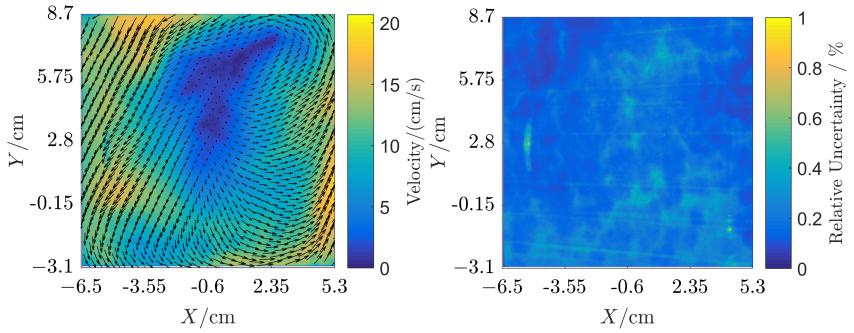

(a) Average velocity (b) Relative uncertainty

Figure 5.3: Disk rotating at a frequency of 40Hz.

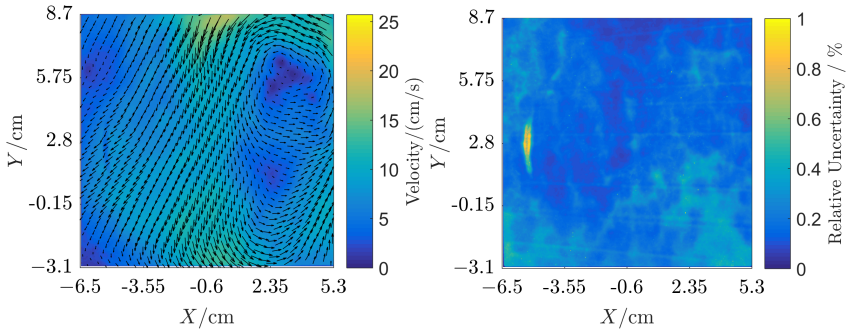

(a) Average velocity (b) Relative uncertainty

Figure 5.4: Disk rotating at a frequency of 30Hz.

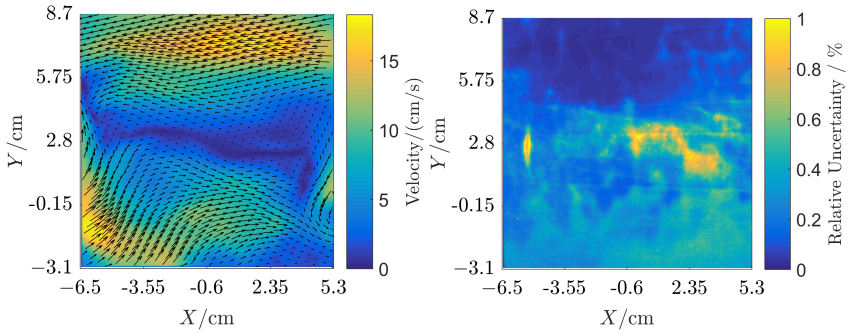

(a) Average velocity (b) Relative uncertainty

Figure 5.5: Disk rotating at a frequency of 20Hz.

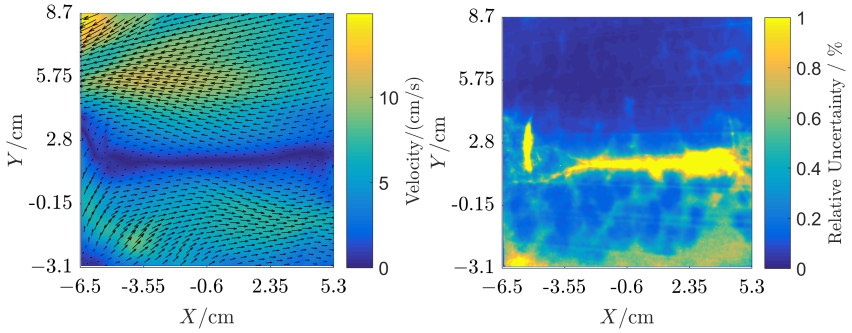

(a) Average velocity (b) Relative uncertainty

Figure 5.6: Disk rotating at a frequency of 10Hz.

Duration of the experiments is 3.33 seconds and the instantaneous velocity fields between $t = 0s$ and $t = 3.33s$ at 5 regular intervals are presented in App. C. On comparing the figures in App. C and mean velocity fields it is clear that the flow fields in case of 40 Hz and 30 Hz disk rotation is fully turbulent, while, the same in case of 20 Hz and 10 Hz disk rotation is near transition.

5.1.2. ABSOLUTE UNCERTAINTIES

The magnitude of absolute uncertainty as seen in Fig. 5.7 increases with the increasing magnitude of the disk rotation which was anticipated. However, the decrease in relative uncertainty with increase in disk rotation suggests that the absolute uncertainty does not linearly increase with the disk rotation speed. The absolute uncertainty magnitude is lower than that of the convective velocity shown in Fig. 5.2a. If the absolute uncertainty is the minimum resolvable velocity then from Fig. 5.7 and mean velocity suggests that the dynamic

range of the set-up is much higher than the rough estimate of 65 made in Sec. 3.5.4.

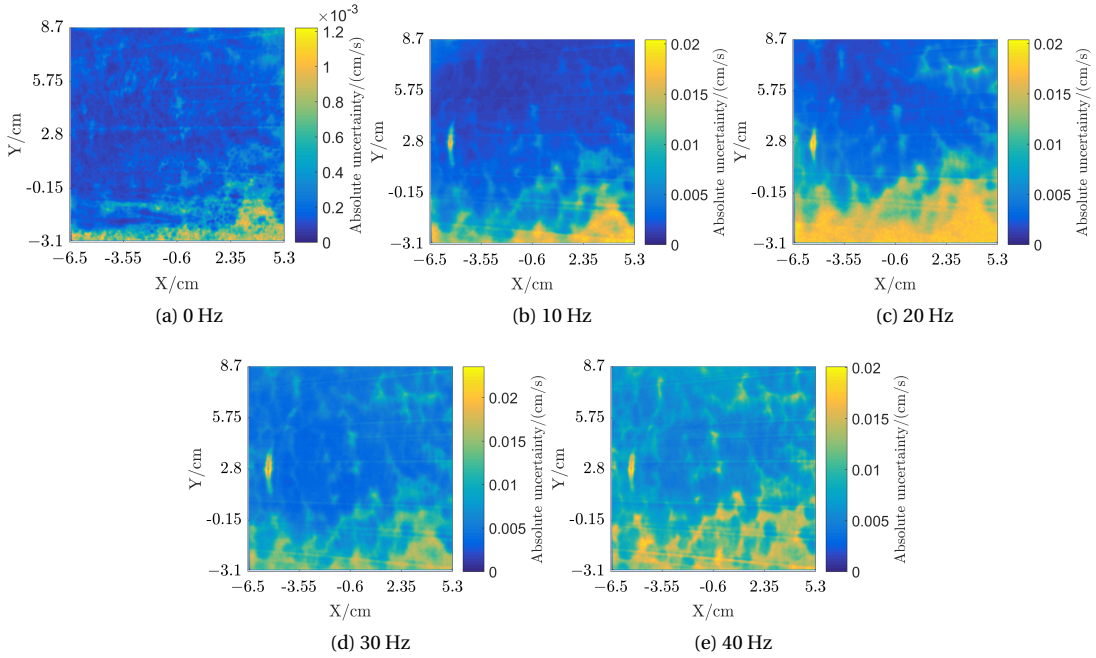

(a) 0 Hz (b) 10 Hz (c) 20 Hz

(d) 30 Hz (e) 40 Hz

Figure 5.7: Absolute uncertainty field in $[cm/s]$ for different disk rotational frequencies.

5.2. FEASIBILITY IN COMPRESSIBLE FLOWS

The assessment of the feasibility of the particle image velocimetry in compressible flows was done in the Chapter 4 in context of supersonic flow of MM vapours. The potential challenges to PIV application in supersonic vapour flows that were discussed are aero-optical distortions of tracer particle images and tracer particle fidelity to the flow.

5.2.1. OPTICAL CHALLENGES

The potential optical challenges to PIV application discussed in the Sec.4.2 were a consequence of significantly large refractive index gradients. The refraction that occurs in a medium of strong refractive index gradients causes the difference in the actual location and perceived location in normal and lateral direction.

NORMAL DIRECTION

The Fig. 5.8 shows the normalized normal shift profile in supersonic MM flow along the nozzle axis. The normal shift is normalized w.r.t. the distance between the measurement plane and the nozzle wall. Hence the magnitude of the normal shift depends on the width of the nozzle. The shape of the normal shift profile also represents the shape of the perceived measurement plane and it is important that the apparent measurement profile is well accommodated within the depth of focus. Now, the depth of focus is a function of the wavelength of laser (λ), f-number ($f_\#$) and the magnification factor (M_f) (Eqn. 5.1). Therefore, a non-linear shape of the perceived measurement plane puts a constraint on the f-number to be used for a given magnification or vice-versa. For example, to properly focus a field of view shown in the Fig. 5.8, the condition shown in the Eqn. 5.2 needs to be fulfilled.

$$\Delta z_f = 4.88\lambda f_\#^2 \left(\frac{M_f + 1}{M_f}\right)^2 \tag{5.1}$$

$$\Delta z_f \geq \text{Norma shift}_{X=0} - \text{Norma shift}_{X=33} \tag{5.2}$$

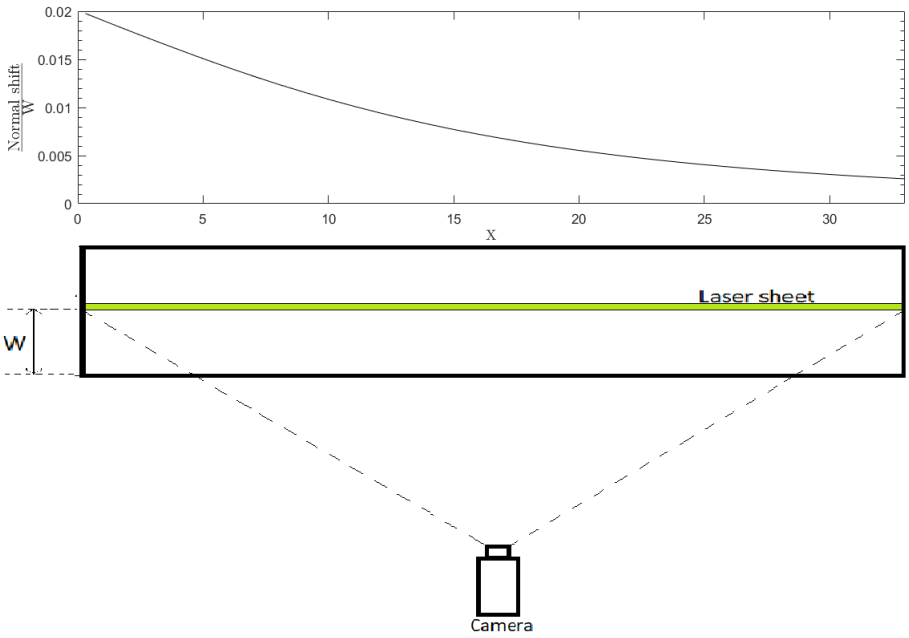

Figure 5.8: Normal shift due to refraction.

LATERAL DIRECTION

The effect of optical-distortions in lateral directions where discussed in the Sec. 4.2.2 and the relationships between the refractive index gradients and expected error in velocity measurements were established. The relationships given in the Eqns. 4.6 and 4.8 are for the 2D position and velocity errors that could occur due

to refractive index gradients. However, the refractive index gradient in X-direction is significantly more pronounced than that in Y-direction therefore, the errors are only calculated for the X-direction along the nozzle axis. Consider the X-component of the Eqns. 4.6 and 4.8 given by Eqns. 5.3 and 5.4 respectively.

$$\epsilon_X = -\frac{1}{2} W^2 \frac{\partial n}{\partial X} \tag{5.3}$$

$$\epsilon_{v,X} = -\frac{1}{2} W^2 \left(\frac{\partial^2 n}{\partial X^2} \cdot u_{p,x} - \frac{\partial u_{p,x}}{\partial X} \cdot \frac{\partial n}{\partial X} \right) \tag{5.4}$$

The X-axis in the Fig. 4.8 is of the arbitrary unit , however it is better to take an example of realistic unit to better understand the importance of the velocity gradients, and estimate the errors. Therefore, considering the X in mm units the refractive index derivative and second derivative now is as shown in the Figs. 5.9.

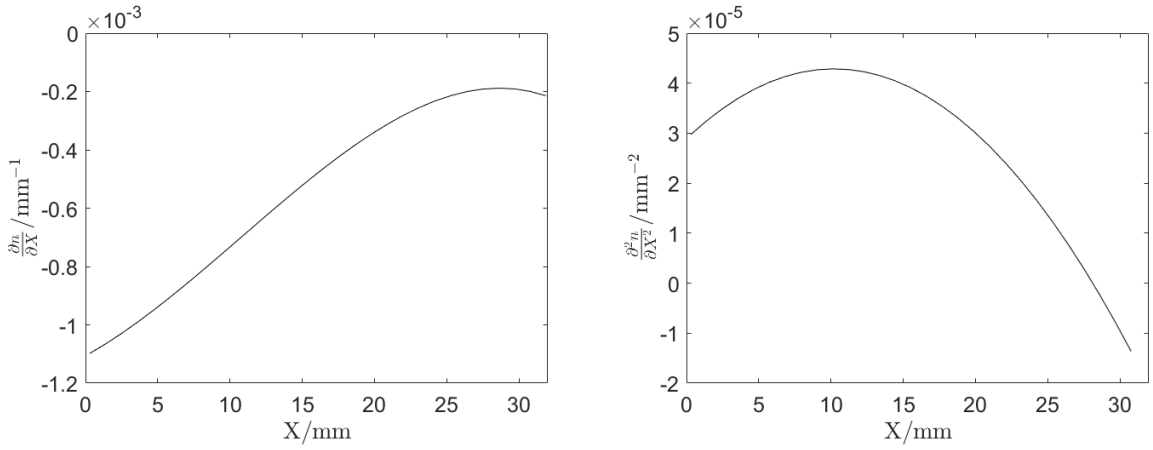

(a) Refractive index derivative

(b) Refractive index second derivative

Figure 5.9: First and second derivative of the refractive index along the nozzle axis for MM.

The other two variables required to compute the position error and the velocity error in X-direction is the velocity of particle and its gradient in X-direction, which can be seen in the Fig. 5.10a and 5.10b respectively. Using the required variables the quantities $\frac{\epsilon_x}{W^2}$ and $\frac{\epsilon_{v,x}}{W^2}$ are evaluated along the nozzle axis, and the results are shown in the Fig. 5.11.

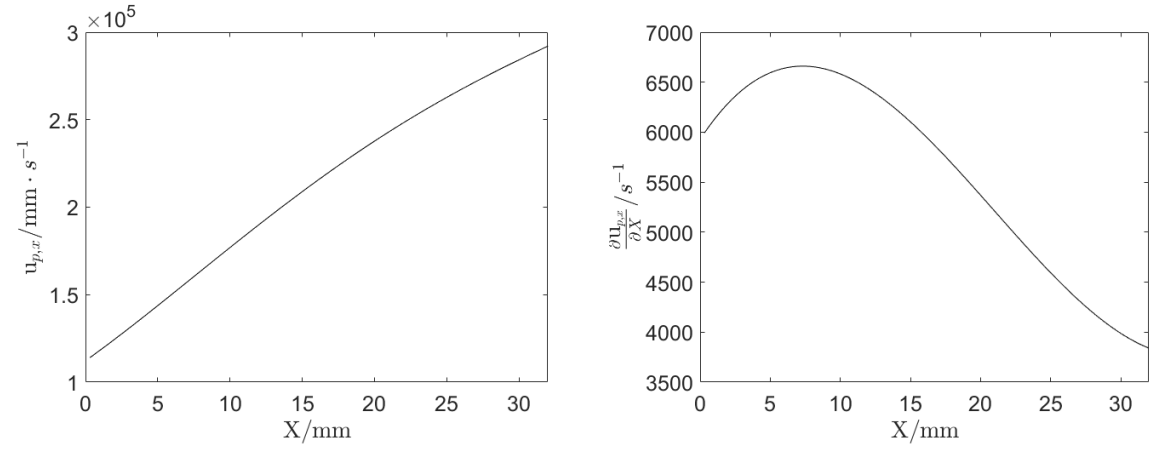

(a) X velocity

(b) X velocity derivative

Figure 5.10: X-component of velocity and its derivative profile along the nozzle axis for MM.

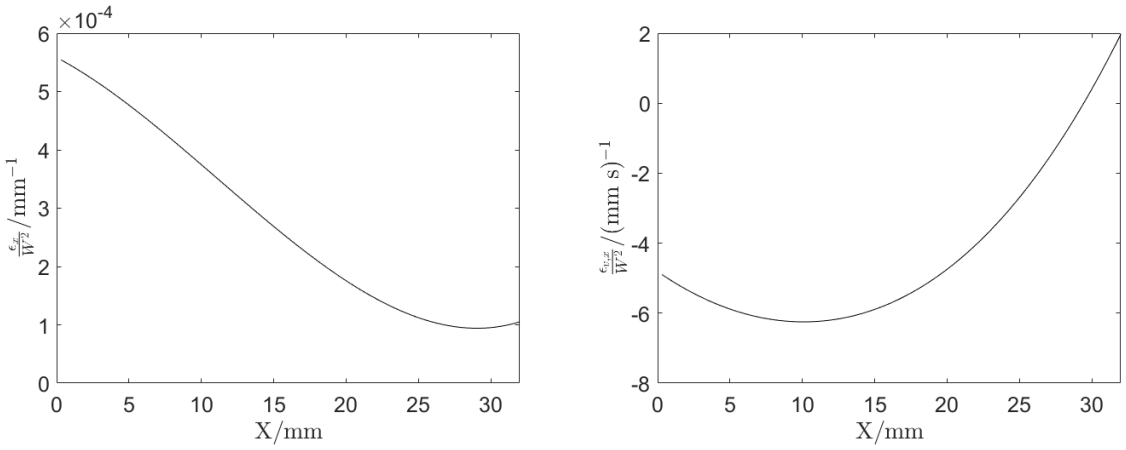

(a) (b)

Figure 5.11: Position and velocity errors divided by W^2.

The expansion of MM flow in the above examples occurs in the thermodynamic region shown in Fig. 5.12. The compressibility factor of MM during the expansion can be seen in Fig. 5.12a and the compressiblity factor less than 0.75 suggests significant non-ideal behaviour. It can be seen from Fig. 5.12b that if the exapansion of MM takes place closer to the vapour-liquid saturation curve then the resulting refractive index gradients are higher and can cause serious errors in velocity due to optical distortion.

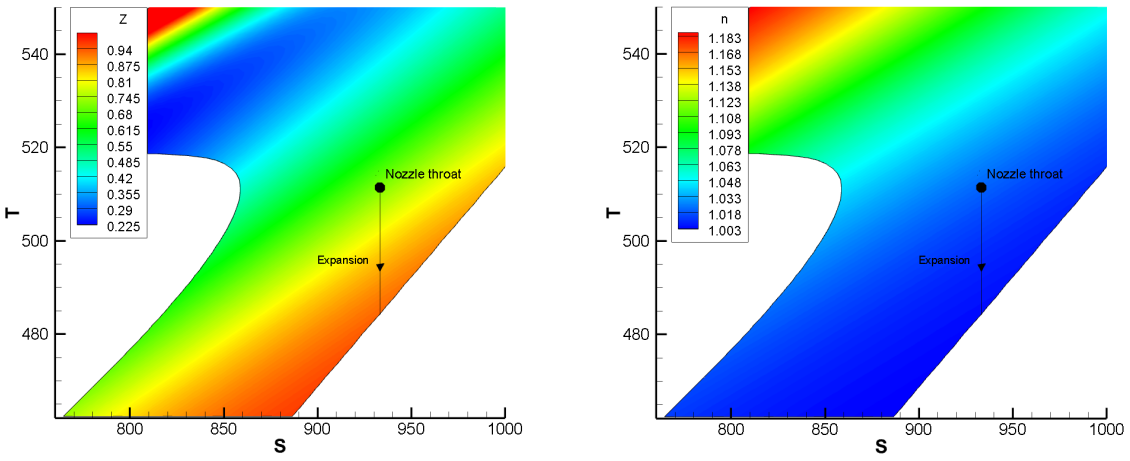

(a) Compressibility factor (b) Refractive index

Figure 5.12: Expansion process of MM flow over T-S plot.

It should be noted that the parameter shown in Fig. 5.11b is the ratio of velocity error and the square of distance between measurement plane and nozzle wall. Therefore, it can be said that the velocity errors will grow if scale of nozzle geometry is increased and the growth is quadratic. For example, doubling the scale of nozzle geometry will result in 4 times larger errors. Preliminary estimation of error in x-component of velocity along the axis of nozzle designed for supersonic MM expansion by Head et. al. for ORCHID reveals that maximum error is expected to be near throat which will amount to around 0.42% [31]. Also, fluids like D_4 or MDM are much more complex than MM and will exhibit refractive index derivatives of much larger magnitude resulting in velocity errors much higher than 1%. It is encouraging to know that the errors due to optical distortion can be estimated and since they are epistemic in nature, they can also be corrected. Such errors can either be estimated experimentally by Schlieren imaging or numerically using ray tracing.

6

CONCLUSION

Based upon the experimental and theoretical work described in the previous chapters certain inferences regarding feasibility of PIV in ORC working fluids is discussed. These conclusions are based on the results for the D_4 and MM medium. Following are the most important conclusions,

- The tracer particles which are conventionally used in ideal gas flows can be used in the fluids of interest. In fact, it was observed that due to higher density of the fluids of interest the particle response time is smaller than in ideal gas medium and therefore more accurate and can resolve smaller flow features.
- In case of supersonic expansion of MM, a large gradient of refractive index was observed because of large gradients in density. These refractive index gradients poses several potential challenges like errors in velocity due to optical distortions and reduction in field of view. These issues are expected to be more severe in more complex fluids.
- It was estimated that for the MM nozzle design of Head et. al. (2016) [31] the velocity error due to optical distortions at nozzle axis will be less than 0.5 %. The velocity error is proportional to the square of the distance between the measurement plane and the nozzle wall. The velocity error is expected to increase with the complexity of the fluid due to larger density gradients which will result in larger refractive index gradients. The errors are expected increase if the expansion occurs closer to the critical point due to higher densities.
- The velocity errors caused by optical distortions are epistemic in nature and can be corrected if an accurate estimation of the density gradients in the flow field is available. This is possible using Background-Oriented-Schlieren technique. A CFD result of the density distribution can be used to create synthetic Schlieren images using ray-tracing method which can be used to correct the velocity errors using simple image processing.
- It was also concluded that for the MM nozzle design by Head et. al. (2016) [31] that the difference between normal shifts in particle images at the throat and at the Mach 2.0 cross section is nor enough to cause problems with imaging. However, that difference could be larger than the focal depth of the camera for a larger nozzle or a more complex fluids which results in blurred particle images in certain segments of the image. This can be solved by reducing the field of view (i.e. magnification) or decreasing the camera aperture (i.e. increasing $f_{\#}$) which could result in diminished particle images.
- The metal oxide tracer particles can be satisfactorily atomized by evaporation of the siloxane + metal oxide suspensions. However, certain amount of agglomeration still exists which could cause problems after a longer duration of operation. Hence, a seeding strategy for vapour tunnel is proposed where the suspension of siloxane + metal oxide is evaporated first before introduction to the flow to minimize agglomeration and unwanted blockages.

It is concluded that PIV is feasible in low speed dense vapour flows. It is concluded that PIV could result in highly erroneous measurements in non-ideal compressible flows, however, the errors can be corrected with some effort. Feasibility of PIV in non-ideal compressible flow depends on design of a suitable seeding system and development of corrective measures for optical distortion errors. Based on this, some future works are recommended in following section.

6.1. FUTURE WORK

- Design of seeding system: It is well established from Sec. 2.2.3 that conventional seeding strategies of fluidization or atomization cannot be used for the vapour tunnels. A comprehensive design of seeding system for vapour tunnels is required that can operate at very high pressures and ensures no contamination of the vapour. The conceptual design proposed in the Sec. 4.4 can be taken as a starting point for this work.

- Experimental determination of the density gradients by means of Background Oriented Schlieren (BOS) should be done to estimate position and velocity errors in PIV data in compressible dense gas flows. The schlieren images can be used to correct for these errors. Alternatively, ray tracing simulations of the dense gas flows should be carried to simulate BOS images which can be very actively used for the corrections of the PIV data.

A

NON-IDEAL COMPRESSIBLE FLUID DYNAMICS

Non-Ideal Compressible Fluid Dynamics (NICFD) is the field of fluid mechanics that studies the fluid flows deviating from the ideal gas behaviour, especially when the fluid is in vicinity of the critical point. The non-ideal behaviour is defined in terms of the gradient of the speed of sound w.r.t. the thermodynamic properties. Landau and Lifshitz defines a parameter shown in the Eqn. A.1 which is referred as the fundamental derivative of gas dynamics (Γ)[59], where c is the speed of sound and s is entropy. For ideal gases, the Γ is a positive constant which means the speed of sound remains constant on variation of thermodynamic properties. For the ORC working fluids, the Γ varies with the other thermodynamic parameters and becomes negative near the critical point (Fig. A.1).

$$\Gamma = 1 + \frac{\rho}{c}\left(\frac{\partial c}{\partial \rho}\right)_s \tag{A.1}$$

The relationship between the thermodynamic properties namely, pressure (p), temperature (T), and density (ρ) is drastically different for the fluids mentioned in the Tab. 1.1 (dense gases) from what can be established by ideal gas equation of state. Several modified forms of equations of state for non-ideal fluids have been proposed throughout the history and some of them were discussed briefly in Sec. 1.2.1.

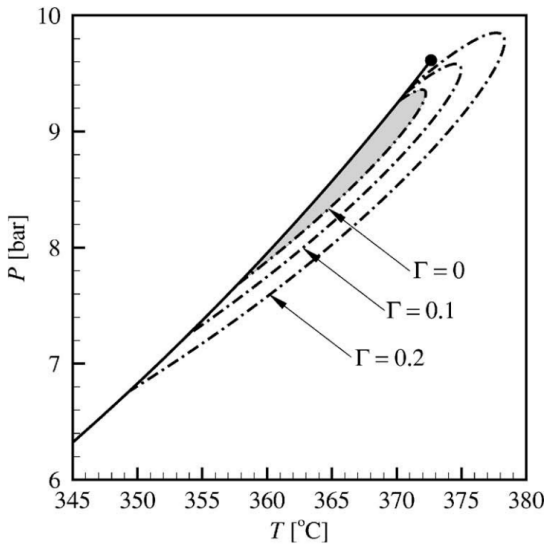

Figure A.1: Saturation curve of D_6 and iso-Γ lines < 1. Grey regions represents $\Gamma < 0$ (extracted from Ref. [8]).

B

IMAGE PRE-PROCESSING TECHNIQUES

B.1. POD BASED BACKGROUND REMOVAL

Mendez et.al. (2016) proposed a novel image processing technique to remove reflections and non-uniform noise from PIV images[50]. Consider the set of n_t PIV images (n_t = 1000 for NIVA work) where every 2-D image of dimensions $n_r \times n_c$ is reshaped into a single column of size $n_p = n_r n_c$, therefore, n_t such columns constitutes a 2-D matrix (X of size $n_p \times n_t$) representing the whole dataset. Any set of PIV images cannot constitute a matrix X (of rank r) such that it can be decomposed (or factorized) as shown in the Eqn. B.1, where, Φ_r is the orthonormal basis for the columns of X, Ψ_r is the orthonormal basis for the rows of X, and Σ_r is a diagonal matrix containing the norm of contributions from the factor matrices. This is also termed as singular value decomposition which is nothing but a discrete form of proper orthogonal decomposition.

$$X = \Phi_r \Sigma_r \Psi_r^T \tag{B.1}$$

The set of PIV images are approximated to a matrix $\tilde{X}$ of rank r ($r < min(n_p, n_t)$, generally for high resolution image acquizition $n_t << n_p$ which is also true in case of NIVA experiments) by solving the minimization problem defined by equation B.2, where E is minimized to obtain $\tilde{X}$[50]. And according to Eckart-Young theorem [60] the solution of the Eqn. B.2 satisfies the Eqn. B.1.

$$min(E) = min(||X - \tilde{X}||) \tag{B.2}$$

For application in PIV to remove background, X is assumed to be sum of the two matrices one corresponds to the particle images (X_p) and the other to the background (X_b) as shown in the Eqn. B.3 and both the components of X have their own singular value decomposition [50].

$$X = X_p + X_b = \Phi_p \Sigma_p \Psi_p^T + \Phi_b \Sigma_b \Psi_b^T \tag{B.3}$$

The decomposition of the PIV dataset as shown by the Eqns. B.1 and B.3 can also be written as a sum of the columns of the left hand term (i.e. sum of individual images over time) as shown by the Eqn. B.5 where s_i is the i^{th} column of X. In the Eqn. B.5 an image can be interpreted as sum of r spatial modes ϕ_k evolving over corresponding temporal modes ψ_k [50].

$$s_i = \sum_{k=1}^{r} \phi_k \sigma_k \psi_k^i \tag{B.4}$$

$$s_{pi} + s_{bi} = \sum_{k=1}^{r} \phi_{pk} \sigma_{pk} \psi_{pk}^i + \sum_{k=1}^{r} \phi_{bk} \sigma_{bk} \psi_{bk}^i \tag{B.5}$$

In a typical PIV image the background noise has a strong spatial and temporal correlation (i.e. X_b is a dense matrix) but the reflections may or may not have strong correlation [50]. In the image set obtained in NIVA experiments the reflections were from the symmetric rotating disk which makes reflections appear uniform in time. Since the reflections were only at certain locations (i.e. disk periphery) it is not uniform

in space. This means that the rank of the background matrix is significantly lower than the particle image matrix. This fact is very concisely depicted by the the Eqn. B.7 given in reference [50].

$$X_b = \sum_{k=1}^{r} \phi_{bk} \sigma_{bk} \psi_{bk}^T \tag{B.6}$$

$$\sigma_{bk} \approx 0, \forall k > r << n_t \tag{B.7}$$

Therefore, it can be said from B.7 that the reflection and background noise has only few dominant modes (unlike particle images)and can be removed. The following figure shows the result of removing the first two modes of background and it can be seen that the reflections are practically removed and sharper particle images can be observed.

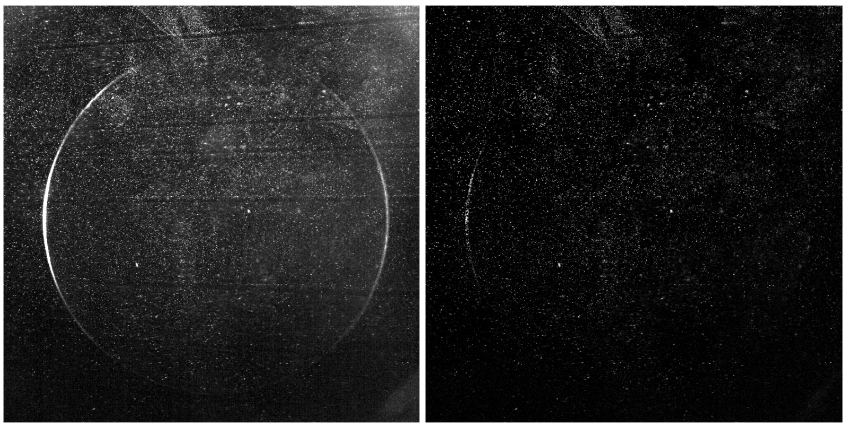

(a) (b)

Figure B.1: Result of POD based background removal.

C

NIVA Instantaneous Velocity Fields

C.1. 0 Hz Case

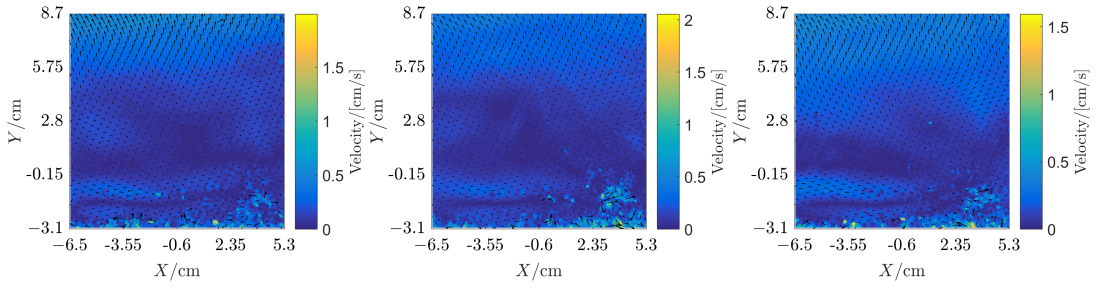

(a) t = 0 s (b) t = 0.833 s (c) t = 1.667 s

(d) t = 2.499 s (e) t = 3.333 s

Figure C.1: Instantaneous velocity fields at different time instances.

C.2. 10 HZ CASE

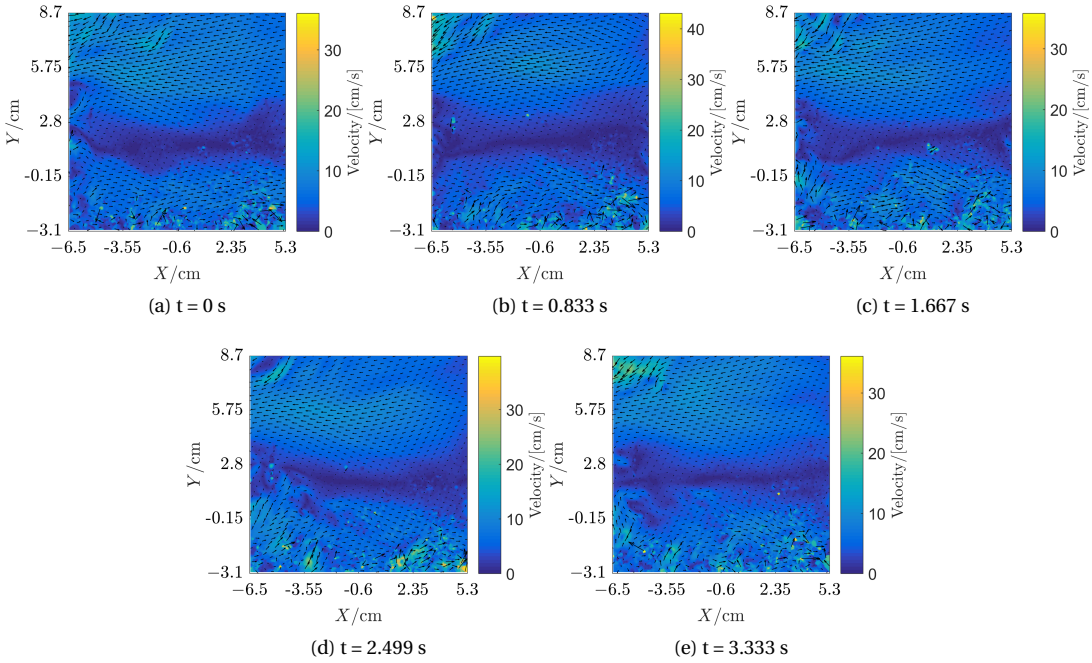

(a) t = 0 s (b) t = 0.833 s (c) t = 1.667 s

(d) t = 2.499 s (e) t = 3.333 s

Figure C.2: Instantaneous velocity fields at different time instances.

C.3. 20 HZ CASE

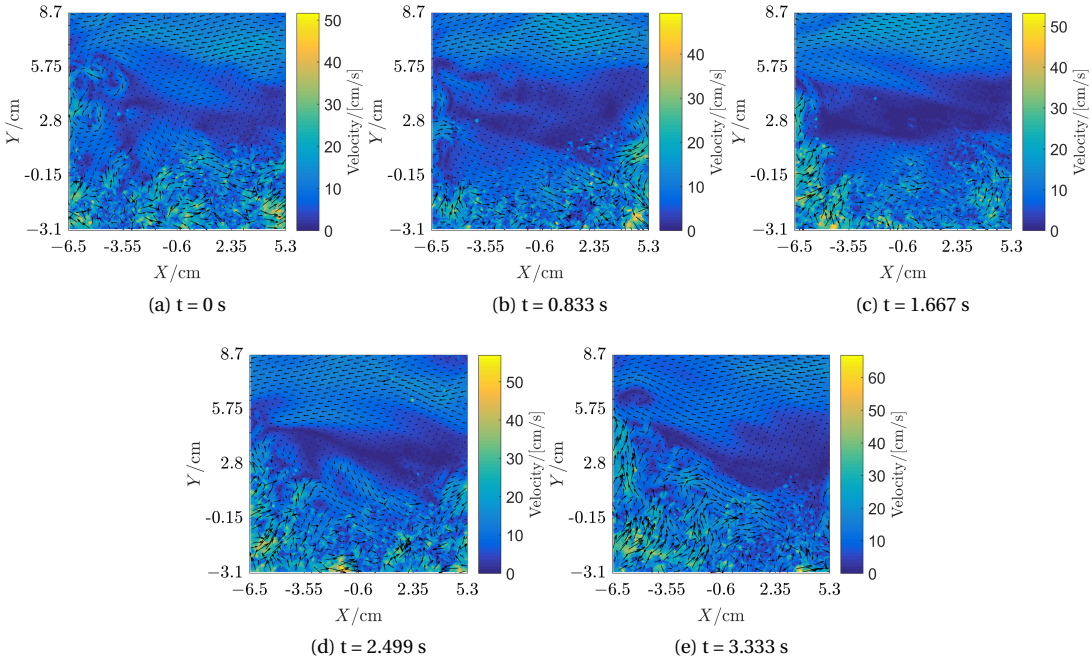

(a) t = 0 s (b) t = 0.833 s (c) t = 1.667 s

(d) t = 2.499 s (e) t = 3.333 s

Figure C.3: Instantaneous velocity fields at different time instances.

C.4. 30 Hz Case

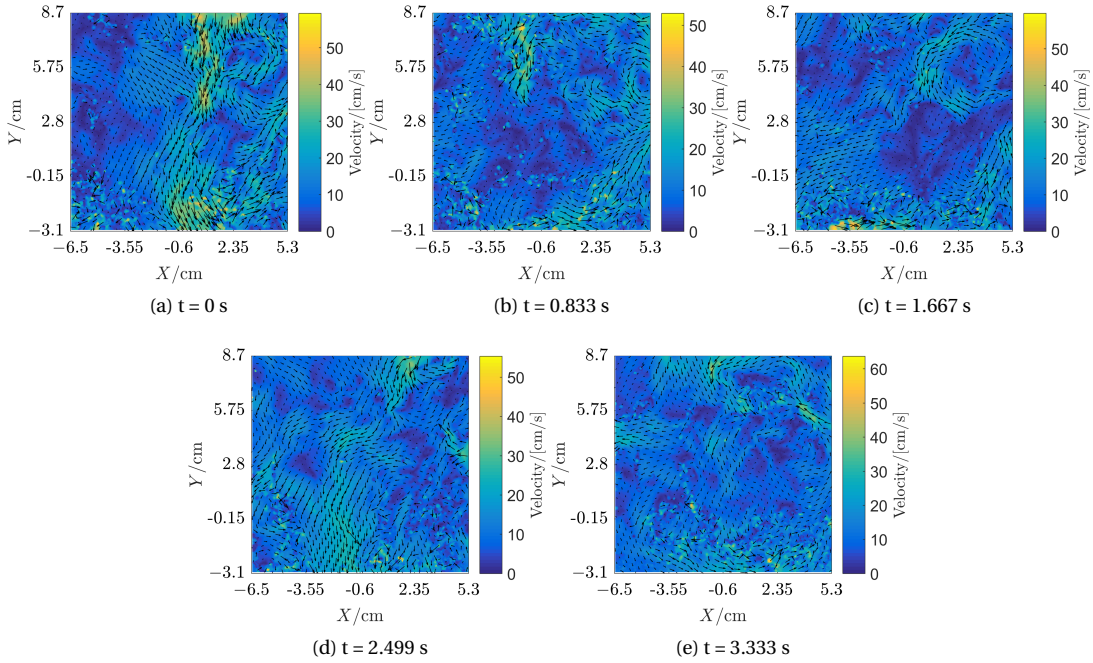

(a) t = 0 s (b) t = 0.833 s (c) t = 1.667 s

(d) t = 2.499 s (e) t = 3.333 s

Figure C.4: Instantaneous velocity fields at different time instances.

C.5. 40 Hz Case

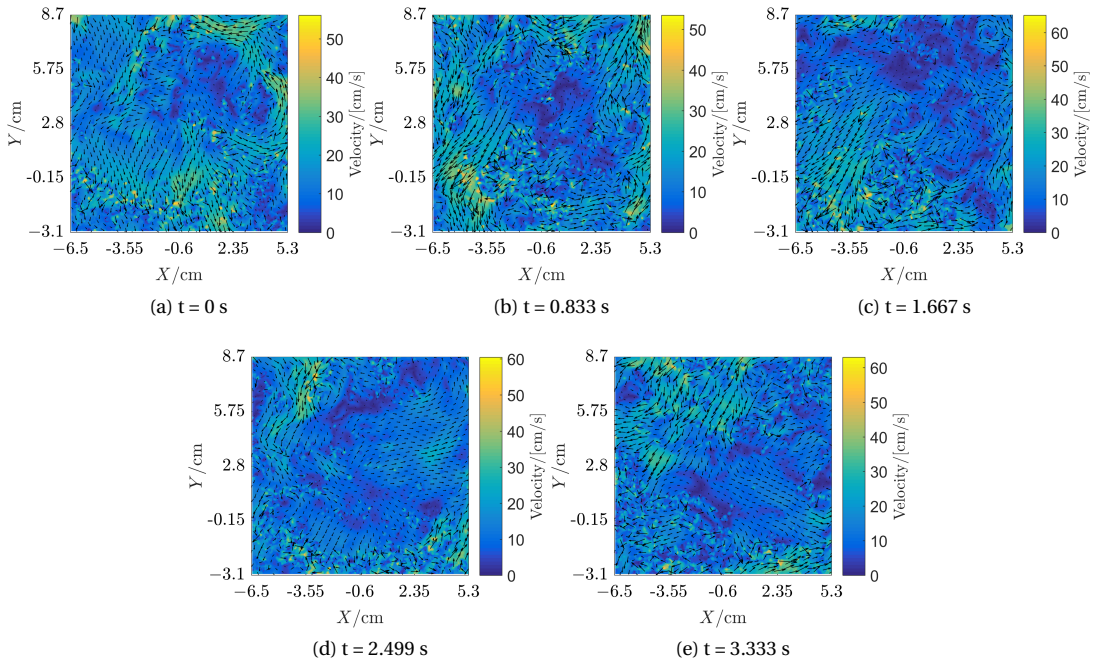

(a) t = 0 s (b) t = 0.833 s (c) t = 1.667 s

(d) t = 2.499 s (e) t = 3.333 s

Figure C.5: Instantaneous velocity fields at different time instances.

D

MISCELLANEOUS INFORMATION ON DAVIS

D.1. VECTOR PROCESSING IN DAVIS

In chapter 3 the images were processed using a multi-grid iterative algorithm with square windows and the settings can be seen in Fig. D.1.

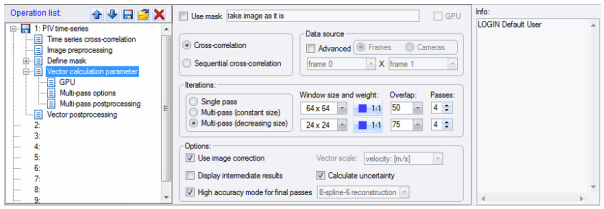

Figure D.1: Cross-correlation settings in DaVis

D.1.1. IN CHAPTER 5

The results presented in chapter 5 were obtained using the multi-grid iterative algorithm with circular windows shapes. Use of circular window shapes resulted in fewer outliers. The processing settings in DaVis can be seen in Fig. D.2.

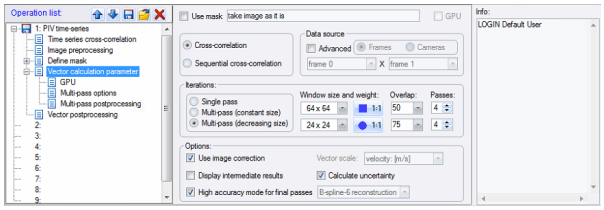

Figure D.2: Cross-correlation settings in DaVis

The processed images can be further filtered to remove the outliers using universal outlier detection. The settings describing the threshold and filter size is shown in Fig. D.3.

D.2. IMPORTING BACKGROUND REMOVED IMAGES

The images pre-processed using POD based background removal can be imported to DaVis by following the steps mentioned below,

Step 1. Press the "Import" button on top-left corner of the window.
Step 2. Go to the file path where images are saved.
Step 3. Select all the images and set the time between images. Press "Add to list".
Step 4. Press "Import Data" to import the pre-processed images.

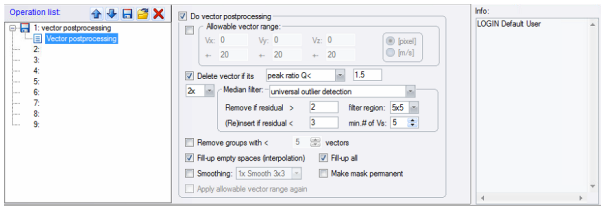

Figure D.3: Post-processing option in DaVis

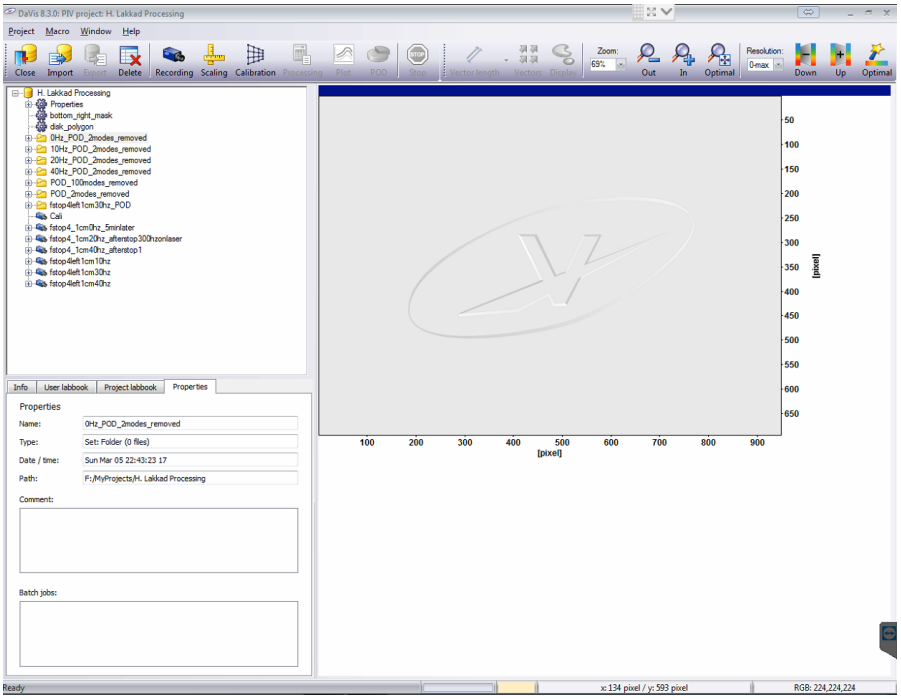

Figure D.4: Step 1

D.3. UNCERTAINTY QUANTIFICATION

In 2013 Sciacchitano et. al. developed Particle Disparity method where the measured velocity vector field is used to predict the individual particle images of each interrogation window. Ideally particle images of the second frame should match perfectly with the first frame particle images after adding the measured displacement, but in real measurements there exists a disparity between particle images of the two frames. Modern algorithms can calculate this disparity with sub-pixel accuracy and uncertainty of the measurement (Equation D.1) can be derived from the disparity vector distribution over the interrogation window [9]. A typical disparity vector distribution can be seen in Figure D.8. For a detailed investigation of variation of uncertainty with varying parameters like displacement, displacement gradient, out-of-plane motion, seeding density, particle image diameter, and background noise can be found in [9].

$$\delta = \sqrt{\mu^2 + (\frac{\sigma}{\sqrt{N}})^2} \tag{D.1}$$

Wieneke in 2014 proposed a method similar to the Particle Disparity method except that here the correlation peak was related to individual pixels instead of particle images. Similar to image matching method, here the uncertainty vriation was studied with varying parameters like pixel noise, out-of-plane motion, seeding density, and particle image size. Wieneke also mentions few limitations of the proposed methods like high standard deviations and variability of the determined uncertainty field, unreliability in cases of low seeding density (very few particles per interrogation window) is obvious since the variability itself depends on number of samples [61]. Sciacchitano et. al. reports a collaborative investigation in [62] where the four uncer-

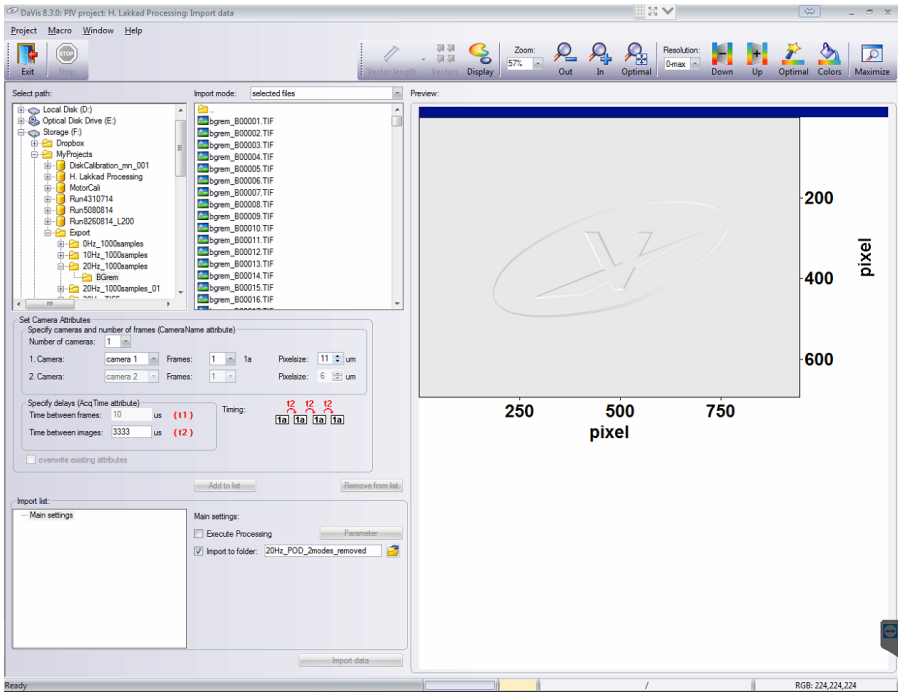

Figure D.5: Step 2

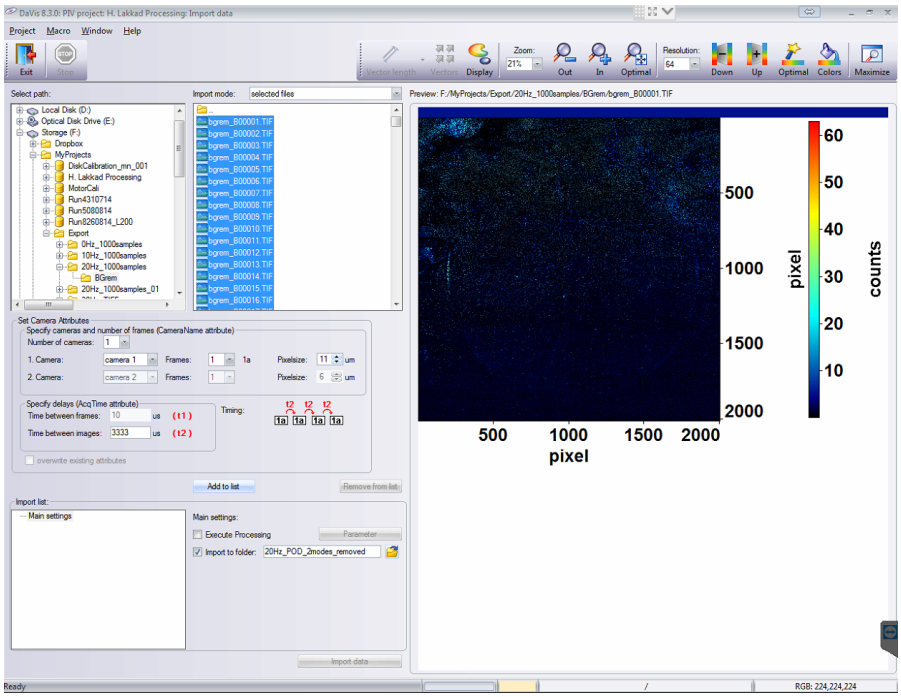

Figure D.6: Step 3

tainty quantification technique namely, Uncertainty Surface method, Particle Disparity method, Peak Ratio method, and Correlation Statistics methods are compared and advantages and limitations of each methods are discussed. The software DaVis implements the Weineke's method for assessment of uncertainty [61].

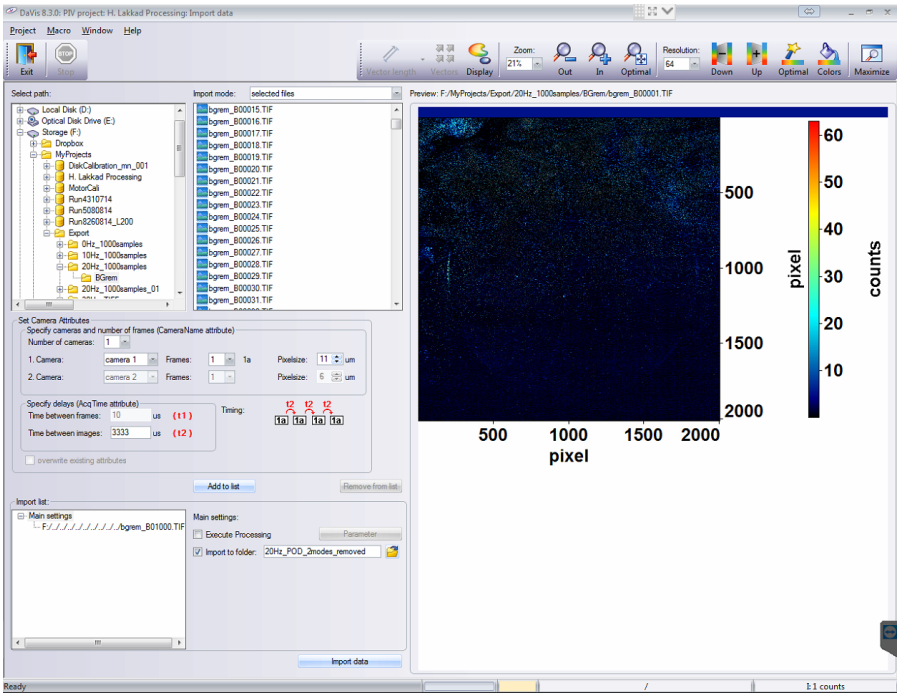

Figure D.7: Step 4

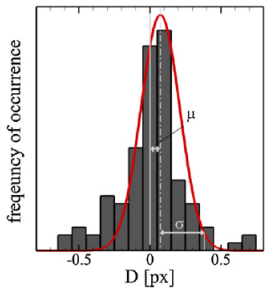

Figure D.8: Distribution of disparity over an interrogation window [9].

D.4. RELATIVE UNCERTAINTY

Process to extract the relative Uncertainty from a vector field. The following operations:

1. use the vector field: "extract scalar field: vector component" - "|V| vector length"

2. use the vector field: "extract scalar field: vector component" - "additional component" - in the parameter card select "Uncertainty V"

3. use the extracted vector length(1.): "basic image arithmetic" - "divide" - in the parameter card select "file:" and then use the length image created by step 2.

4. use result of 3.: "basic image arithmetic" - "multiply" - in the parameter card select "constant:" with value 100

5. use result of 4.: "scales" - "set scales by defined values" - in the parameter card change the Unit of the Intensity scale to "

If you want to display the result in the background of your vector field make sure that you use "Enlarge raw data" in the "extract scalar field: vector component" (step 1. and 2.)

D.5. PIV DATA QUALITY TABLE FROM NIVA

It can seen from Fig. 3.12 that the seeding practically vanishes at the bottom of the box. Consequently, it will also affect the overall quality of the PIV data. It is hence worthwhile to investigate the percentage of outliers and Q-factor in the regions of extremely low seeding. One can judge that the uniformity in seeding is satisfactory horizontally, but it various significantly vertically. From the Fig. 3.12 it can be inferred that the extremely low seeding (< 0.005 ppp) in the lower segment of dimensions $600X2016$ pixels. We divide the image into two horizontal segments whose dimensions can be seen in Fig. D.9 and the vector field results like outliers, avg. Q-factor, and peak locking were determined for these regions separately using the vector fields presented in Sec. 3.5.3. The vector fields obtained after TSM image processing were used for this analysis.

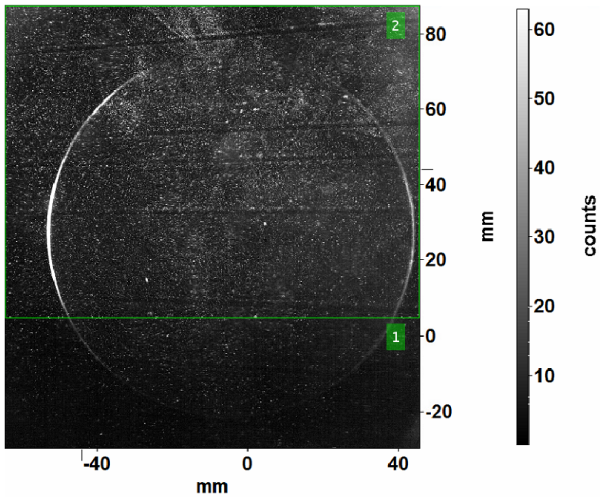

Figure D.9: Image division for analysing quality of data in different regions.

DaVis also shows the results like outliers and average Q-factor for a small rectangular regions selected by the user. Here the "rectangle 1" corresponds to the region below the green line in Figure D.9 and the "rectangle 2" corresponds to the region above it. Percentage outliers and average Q-factor for rectangle 1 and rectangle 2 were calculated for all interrogation window sizes used before. The quality of data when analysed separately for region with sufficient seeding is at par with generally accepted standard. From the data shown in Table D.1 the resolution of 24X24 interrogation window size yields acceptable vector field. Hence it can be concluded that the test section had sufficient seeding to yield correct vectors.

Speed	Segment	Size	16 × 16	24 × 24	32 × 32	48 × 48	64 × 64	96 × 96
0 Hz	Rectangle 1	% outliers	1.11	4.61	2.76	0.34	0.081	0.048
		Avg. Q-factor	2.00	2.41	2.57	2.69	2.75	2.83
		Peak lock	0.3128	0.4441	0.5319	0.6609	0.7371	0.8143
	Rectangle 2	% outliers	0.69	0.45	0.33	0.23	0.036	0.061
		Avg. Q-factor	2.59	2.85	2.95	2.98	2.99	3.00
		Peak lock	0.5543	0.6467	0.6887	0.7194	0.7291	0.7372
10 Hz	Rectangle 1	% outliers	2.08	7.62	5.87	1.98	0.94	0.048
		Avg. Q-factor	1.63	2.16	2.32	2.44	2.49	2.60
		Peak lock	0.0201	0.0359	0.0565	0.0957	0.1241	0.1390
	Rectangle 2	% outliers	0.7	0.65	0.44	0.16	0.045	0.04
		Avg. Q-factor	2.59	2.83	2.92	2.97	2.98	2.99
		Peak lock	0.0382	0.0430	0.0467	0.0459	0.0466	0.0417
20 Hz	Rectangle 1	% outliers	3.08	18.02	21.61	12.99	6.72	3.57
		Avg. Q-factor	1.43	2.10	2.35	2.54	2.59	2.57
		Peak lock	0.0007	0.0080	0.0354	0.1400	0.3403	0.4134
	Rectangle 2	% outliers	0.94	1.94	1.54	0.83	0.42	0.79
		Avg. Q-factor	2.12	2.58	2.76	2.88	2.90	2.90
		Peak lock	0.0297	0.0302	0.0240	0.0183	0.0077	0.0026
30 Hz	Rectangle 1	% outliers	2.32	14.28	17.21	18.9	14.88	10.14
		Avg. Q-factor	1.57	2.14	2.38	2.53	2.59	2.62
		Peak lock	0.0026	0.0006	0.0008	0.0013	0.0149	0.0213
	Rectangle 2	% outliers	1.34	3.61	2.65	3.11	3.62	4.86
		Avg. Q-factor	2.11	2.58	2.76	2.87	2.90	2.87
		Peak lock	0.0190	0.0162	0.0168	0.0105	0.0137	0.0118
40 Hz	Rectangle 1	% outliers	2.76	14.6	15.74	17.31	15.93	12.9
		Avg. Q-factor	1.64	2.14	2.34	2.51	2.57	2.63
		Peak lock	0.0030	0.0037	0.0073	0.0093	0.0131	0.0291
	Rectangle 2	% outliers	1.57	4.19	3.76	3.90	5.34	5.39
		Avg. Q-factor	2.11	2.56	2.75	2.86	2.89	2.87
		Peak lock	0.0124	0.0121	0.0105	0.0049	0.0065	0.0019

Table D.1: Interrogation window size wise % of outliers in two different regions.

E

MATLAB CODES

Some miscellaneous methods and the MATLAB routines used in this work are reported in this appendix.

E.1. EULER SHOCK WAVE CALCULATOR

Consider an OSW in the fluid of interest as shown in the Fig. 4.9. Let the Mach no. upstream and downstream of the OSW be M_1 and M_2, and velocities be V_{n_1} and V_{n_2} respectively. For supersonic flow of ideal gas, β, θ, and M_1 are related by a closed expression, however, it is not the case for the fluids that does not obey the ideal gas equation of state. For these fluids the relation between β and θ is given in terms of the density ratio ($\hat{r} = \frac{\rho_1}{\rho_2} = \frac{V_{n_2}}{V_{n_1}}$, where V_{n_i} is the velocity component normal to the OSW) as shown in Eqn. E.1.

$$tan\beta = \frac{(1-\hat{r}) \pm [(1-\hat{r})^2 - 4\hat{r}\,tan^2\theta]^{1/2}}{2\hat{r}\,tan\theta} \tag{E.1}$$

Using the Eqn. E.1 and the Rankine-Hugoniot[1] equations the jump conditions are calculated using an iterative procedure presented by Grossman (2000) where the thermodynamic properties and the speed of sound in the fluid of interest can be calculated using REFPROP [63]. The procedure is described as follows,

1. The flow conditions upstream of the OSW i.e. V_1, p_1, ρ_1 are and and the. Using upstream conditions calculate enthalpy $h_1(p_1, \rho_1)$ using REFPROP.
2. Assume a value of density ratio and calculate downstream density using $\rho_2 = \frac{\rho_1}{\hat{r}}$.
3. Using Eqn. E.1 calculate β and along with it the upstream velocity component normal to the OSW, $V_{n_1} = V_1 sin\beta$. Eqn. E.1 gives two solutions (corresponding to $\pm$) however, only the solution that corresponds to $-$ is the weak shock solution because according to the second law of thermodynamics the occurrence of weak solution takes preference over the strong solution.
4. Using Rankine-Hugoniot equations calculate the downstream variables, $V_{n_2} = \frac{\rho_1}{\rho_2} V_{n_1}$, $p_2 = p_1 + \rho_1 V_{n_1}^2 (1 - \hat{r})$, and $h_2 = h_1 + \frac{V_{n_1}^2}{2}(1 - \hat{r}^2)$.
5. Obtain downstream enthalpy using equation of state i.e. $\hat{h}_2(p_2, \rho_2)$.
6. Compare $\hat{h}_2$ and h_2. If $\hat{h}_2 \neq h_2$ then repeat from step 2 with a modified $\hat{r}$ until a convergence of $\hat{r}$ is achieved.

E.1.1. CODE

```
% Conditios upstream of the OSW
u_before = M1*sos;
p_before =  p1;
rho_before = rho1;
```

[1] Rankine-Hugoniot equations is a set of general conservation equations of mass, momentum, and energy across a shock wave.

```
Beta_wlist = [];
Theta_wlist = zeros(1,1)';
Options=optimset('Display','Off','MaxIter',3000,'MaxFunEvals',3000, 'TolFun', 1.0e-12, 'TolX',1.0
Nit = 199;
v_guessvector = [0.99:-1/(Nit+1):0.001];
flip = 0; %A switch to determine whether on not to store beta
iterate = 0;
% Thetalist = 0.01:10:25;
Thetalist = 11.51;
% Thetalist = 6:10:25;


%%%%%%%%%%%%%%%%%%%%%%%%%%Weak Shock Wave %%%%%%%%%%%%%%%%%%%%%%%%%%%%%%%%
for k = 1:size(Thetalist,1)
    %Step 6
    for j = 1:size(Thetalist,2)              % The downstream flow inclination angle. aka Wedge A
        Theta = Thetalist(j);
        v_guessfinallist(1) = 1;
        for i = 1:Nit-1
            v_guess = v_guessvector(i);
            try
                [v_guessfinal,~,exitflag] = fsolve(@(v_guess)(JumpConOblique(u_before(k), p_befor
                v_guessfinallist(i) = v_guessfinal;
                if exitflag <= 0
                    %                 warning('v_guess is not a sln');
                    v_guessfinal = 1.5;
                end

                Beta_weak = precalcBeta_weak(p_before(k), rho_before(k), v_guessfinal, Theta ,Flu

                if v_guessfinal >= 0 && v_guessfinal < 0.99999 && Beta_weak < 90 && Beta_weak > 0
                    if imag(Beta_weak) == 0
                        break
                    end
                end
            catch
            end

        end
        if i == Nit-1
            flip = 1;
            %             Theta_max = Thetalist(j-1); Theta max is when the strong
            %             oblique shock sln becomes complex.
            warning('Some weak Oblique shock slns are complex');
            if isempty(Beta_wlist) == 1;
                fprintf('never attached a weak shock at this mach number at all the thetas = %3.8
            end
            break
        end
        flip = 0;

        if i == Nit-1
            flip = 1;
        end
```

```
        if flip == 0
            try


                %Step 1
                [h_before,ErrorMsg] = invoke(Fluid,'Enthalpy','Pd',p_before(k),rho_before(k));
                ErrorCheck(ErrorMsg);
                %Step 2

                rho_after = rho_before(k)/v_guessfinal;
                %Step 3
                %Step 3 A: Calulation of the weak angles
                A = (1-v_guessfinal);
                B = sqrt((1-v_guessfinal)^2-4*v_guessfinal*(tand(Theta))^2);
                C = 2*v_guessfinal*tand(Theta);
                Beta_weak = atand((A - B )/C); %The -ve sln corresponds to a weak oblique shock
                %             Beta_weak = abs(Beta_weak); %Complex solutions are an
                %             indcation of detatchement or theta max. Or simply an
                %             inability to continue with the weak. See the strong.

                if Beta_weak < 0 || Beta_weak >= 90
                    Beta_weak = NaN;
                end
               % Mach_angle = asind(1/M_3);
                %             if imag(Beta_strong) == 0
                %                 Beta_strong = atand((A + B )/C);
                %             else
                %                 Beta_strong = NaN;
                %             end

                %Step 3 C: Calulation of the normal shock velocity based on
                %weak shock
                u_nbefore = u_before(k)*sind(Beta_weak); %Normal velocity before the shock

                %Step 4
                u_nafter = u_nbefore*v_guessfinal; %Normal velocity after shock
                p_after = p_before(k) + rho_before(k)*(u_nbefore^2)*(1-v_guessfinal); %Pressure after s
                h_after = h_before + (u_nbefore^2/2)*(1-v_guessfinal^2); %Enthalpy after shock
                %Step 5
                [h_tildaafter,ErrorMsg] = invoke(Fluid,'Enthalpy','Pd',p_after,rho_after);
                ErrorCheck(ErrorMsg); %Enthalpy from the equation of state

                %After Convergence
                u_after = u_nafter/sind(Beta_weak-Theta);

%                 M = MOC.Mach(k);
                %Other static properties
                [sos_after,ErrorMsg]    = invoke(Fluid,'SoundSpeed','Ph',p_after,h_after);
                ErrorCheck(ErrorMsg);
                [sos_before,ErrorMsg]    = invoke(Fluid,'SoundSpeed','Ph',p_before(k),h_before);
                ErrorCheck(ErrorMsg);

                M_before = u_before(k)/sos_before;%
                M_after = u_after/sos_after;%
                M_nbefore = u_nbefore/sos_before;%
                M_nafter = u_nafter/sos_after;  % Normal Mach number after shock
```

```
                %---- Calculation of stagnation properties flow velocity direction
                %%%%%%
                h_01 = h_before + 0.5*u_before(k)^2;
                [s_1,ErrorMsg] = invoke(Fluid,'Entropy','Pd',p_before(k),rho_before(k));
                ErrorCheck(ErrorMsg);
                [P_01,ErrorMsg] = invoke(Fluid,'Pressure','hs',h_01,s_1);
                ErrorCheck(ErrorMsg);

                h_02 = h_after + 0.5*u_after^2;
                [s_2,ErrorMsg] = invoke(Fluid,'Entropy','Pd',p_after,rho_after);
                ErrorCheck(ErrorMsg);
                [P_02,ErrorMsg] = invoke(Fluid,'Pressure','hs',h_02,s_2);
                ErrorCheck(ErrorMsg);
            end
        end
    end
end


function h_after = JumpConOblique(u_before, p_before, rho_before, v_guess, Theta ,Fluid)

%Step 1
[h_before,ErrorMsg] = invoke(Fluid,'Enthalpy','Pd',p_before,rho_before);
ErrorCheck(ErrorMsg);
%Step 2

rho_after = rho_before/v_guess;
%Step 3
%Step 3 A: Calulation of the strong and weak angles
A = (1-v_guess);
B = sqrt((1-v_guess)^2-4*v_guess*(tand(Theta))^2);
C = 2*v_guess*tand(Theta);

Beta_strong = atand((A + B )/C); %The +ve sln corresponds to a strong oblique shock

Beta_weak = atand((A - B )/C); %The -ve sln corresponds to a weak oblique shock

Beta_weak = abs(Beta_weak);

%Step 3 B: Calulation of the normal shock velocity
u_nbefore = u_before*sind(Beta_weak); %Normal velocity before the shock

%Step 4
u_nafter = u_nbefore*v_guess; %Normal velocity after shock
p_after = p_before + rho_before*(u_nbefore^2)*(1-v_guess); %Pressure after shock
h_after = h_before + (u_nbefore^2/2)*(1-v_guess^2); %Enthalpy after shock

end


function h_tildaafter = CurveFitOblique(u_before, p_before, rho_before, v_guess, Theta ,Fluid)

%Step 1
[h_before,ErrorMsg] = invoke(Fluid,'Enthalpy','Pd',p_before,rho_before);
ErrorCheck(ErrorMsg);
```

```
%Step 2

rho_after = rho_before/v_guess;
%Step 3
Beta_strong = atand(((1-v_guess)+sqrt((1-v_guess)^2-4*v_guess*(tand(Theta))^2))/(2*v_guess*tand(Theta)))
Beta_weak = atand(((1-v_guess)-sqrt((1-v_guess)^2-4*v_guess*(tand(Theta))^2))/(2*v_guess*tand(Theta)));

Beta_weak = abs(Beta_weak);

u_nbefore = u_before*sind(Beta_weak); %Normal velocity before the shock

%Step 4
u_nafter = u_nbefore*v_guess; %Normal velocity after shock
p_after = p_before + rho_before*(u_nbefore^2)*(1-v_guess); %Pressure after shock
%h_after = h_before + (u_nbefore^2/2)*(1-v_guess^2); %Enthalpy after shock
%Step 5
[h_tildaafter,ErrorMsg] = invoke(Fluid,'Enthalpy','Pd',p_after,rho_after);
ErrorCheck(ErrorMsg); %Enthalpy from the equation of state


end
```

E.2. VAPOUR VISCOSITY PLOT

```
% Fluid names in REFPROP. MM_mod is duplicate of MM file with nonane as
% reference fluid instead of nitrogen
Fluids = [string('D4'),string('MM'),string('MM_mod')];

% Required constants
Ru = 8314;
MW = [296.61576, 162.3775, 162.3775]; % Molecular mass
R = Ru./MW;

% Initializing range of T and P allowed in REFPROP
nT = 100;
nP = 100;
T = linspace(300,673,nT);
P = linspace(100,2500,nP);

% Determining fluid viscosity
for i = 1:size(Fluids,2)

    [Tcr(i), Pcr(i)] = refpropm('TP','C',0,' ',0,char(Fluids(i)));
    P_sv{i} = linspace(100,Pcr(i)-1,100);
    T_sv{i} = linspace(300,Tcr(i)-1,100);
    for j = 1:size(P,2)
        Rho_sv{i}(j) = refpropm('D','P',P_sv{i}(j),'Q',1,char(Fluids(i)));
        Rho_sl{i}(j) = refpropm('D','P',P_sv{i}(j),'Q',0,char(Fluids(i)));
        for k = 1:size(T,2)
            Rho{i}(j,k) = refpropm('D','T',T(k),'P',P(j),char(Fluids(i)));
            S{i}(j,k) = refpropm('S','T',T(k),'P',P(j),char(Fluids(i)));
            S_sv{i}(k) = refpropm('S','T',T_sv{i}(k),'Q',1,char(Fluids(i)));
            S_sl{i}(k) = refpropm('S','T',T_sv{i}(k),'Q',0,char(Fluids(i)));
            mu_dy{i}(j,k) = refpropm('V','T',T(k),'P',P(j),char(Fluids(i)));
        end
    end
```

```
end

% Determining vapour saturation curve
for i = 1:size(Fluids,2)
    var1{i} = S_sv{i};
    var2{i} = T_sv{i};
    Q1_curve{i} = polyfit(var1{i},var2{i},1);
end

% Determining vapour phase viscosity
for i=1:size(Fluids,2)
    P_all{i} = linspace(100,Pcr(i),100);
    T_all{i} = linspace(300,673,100);
    for j = 1:size(P_all{i},2)
        for k = 1:size(T_all{i},2)
            Rho_all{i}(j,k) = refpropm('D','T',T_all{i}(k),'P',P_all{i}(j),char(Fluids(i)));
            mu_all{i}(j,k) = refpropm('V','T',T_all{i}(k),'P',P_all{i}(j),char(Fluids(i)));
            S_all{i}(j,k) = refpropm('S','T',T_all{i}(k),'P',P_all{i}(j),char(Fluids(i)));
            pos = T_all{i}(k) - polyval(Q1_curve{i},S_all{i}(j,k));
            if(pos<0)
                P_vap{i}(j) = P_all{i}(j);
                T_vap{i}(k) = T_all{i}(k);
                Rho_vap{i}(j,k) = Rho_all{i}(j,k);
                mu_vap{i}(j,k) = mu_all{i}(j,k);
                S_vap{i}(j,k) = S_all{i}(j,k);
            end
        end
    end
end

% Assigning NaN values to liquid phase viscosity so that it does not appear
% in the plot
for i = 1:size(Fluids,2)
    for j = 1:size(P_vap{i},2)
        for k = 1:size(T_vap{i},2)
            if (S_vap{i}(j,k) == 0)
                S_vap{i}(j,k) = NaN;
                mu_vap{i}(j,k) = NaN;
                Rho_vap{i}(j,k) = NaN;
            end
        end
    end
end

n = 1; % Index of the fluid to be plotted, for e.g. n = 2 is MM

% Plotting vapour viscosity isotherms
for j = 1:size(T_vap{n},2)
    figure(1)
    plot(P_vap{n}/Pcr(n),mu_vap{n}(:,j),'k');
    hold on;
end
xlabel('Reduced pressure');
ylabel('$\textrm{Viscosity}/(\textrm{Pa}\cdot\textrm{s})$','Interpreter','Latex');
set(gca,'fontsize',15);
```

```
% Plotting vapour viscosity isobars
for j = 1:size(P_vap{n},2)
    figure(2)
    plot(T_vap{n}/Tcr(n),mu_vap{n}(j,:),'k');
    hold on;
end
xlabel('Reduced Temperature');
ylabel('$\textrm{Viscosity}/(\textrm{Pa}\cdot\textrm{s})$','Interpreter','Latex');
xlim([0.75 1.3]);
set(gca,'fontsize',15);
```

E.3. MOLECULAR COMPLEXITY PLOT

```
% Fluid names in REFPROP.
Fluids = [string('D4'),string('MM'),string('MDM'),string('D5'),string('D6'),...
    string('toluene'), string('nonane'), string('benzene'), string('ioctane'),...
    string('ethanol'), string('R245fa'), string('c12')];

% Required constants
R = 8314;
Tr = 0.7; % Molecular complexity defined at reduced temperature of 0.7
dT = 1;
MW = [296.61576, 162.3775, 236.53146, 370.77, 444.9236, 92.138, 128.26,...
    78.112, 114.23, 46.068, 134.05, 170.34]; % Molecular mass
R_specific = R./MW;


for i = 1:size(Fluids,2)

    % Getting critical parameters
    [Tcr(i), Pcr(i)] = refpropm('TP','C',0,' ',0,char(Fluids(i)));
    T_def(i) = Tr.*Tcr(i);
    T{i} = 300:dT:(Tcr(i)-1);
    Pvp{i} = 500:100:5000;
    [Min_delT(i),indx(i)] = min(abs(T{i}-T_def(i)));

    % Saturation curve viscosity values
    for j = 1:size(T{i},2)
        S_sv{i}(j) = refpropm('S','T',T{i}(j),'Q',1,char(Fluids(i)));
    end

    % Molecular complexity
    Sigma(i) = (Tcr(i)/R_specific(i))*(S_sv{i}(indx(i)+1) - S_sv{i}(indx(i)))/dT;

end

% Plotting molecular complexity vs molecular mass
figure(1)
plot(MW,Sigma,'*');
xlabel('$\textrm{Molecular mass}/(\textrm{g/mol})$');
ylabel('$\sigma /[-]$','Interpreter','Latex');
set(gca,'fontsize',15);
```

E.4. PARTICLE EQUATION OF MOTION

```
% Fluid velocity upstream nad downstream of OSW
```

```
ufi = 337.3911; %MM 187.0079 D4 146.8618 Air 337.3911 %T1 MM 525 D4 594
uff = 220.7865; %MM 119.361 D4 93.6687 Air 220.7865 %P1 MM 18.4 D4 14.7

% Denisty and viscosity of fluid, denisty and diameter of particles
mu_f = 1.3251e-5; %MM 1.5538e-5 D4 1.5e-5 Air 1.3251e-5
rho_f = 0.8257; %D4 15.488 MM 13.5026; Air %0.8257; MM rho_before 8.62
rho_p = 4000;
dp = 0.27e-6;

% Analytical value of time constant using Melling's drag formulation
C = 18*mu_f/(rho_p*dp*dp);

% ODE45 solver options and plotting style specifiers
options = odeset('RelTol',1e-6,'AbsTol',1e-10);
clrs = {'b','r','g','k'};
mrkrs = {'.','x','^','s','d','>','<'};

for i = [1 2 3]
[t,up] = ode45(@(t,up)stokeseqn(t,up,uff,i,mu_f,rho_f,rho_p,dp),linspace(0,1e-4,100000),ufi,optic
load('Un_t.mat');
load('Un_s.mat');
Rep{i} = rho_f*abs(up-uff)*dp/mu_f;

x = 0;
x2(1) = 0;

for j = 1:length(up)-1

    % Calculatng distance travelled by particle from the OSW
    um(j) = (up(j)+up(j+1))/2;
    dt(j) = (t(j+1)-t(j));
    dx{i}(j) = um(j)*dt(j);
    x2(j+1) = x2(j) + dx{i}(j);

    % Determining relaxation time and distance
    if abs(up(j)-uff)>abs(uff-ufi)*(1/exp(1))
        tau(i) = t(j);
        xi(i) = x2(j);
    end
end
x(i) = sum(dx{i});

% Particle velocity vs. distance from the OSW
figure(1)
plot(x2*1000,abs((up-uff)./(uff-ufi)),'Marker',mrkrs{i},'Color','k');
hold on;
xlim([0 3]);
clear x2;
legend({'$\textrm{C}_{\textrm{D,Melling}}$','$\textrm{C}_{\textrm{D,Oseen}}$',...
    '$\textrm{C}_{\textrm{D,Goldstein}}$'},'Interpreter','latex');
xlabel('Distance normal to shock/(mm)','Interpreter','latex');
ylabel(['$\frac{(\textrm{u}_{\textrm{f,f}}-\textrm{u}_{\textrm{p}})}'...
    '{(\textrm{u}_{\textrm{f,f}}-\textrm{u}_{\textrm{f,i}})}$'],'Interpreter','latex');

% Particle velocity vs. time
figure(2)
```

```
plot(t*(1e6),abs((up-uff)./(uff-ufi)),'Marker',mrkrs{i},'Color','k');
hold on;
xlim([0 2]);
clear x2;
legend({'$\textrm{C}_{\textrm{D,Melling}}$','$\textrm{C}_{\textrm{D,Oseen}}$',...
    '$\textrm{C}_{\textrm{D,Goldstein}}$'},'Interpreter','latex');
xlabel('$\textrm{Time}/(\mu \textrm{s})$','Interpreter','latex');
ylabel(['$\frac{(\textrm{u}_{\textrm{f,f}}-\textrm{u}_{\textrm{p}})}'...
    '{(\textrm{u}_{\textrm{f,f}}-\textrm{u}_{\textrm{f,i}})}$'],'Interpreter','latex');
end

% Experimental data in air from Scarano and Oudheusden (2003)
figure(1)
plot(Un_s(:,1),Un_s(:,2),'ko');

% ODE45 function
function dudt = stokeseqn(t,up,uff,cdi,mu_f,rho_f,rho_p,dp)

Rep = rho_f*abs(up-uff)*dp/mu_f;
switch cdi
    case 1 %Melling
        Cd = 24./Rep;
    case 2 %Oseen
        Cd = (24./Rep).*(1 + 3.*Rep./16);
    case 3 % Goldstein
        Cd = (24./Rep).*(1 + (3.*Rep./16) - 19.*Rep.*Rep./1280);
end
k = 3*mu_f/(4*rho_p*dp*dp);
dudt = k*Cd.*Rep.*(uff-up);
end
```

E.5. PARTICLE IMAGE COUNT

```
function [numP,intP,j_part,i_part,count_ker,counter] = find_particles(im,intensity_treshold,rk)

%rk=1;

im_size_y = size(im,1);
im_size_x = size(im,2);

%% Count particles
numP=0;
for j=1:im_size_y
    for i=1:im_size_x
        counter=0;
        count_ker=0;
        for ip=i-rk:i+rk
            for jp=j-rk:j+rk
                if ip >= 1 && ip <=im_size_x
                    if jp >= 1 && jp <=im_size_y
                        count_ker=count_ker+1;
                        if im(j,i) > im(jp,ip) && im(j,i) > intensity_treshold
                            counter=counter+1;
                        end
                    end
                end
```

```
            end
        end
        if counter/(count_ker-1) == 1
            numP=numP+1;
        end
    end
end

%% Find particles
% np=max(num_part(:));
i_part=zeros(numP,1);
j_part=zeros(numP,1);
intP=zeros(numP,1);

numP=0;
for j=1:im_size_y
    for i=1:im_size_x
        counter(j,i)=0;
        count_ker(j,i)=0;
        for ip=i-rk:i+rk
            for jp=j-rk:j+rk
                if ip >= 1 && ip <=im_size_x
                    if jp >= 1 && jp <=im_size_y
                        count_ker(j,i)=count_ker(j,i)+1;
                        if im(j,i) > im(jp,ip) && im(j,i) > intensity_treshold
                            counter(j,i)=counter(j,i)+1;
                        end
                    end
                end
            end
        end
        if counter(j,i)/(count_ker(j,i)-1) == 1
            numP=numP+1;
            i_part(numP)=i;
            j_part(numP)=j;
            intP(numP)=im(j,i);
        end
    end
end
```

BIBLIOGRAPHY

[1] A. P. S. Wheeler and J. Ong, *The role of dense gas dynamics on organic rankine cycle turbine performance,* Journal of Engineering for Gas Turbine and Power **135** (2013).

[2] A. P. S. Wheeler and J. Ong, *A study of the three-dimensional unsteady real-gas flows within a transonic orc turbine,* in *Proceedings of the ASME Turbo Expo 2014* (2014).

[3] A. Spinelli, A. Guardone, F. Cozzi, M. Carmine, R. Cheli, M. Zocca, P. Gaetani, and V. Dossena, *Experimental observation of non-ideal nozzle flow of siloxane vapor mdm,* in *3rd International Seminar on ORC Power Systems* (2015).

[4] J. Westerweel, G. E. Elsinga, and R. J. Adrian, *Particle image velocimetery for complex and turbulent flow,* Annual Review of Fluid Mechanics , 369 (2013).

[5] S. Gallarini, *Design and Commissioning of a Laser Doppler Velocimetry seeding system for non-ideal fluid flows,* Master's thesis, Politecnico di Milano (2016).

[6] M. Raffel, C. E. Willert, S. T. Wereley, and J. Kompenhans, *Particle Image Velocimetry: A practical guide* (Springer, 2007).

[7] A. Melling, *Tracer particle and seeding for particle imag velocimetry,* IOPscience (1997).

[8] P. Colonna, A. Guardone, N. R. Nannan, and C. Zamfirescu, *Design of the dense gas flexible asymmetric shock tube,* Journal of Fluids Engineering **130** (2008).

[9] A. Sciacchitano, B. Wieneke, and F. Scarano, *Piv uncertainty quantification by image matching,* IOPscience (2013).

[10] A. Head, C. Servi, E. Casati, and P. Colonna, *Design Specification And Requirements of the ORCHID Set-up,* Tech. Rep. (Delf University of Technology, 2015).

[11] M. Thol, T. Windmann, R. Span, and J. Vrabec, *Thermodynamic properties of octamethylcyclotetrasiloxane,* Journal of Chemical and Engineering Data (2016).

[12] P. Colonna, E. Casati, C. Trapp, T. Mathijssen, J. Larjola, T. Saaresti, and A. Uusitalo, *Organic rankine cycle power systems: A review,* Eng. Gas Turbine Power (2015).

[13] C. Invernizzi, *Closed Power Cycle: Thermodynamic Fundmentals and Applications* (Springer, 2013).

[14] J. D. van der Waals, *De Continuiteit Van Den Gas-en Vloeistoftoestand,* Ph.D. thesis, Hoogeschool Leiden (1873).

[15] B. Poling, J. M. Prausnitz, and O. J. P., *The Properties of Gases and Liquids* (McGraw-Hill, 2001).

[16] P. Colonna, N. R. Nannan, A. Guardone, and E. W. Lemmon, *Multiparameter equations of state for selected siloxanes,* Fluid Phase Equilibria, Elsevier (2006).

[17] M. Thol, T. Windmann, R. Span, and J. Vrabec, *Fundamental equation of state correlation for hexamethyldisiloxane based on experimental and molecular simulation data.* Fluid Phase Equilibria (2015).

[18] E. W. Lemmon, M. L. Huber, and M. O. McLinden, *NIST Standard Reference Database 23: Reference Fluid Thermodynamic and Transport Properties-REFPROP, version 9.0,* Tech. Rep. (National Institute of Standards and Technology, Standard Reference Data Program, Gaithersburg, MD, 2010).

[19] A. C. Aldo and B. M. Argrow, *Supersonic Minimum Length Nozzle Design for Dense Gases,* Tech. Rep. (NASA, 1993).

[20] K. L. McLallin and J. E. Haas, *Experimental performance and analysis of a 15.04-centimeter-tip-diameter radial-inflow turbine with work factor of 1.126 and thick blading,* Tech. Rep. (NASA, 1980).

[21] J. D. Andeson, *Moder Compressible Flow with Historical Perspective*, 3rd ed., edited by J. D. Andeson (McGraw-Hill, 2004).

[22] M. Gad-el Hak, *Basic instruments,* (CRC Press, 2016) Chap. 45, pp. 1–14.

[23] S. S. Kutateladze, A. A. Borisov, A. A. Borisov, and V. E. Nakoryakov, *Experimental detection of a rarefaction shock wave near a liquid-vapor critical point,* Akademiia Nauk SSSR Doklady **252**, 595 (1980).

[24] N. R. Nannan, *Advancements in Nonclassical Gas Dynamics*, Ph.D. thesis, Delft University of Techology (2009).

[25] T. Mathijssen, *Experimental Observation of Non-Ideal Compressible Fluid Dyamics*, Ph.D. thesis, Delft University of Technology (2016).

[26] F. J. D. Galiana, A. P. S. Wheeler, and J. Ong, *A study of trailing-edge losses in organic rankine cycle turbines,* in *Proceedings of ASME Turbo Expo 2015* (Montreal, Canada, 2015).

[27] M. Preissinger and D. Brueggemann, *Thermal stability of hexamethyldisiloxane (mm) for high-temperature organic rankine cycle (orc),* Energies **9** (2016).

[28] G. E. Elsinga, *Density measurements by mmean of schlieren methods*, Master's thesis, Delft University of Technology (2003).

[29] A. Spinelli, *Design and construction of a Test Rig for Organic Vapours*, Ph.D. thesis, Politecnico Di Milano (2010).

[30] G. Gori, M. Zocca, G. Cammi, A. Spinelli, and A. Guardone, *Experimental assessment of the open-source su2 cfd suite for orc applications,* in *International Seminar on ORC Power Systems* (Milano, Italy, 2017).

[31] A. Head, C. Servi, E. Casati, and P. Colonna, *Prelimnary design of the orchid: A facility for studying non-ideal compressiblr fluid dyamics and testing orc expanders,* in *ASME Turbo Expo 2016* (2016).

[32] W. Ueno, S. nd Tsuru, Y. Kinoue, N. Shiomo, and T. Setoguchi, *Piv mesurement of carbon dioxide gas-liquid two-phase nozzle flow,* in *ASME-JSME-KSME Joints Fluids Engineering Conference* (2015).

[33] S. Chapman and T. G. Cowling, *The Machathematical theory of non-uniform gases*, edited by D. Burnett (Cambridge University Press, 1970).

[34] T. H. Chung, L. L. Lee, and K. E. Starling, *Applications of kinetic gas theories and multiparameter correlation for prediction of dilute gas viscosity and thermal conductivity,* Ind. Eng. Chem. Fundam. **23** (1984).

[35] M. L. Huber, A. Laesecke, and R. A. Perkins, *Model for the viscosity and thermal conductivity of refrigerants, including a new correlation for the viscosity of r134a,* Industrial & Engineering Chemistry Research (2003).

[36] M. Born and E. Wolf, *Principles of Optics* (Cambridge University Press, 1999).

[37] J. C. Owens, *Optical refractive index of air: Dependence on pressure, temperature and composition,* Applied Optics (1967).

[38] W. Merzkirch, *Flow Visualization* (Academic Press Inc. (London) Ltd., 1987).

[39] W. Swientoslawski, *Atomic refraction,* Journal of the American Chemical Society (1920).

[40] E. L. Warrick, *The application of bond refractions to organo-silicon chemistry,* Journal of the American Chemical Society (1946).

[41] M. J. Hunter, J. F. Hyde, E. L. Warrick, and H. J. Fletcher, *Organo-silicon polymers. the cyclic dimethyl siloxanes*,* Journal of the American Chemical Society (1946).

[42] A. H. Fainberg and W. Miller, *Molar refractivity in flourine-containing perhalo compounds,* Journal of the American Chemical Society (1965).

[43] Y. Liu and P. H. Daum, *Relationship of refractive index to mass density and self-consistency of mixing rules for multicomponent mixtures like ambient aaerosol.* Journal of Aerosol Science **39**, 974 (2008).

[44] M. R. Maxey and J. J. Riley, *Equation of motion for a small rigid sphere in a nonuniform flow,* Physics of Fluids **26**, 883 (1982).

[45] N. Lang, *Investigation of the flow tracking capabilities of tracer particles for the application of piv to supersonic flow fields,* in *Aerodynamisches Institut Rheinisch-Westfalische Technische Hochschule (RWTH) Aachen* (1999).

[46] M. J. Walsh, *Influence of Partilce Drag Coefficient on Particle Motion in High-Speed Flow with Typical Laser Velocimeter Application*, Tech. Rep. (NASA Langley Research Center, Hampton, Va., 1976).

[47] F. Scarano and B. W. van Oudheusden, *Planar velocity measurements of a two-dimensional compressible wake,* Experiments in Fluids **34**, 430 (2003).

[48] P. J. Pritchard, *Fox and McDonald's Introduction to Fluid Mechanics*, edited by J. C. Leylegian (JOHN WILEY & SONS, INC., 2011).

[49] M. Glass and I. M. Kennedy, *An improved seeding method for high temperature laser doppler velocimetry,* Combustion and Flame **29**, 333 (1977).

[50] M. A. Mendez, M. Raiola, A. Masullo, S. Discetti, A. Laniro, R. Theunissen, and J. M. Buchlin, *Pod-based background removal for particle image velocimetry,* Experimental Thermal and Fluid Science (2016).

[51] E. F. J. Overmars, N. G. W. Warncke, C. Poelma, and J. Westerweel, *Bias errors in piv: the peak locking effect revisited,* in *International Symposium on Application of Laser Techniques to Fluid echanics* (2010).

[52] W. G. Cochran, *The flow due to a rotating disc,* Zeitschrift fuer angewandte Mathematics u. Mechanik **30** (1934).

[53] J. Westerweel, *Efficient detection of spurious vectors in particle image velocimetry data,* Experiments in Fluids **16**, 236 (1994).

[54] J. Westerweel and F. Scarano, *Universal outlier detection for piv data,* Experiments in Fluids (2005).

[55] S. Bahamonde, M. Pini, C. De Servi, A. Rubino, and P. Colonna, *Method for the prelimnary fluid dynamic design of high-temperature mini-organic rankine cycle turbines.* Journal of Engineering for Gas Turbine and Power (2017).

[56] E. Casati, S. Vitale, M. Pini, G. Persico, and P. Colonna, *Centrifugal turbines for mini-organic rankine cycle power systems,* Journal of Engineering for Gas Turbine and Power **136** (2014).

[57] G. E. Elsinga, B. W. van Oudheusden, and F. Scarano, *Evaluation of aero-optical distortion eeffect in piv,* Experiments in FLuids (2005).

[58] D. Ragni, F. Schrijer, B. W. van Oudheusden, and F. Scarano, *Particle tracer response across shocks measured by piv,* Experiments in Fluids **50**, 53 (2011).

[59] L. D. Landau and E. M. Lifshitz, *Fluid Mechanics*, edited by E. M. Lifshitz (Pergamon Press, 2013).

[60] C. Eckart and G. Young, *The approximation of one matrix by another of lower rank,* Psychometrika (1936).

[61] B. Wieneke, *Generic a-posteriori uncertainty quantifcation for piv vector fields by correlation statistics,* in *International Symposium on Application of Laser Techniques to Fluid Mechanics* (2014).

[62] A. Sciacchitano, D. Neal, B. Smith, S. Warner, P. Vlachos, B. Weineke, and F. Scarano, *Collaborative framework for piv uncertainty quantification: comparative assessment of methods,* in *International Symposium on Application of Laser Techniques to Fluid Mechanics* (2014).

[63] B. Grossman, *Fundamental concepts of real gas dynamics,* (Department of Aerospace and Ocean Engineering Virginia Polytechnic Institute and State University, 2000).